An Acoustical Study of the Properties and Behaviour of Sea Ice

by

Yunbo Xie

B. Sc. , Shangdong College of Oceanography, Qingdao, China, 1982

M. Sc. , Shanghai Acoustics Laboratory, The Chinese Academy of Sciences, 1985

A THESIS SUBMITTED IN PARTIAL FULFILLMENT OF

THE REQUIREMENTS FOR THE DEGREE OF

DOCTOR OF PHILOSOPHY

in

THE FACULTY OF GRADUATE STUDIES

(Department of Oceanography)

We accept this thesis as conforming to the required standard

THE UNIVERSITY OF BRITISH COLUMBIA

April 1991

In presenting this thesis in partial fulfilment of the requirements for an advanced degree at the University of British Columbia, I agree that the Library shall make it freely available for reference and study. I further agree that permission for extensive copying of this thesis for scholarly purposes may be granted by the head of my department or by his or her representatives? It is understood that copying or publication of this thesis for financial gain shall not be allowed without my written permission.

Department of ___Oceanography___

The University of British Columbia
Vancouver, Canada

Date ___April 25, 1991___

Abstract

The primary goal of this thesis is to utilize acoustical radiation from the Arctic ice cover to infer the response of sea ice to environmental forcing, and to sense remotely the mechanical properties of the ice. The work makes use of two experiments in the Canadian arctic undertaken by the Ocean Acoustics Group of the Institute of Ocean Sciences, which resulted in an extensive body of acoustical and related environmental data. Cracking sounds originating from both first and multi-year ice fracturing processes are analyzed. Data used in this thesis also include sound made by artificial sources.

The survey of *in situ* ice conditions by air photography and synthetic radar imaging, and a crack distribution map based on observations made with a 3-D hydrophone array, reveal, for the first time, a close correlation between thermal cracking events and ice type. It is shown that most of the thermal cracks occur in irregular multi-year ice where there are exposed, snow-free surfaces.

The study shows that acoustical radiation from some cracks implies a slip-stick seismic movement over the faults, and some cracks tend to radiate more high frequency sound downwards rather than sideways. This phenomenon is most clearly apparent in sounds made by artificial sources. Another interesting finding from this study is that the sound of cracking ice does not always exhibit a vertical dipole radiation pattern, and some cracks due to thermal tension on smooth first year ice radiate more energy horizontally.

The observations have motivated the development of various analytical models. These models allow the observed acoustical features to be related to the length and

depth of a crack, the thickness of the ice cover and its Young's modulus. The models also show that maximum sound radiation from a crack is in the direction of external forcing.

Finally, it is found that noise due to rubbing between ice floes exhibits a narrow band spectrum. This phenomenon is investigated and a linear model derived shows that the observed peak frequency is that of the first mode horizontal shear wave triggered by frictional effects at the ice floe edge.

Contents

List of Tables

List of Figures

Acknowledgements

First of all, I would like to thank Dr. David M. Farmer for providing me with such a wonderful opportunity of doing my graduate studies in Canada, a marvellous country with marvellous people. During my four years thesis research under his supervision, David has always been very supportive to me. Not only did he constantly give me many enlightening suggestions on both data processing and analysis, he also provided me with financial support throughout most of my graduate studies which is highly appreciated.

I would also like to thank Dr. Steve Pond for his guidance and also his assistance on many practical matters.

I am indebted to Grace Kamitakahara-King for her generous help in computer programming. Thanks to Grace, I can now work with my computer instead of swearing at it all the time. I am also indebted to Ron Teichrob for designing and building the electronic equipment used in my experiment, without which this work could not have been done. Dr. Sherman Waddell carried out the 1987 experiment and provided some very insightful suggestions to me at the early stage of this work.

A number of people at the Institute of Ocean Sciences were of great help to me. Among them are Robert Lake, Danny Richards, Ron Perkin, Humfrey Melling, Allan Douglas, Sharon Thomson and Netta Delacretaz.

I can never forget enormous help I received in both my life and work from my best friends and fellow students Len Zedel and Svein Vagle. It is hard to find appropriate words to express my deep indebtedness to them. Let me say that I promise I will never ask them to test drive a car that does not have brakes again.

Special thanks are due to my fellow students and friends Daniela DiIorio, Dimitri Menemenlis and Li Ding for constantly reminding me that apart from work there are many enjoyable things in life, such as playing music, kicking a soccer ball, cooking a Chinese dinner for my country folks, etc.

Finally, I thank my family for their great emotional support for my overseas studies in the past four and half years. This support is invaluable to me and I owe my family for that for the rest of my life.

I HEREBY DEDICATE THIS THESIS TO THOSE WHO SACRIFICED THEIR VALUABLE LIVES FOR THE DEMOCRATIC FUTURE OF CHINA.

唐玄奘西行圖

西行歷盡坎坷難
跋涉萬里往伽竺
彌勒橫流中華土
聖僧留芳千古讚

So harsh was
the journey to the West;
Seeking the truth
for his countrymen,
a monk trudged
thousands of miles
on a bumpy road.

a story from
the Tang Dynasty.

Introduction

Arctic oceanography is a unique branch of ocean science. In contrast to the open ocean environment, the existence of sea ice in the Arctic inhibits direct transfer of momentum, heat and gas between the atmosphere and ocean. Arctic oceanography also presents one of the most challenging areas of geophysical research. In man's long history of battling the Arctic, early explorers were not discouraged by the hostile environment. Numerous expeditions (both successful and unsuccessful), have provided us with extensive knowledge of this cold part of the world.

With the discovery of large oil and natural gas fields beneath the continental shelf, the Arctic has become increasingly important. But the exploration and transport of these energy resources require a comprehensive knowledge of sea ice, and in particular its physical properties. The physical behaviour of sea ice is determined by its mechanical properties and the environmental stresses to which it is subject. As a passive system, sea ice absorbs momentum from both the wind and ocean current. Thus, an ice cover is under stress on both of its boundaries. If the stress exceeds the strength of the ice cover, the ice will respond by cracking or even breaking up. As an active system, the motion of an ice cover will exert a stress on the surface water and air. Therefore, sea ice behaviour has a great influence on air-sea interaction in the Arctic Ocean.

This thesis deals with one aspect of sea ice behaviour — *The Response of Sea Ice to Environmental Forcing*, which seems to be one of the topics that interests physical oceanographers, Arctic engineers and the shipping industry. Due to the complication of environmental forcing, an inverse approach is adopted to gain some

1

physical insight of both the applied stress and mechanical properties of sea ice. The information leading to the understanding of the behaviour and properties of sea ice is obtained from the acoustical radiation of stressed sea ice. The thesis consists of five chapters outlined below:

Chapter 1 provides some background knowledge relating to the problems dealt with in this thesis. These include mechanical properties of sea ice, the physical process of ice failure, stress induced by environmental forcing and acoustical properties of sea ice.

Chapter 2 describes the 1987 Beaufort Sea Ambient Sound Experiment. An ice breaking model is derived based on the observations of individual cracking events.

Chapter 3 discusses thermal stress cracking. The discussion includes a description of the 1988 Ambient Sound Experiment in the Central Canadian Arctic, the spatial distribution of thermal cracking events with respect to *in situ* ice conditions, the impulse response of an ice cover, the angular frequency dependent radiation of thermal cracking and remote sensing of Young's modulus and ice thickness.

Chapter 4 deals with ambient sound due to break-up of landfast ice. The analysis is based on the 1987 Beaufort Sea experiment. This chapter includes a scenario of the break-up of landfast ice, pure tone ambient sound due to ice rubbing, and horizontal failure of an ice cover. In the end, a steady solution to a boundary value problem is solved to interpret the pure tone sound generation mechanism.

Chapter 5 summarizes the main results of this research and points out potential research directions for future studies.

Chapter 1

Background

1.1 The Geophysics of Sea Ice and Motivation of the Study

An excellent review of the geophysics of sea ice is given by Untersteiner [1]. He points out that

> Terrestrial temperatures lie in a range, where in the course of a year, the sea surface at high latitudes gets cold enough to freeze. The heat of fusion released by the sea surface to form a layer of ice one-metre thick is an order of magnitude smaller than the mean annual total of either short-wave or long-wave radiation reaching the surface. Therefore, small changes in the climatic forcing will produce large changes in the extent of ice-covered areas, which makes sea ice a very sensitive system to global climatic variations.

Being a mechanical as well as a thermal barrier between the ocean and atmosphere, sea ice suppresses the exchange of kinetic energy and heat between the two media, while the ocean temperature beneath the ice is held at a nearly constant value (freezing point of the sea water).

However, the large extent of sea ice is not forced unilaterally by oceanic and atmospheric conditions. Rather, it participates in a variety of feedback effects both positive and negative. As a positive feedback system, once ice occurs, the nearly black sea surface with *albedo* $\leq$ 0.1 becomes highly reflective to solar radiation, reducing the net short-wave radiation and thus cooling the surface and contributing to an expansion of the ice cover. As a negative feedback system, the cold surface builds a temperature inversion in the atmospheric boundary layer, directing more sensible heat towards the surface. Sea ice, as a bridge between atmosphere and ocean, plays an extremely important role in air-sea interaction at high latitudes.

The study of sea ice is also important to Arctic engineering. With conventional world oil resources being slowly depleted, there is an increasing interest in developing Canada's Arctic oil and gas. As a result, a comprehensive knowledge of the physical characteristics of sea ice is required to allow for safe oil exploration activity.

Ice motion is a serious problem to Arctic shipping . An improved capability for predicting ice behaviour and movement would contribute to safer and more economic navigation in the arctic channels and ocean.

Although the advance of science and technology has increased man's knowledge of the Arctic, our understanding of sea ice properties is very limited, partly due to the fact that the Arctic environment is harsh making it very difficult and costly to engage in field studies there. So far, most of the studies on mechanical properties of sea ice have been based on ice samples of both limited number and size. Scientists have learned some characteristics of sea ice by detailed experimental tests using small samples. However, cutting the natural ice into small pieces eliminates its large scale rheological nature which is one of its important features. Moreover, the boundary conditions will also be changed.

Sound generation and propagation in sea ice is a problem of longstanding interest. As we know, sea ice is far from being a material with uniform and consistent behaviour. Moreover, the ice cover itself is a mixture of new and refrozen leads, first year and multi-year ice, pressure ridges, and sometimes icebergs. In such a

complicated and unpredictable environment, analysis of acoustic signals may provide valuable insight on mechanisms of fracture that would be hard to achieve with more direct techniques. Thus, acoustic remote sensing techniques provide a unique way to study Arctic sea ice. Ambient sound generated by ice activities can travel a great distance through sea water which is an excellent sound channel. Acoustical sensors can also pick up those signals leaking from the ice waveguide into the water. The advantage of this approach is that it allows one to gain good physical insight into sea ice activities without the complications and physical interference of *in situ* measurement. Thus, Arctic acoustics has become one of the most important Arctic sciences with great potential for the study of sea ice behaviour and properties. This potential has already shown its unique effectiveness in remote sensing of sea ice (see Ref. [2], [3] and [4]).

1.2　Mechanical Properties of Sea Ice

Based on work over the last thirty years Mellor [5] gives a very comprehensive description of the mechanical properties of sea ice and his paper has become a handbook for those who want to enter this field. Generally speaking, sea ice is a very complicated material in terms of its mechanical properties; its elastic parameters are functions of temperature, salinity, brine volume, crystal size, orientation of c-axis (optical axis), time, etc. Brine volume is defined by Pounder [6] as the fraction of the volume of a piece of sea ice occupied by fluid, brine or air. Pounder [6] suggested that sea ice, to a first order of approximation, be considered as a visco-elastic material and its mechanical behaviour be described by a rheological model known as a Maxwell unit. Although this is a simple model, it illustrates the distinct mechanical behaviour of sea ice. Therefore, it is worthwhile presenting the basic ideas of the Maxwell unit.

Neglecting the anisotropic nature of sea ice, for any kinds of deformation, one can decompose the stresses applied to the ice into pure tensile stress, illustrated in Figure 1.1(a) by an ice cylinder, pure shear stress (Figure 1.1(b)) by an ice block and pure compression or dilatation as shown in Figure 1.1(c) by a piece of ice immersed in a fluid. The relationships between strain, e_{ij}, and stress, s_{ij}, for the three cases are given as follows:

$$s_{xx} = E e_{xx}, \tag{1.1}$$

$$s_{xy} = \mu e_{xy}, \tag{1.2}$$

$$p = k \frac{\Delta v}{v} \tag{1.3}$$

and

$$\sigma = -\frac{e_{yy}}{e_{xx}}, \tag{1.4}$$
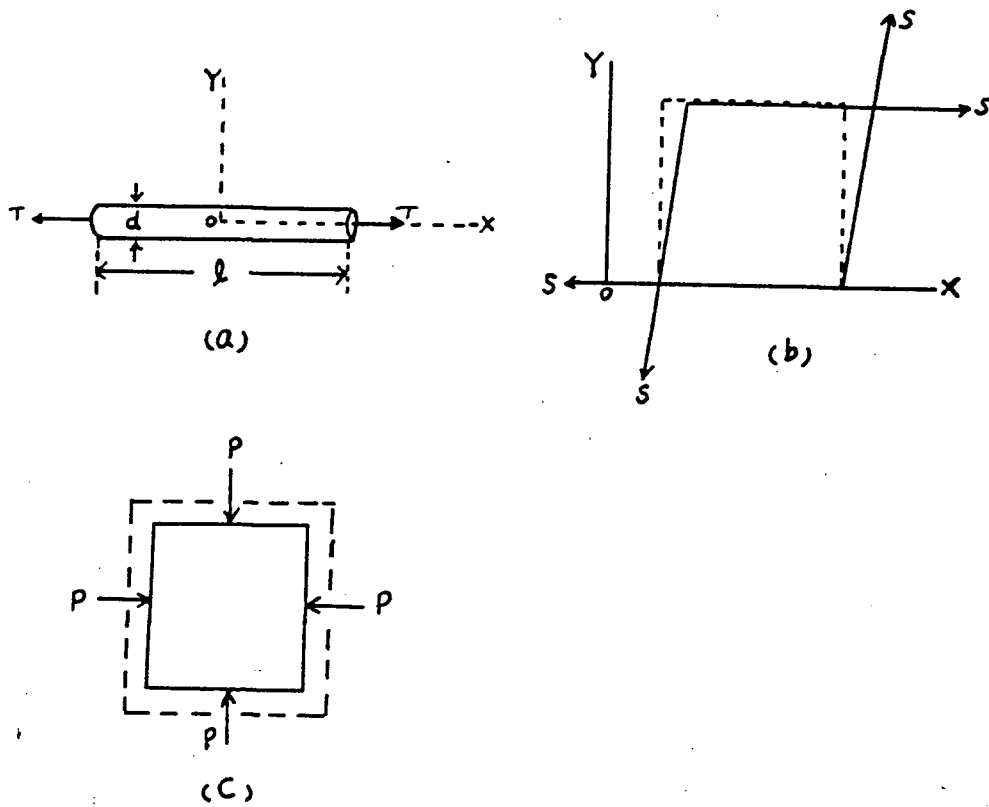
Figure 1.1: Sketch illustrating 3 types of Stresses (after Pounder).(a). Pure tensile stress on an ice cylinder. (b) Pure shear stress on an ice block; the dotted rectangle indicates an unstrained block of ice. (c) Compressional pressure on an ice block.

where E is Young's modulus of ice; μ is the shear modulus or rigidity of ice; k is the bulk modulus of ice and $\Delta v/v$ is the fractional decrease in volume; p is hydrostatic pressure; σ is Poisson's ratio.

Let e_e, e_v, e_t be the elastic, viscous and total strains respectively. Assume a sinusoidally varying shear stress $s = s_0 \sin \omega t$ is applied to a block of so-called visco-elastic ice. For the elastic part of the strain, by Hooke's law ,

$$\mu e_e = s. \tag{1.5}$$

For the viscous part of strain, using the Newtonian flow model

$$\eta \frac{de_v}{dt} = s, \tag{1.6}$$

where η is the coefficient of viscosity of the ice. Since $e_t = e_e + e_v$,

$$\frac{de_t}{dt} = \frac{de_e}{dt} + \frac{de_v}{dt}. \tag{1.7}$$

Substituting equations (1.5) and (1.6) into (1.7), one has:

$$\frac{de_t}{dt} = \frac{1}{\mu}\frac{ds}{dt} + \frac{1}{\eta}s. \tag{1.8}$$

This is the mathematical expression for the Maxwell unit shown in Figure 1.2.
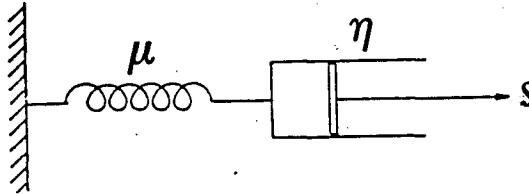
Figure 1.2: A rheological model for sea ice: the Maxwell unit.

In Figure 1.2, a dash pot and a spring have been connected in series to simulate the visco-elastic property of sea ice indicated by equation (1.8); that is, the total strain in the ice is the sum of strains due to elastic and viscous deformations. A more thorough discussion of ice properties based on the Maxwell unit can be found in Pounder's book (pp. 93 to 95 of Ref. [6]).

Driven by the harmonic stress $s = s_0 \sin \omega t$, equation (1.8) leads to a response

$$e_t = \frac{s_0}{\mu} \sin \omega t + \frac{s_0}{\omega \eta} (1 - \cos \omega t). \qquad (1.9)$$

From (1.9), it is seen that if $\omega \gg \mu/\eta$, the first term is dominant and the strain is almost entirely elastic. Taking $\mu = 2.5 \times 10^9 Pa$ (a reasonable value for pure ice), and $\eta = 1.0 \times 10^9 Pa \cdot sec/cm^2$ (a reasonable figure for temperature $\approx -5^0 C$ and stress $\approx 9.8 \times 10^4 Pa$), one has $\omega \gg 2.5 rad/sec$. That is to say, any periodic forces with a period much less than 1 second will only result in elastic deformations of ice. The viscosity of ice affects its elastic behaviour if the ice is subject to a slowly varying force.

In general, the strain-stress curve of ice has three different ranges. They are:

1. The elastic region where Hooke's law holds;

2. The plastic region where the relationship between strain and stress is nonlinear and after the stress is removed ice cannot revert to its original shape;

3. The yield point, or the ultimate stress point, at which ice breaks.

However, the distribution of these three ranges varies greatly with the rate of stress application, or strain rate. If the stress is applied rapidly to ice, and for a short period of time only, the elastic range of the ice will be quite large and the plastic range very small, that is, stress only slightly above the elastic limit will lead to fracture. These characteristics were illustrated by Karlsson [7] in his numerical model. Figure 1.3 shows the results.

It should be pointed out that the Maxwell unit is the simplest model for ice. Apart from elastic and viscous behaviour, ice has plastic and creeping properties. With creeping, ice can actually memorize stresses. In other words, it can delay its deformative response to a stress being applied to it for a long time. All these characteristics can be modelled in a way similar to the derivation of the Maxwell unit. More comprehensive models are summarized in Mellor's paper [5].

Sea ice grows out of sea water and forms a layered structure, from which sea ice inherits a so-called profile property, i. e. the mechanical properties of the ice cover vary with depth. Cox and Weeks [8] in their recent paper reviewed a wide variety of field studies conducted in different polar regions. They summarized data sets collected by a number of people and derived vertical distributions of temperature and salinity for ice sheets of different thickness. Using a least squares fitting method, Cox and Weeks [8] obtained empirical formulae for Young's modulus, and Poisson's ratio in terms of brine volume profiles in ice sheets. Figure 1.4 shows profiles of Young's modulus for ice sheets of 10 different thicknesses. Generally, the Young's modulus in the surface layer of an ice sheet is greater than that in the lower layer.
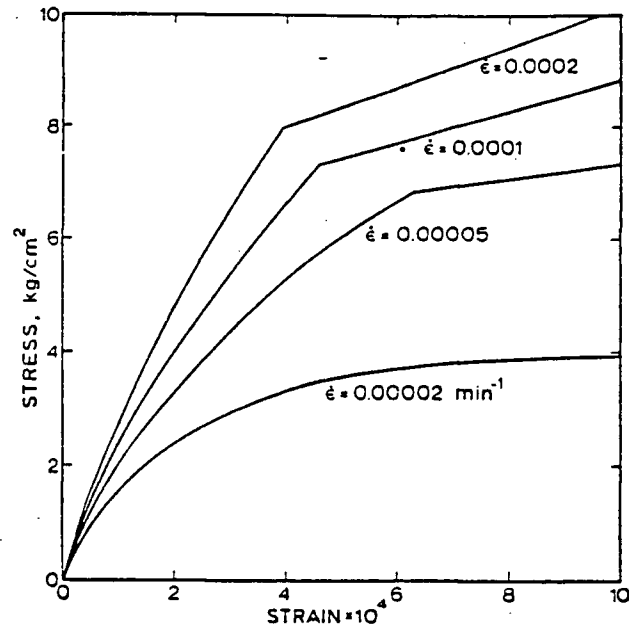
Figure 1.3: Uniaxial stress-strain curves for viscoelastic-plastic model at various strain rates indicated by $\dot{\epsilon}$.
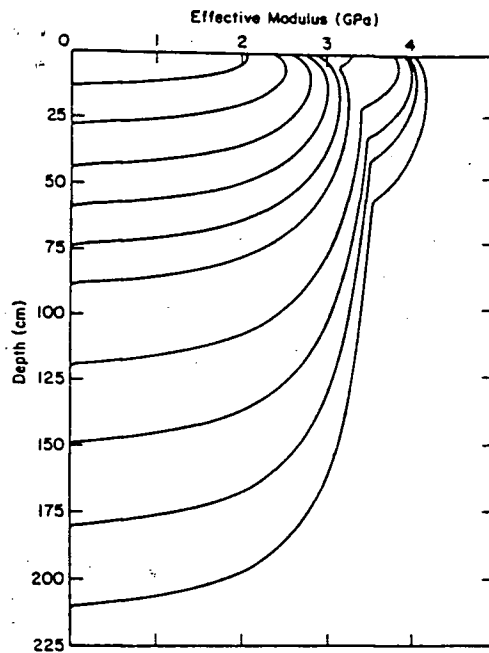
Figure 1.4: Young's modulus profiles for 10 different ice thicknesses (after Cox and Weeks). Each profile intersects the vertical axis at the depth corresponding to the bottom of the ice and thus shows the model profile for ice of that thickness.

1.3 Physical Process of Ice Failure

In studying the strength of an elastic plate, Griffith [9] first postulated a criterion for growth of a crack of length $2c$. The basic idea is: *the change of potential energy in the plate is equal to the change of surface energy in the crack as it grows in length.* Mathematically this idea can be expressed as

$$\frac{\partial}{\partial c}(\frac{\pi s^2 c^2}{E}) = \frac{\partial}{\partial c}(4c\gamma),$$ (1.10)

where γ is the specific surface energy of the material; s is the applied stress (tensile stress perpendicular to the long axis of the crack) at which crack growth occurs. Therefore, the minimum applied stress necessary for crack growth is

$$s = (\frac{2E\gamma}{\pi c})^{\frac{1}{2}}.$$ (1.11)

However, the predicted values from (1.11) were found to be too low for the actual strength of most material, including ice samples. This discrepancy is explained by the fact that once a crack occurs, a large amount of stress will concentrate at the crack's tip, which has the effect of blunting the crack. Hence, further growth of the crack requires an extra amount of work to overcome this barrier or "plastic region".

Orowan [10] modified Griffith's model by including a specific energy for plastic working γ_p in (1.11). Since $\gamma_p \gg \gamma$, (1.11) becomes

$$s \approx (\frac{2E\gamma_p}{\pi c})^{\frac{1}{2}}.$$ (1.12)

This result is important, because it emphasises the fact that less energy is required to lengthen a crack than is required to start one. It is seen that as the crack lengthens (c increases), the stress required for further extension of the crack decreases.

While the above model gives a nice picture of failure processes in an elastic plate, it is hard to use this theory to get a quantitative interpretation of sea ice cracking. Sea ice has a more complicated structure than an elastic plate and, as mentioned above, its elastic parameters vary with temperature, salinity and other

factors. Therefore, the discussion of ice properties in terms of these parameters is of limited value. It is almost impossible to get an analytical form relating elastic parameters with these factors. Based on a laboratory study, Dykin [11] concluded that

1. Neither the grain size nor the spacing of platelets (smallest elements of ice crystals) have much influence on the tensile strength.

2. Orientation of the grain structure in relation to the stress field has a significant influence. That is, the vertical tensile strength is 2 to 3 times greater than the horizontal one.

3. Temperature has a linear effect on ice strength while salinity has a nonlinear effect. The influence of temperature and salinity could be converted into a single function — brine volume.

Based on field data obtained from sites scattered throughout the Arctic, Cox and Weeks [8] derived empirical formulae for the tensile (TS), shear (SS) and flexural strength (FS) of sea ice in terms of its brine volume BV. These are:
For horizontal tensile stress tests:

$$TS = 0.816 - 0.0689\sqrt{BV}; \tag{1.13}$$

For vertical tensile stress tests:

$$TS = 1.54 - 0.0872\sqrt{BV}; \tag{1.14}$$

For shear stress tests:

$$SS = 1.68 - 0.118\sqrt{BV}; \tag{1.15}$$

For flexure stress tests:

$$FS = 0.959 - 0.0608\sqrt{BV}; \tag{1.16}$$

where strength is in *Mega Pascals* (*MPa*); BV is in parts per thousand (*ppt*).

It is a matter of common observation that sea ice strength increases as temperature drops. Assur [12] attributed this phenomenon to the reinforcement of the mechanical strength of the ice by the solid salt deposited in it.

Assur [12] also gave a theoretical model for sea ice structure and related it to the strength of sea ice. The basic idea is very simple. He assumed that the reduction in the strength of sea ice was proportional to the reduction in ice volume due to the existence of rows of brine cylinders in the ice. The strength for ice with this structure is

$$s = s_o(1 - 2\sqrt{\frac{\gamma}{\pi\beta_0}}\sqrt{\mu}), \tag{1.17}$$

where s and s_0 are the ultimate tensile strengths with and without brine respectively; $\gamma = g/g_0$ with g and g_0 being the average length and average separation of brine pockets along the growth axis respectively; μ is the brine volume; $\beta_0 = b_0/a_0$ where a_0 is the average platelet thickness, and b_0 the average brine cylinder separation.

As revealed by (1.17), the strength of sea ice decreases as the brine content increases, which is mainly due to increasing temperature. Another interesting result of (1.17) is that there is a limiting value of μ at which s vanishes. This no-strength condition occurs for $\mu_c = \pi\beta_0/4\gamma$, and gives the critical value of μ at which the skeleton layer of sea ice is growing.

1.4   Stresses Induced by Environmental Forcing

The fact that an ice cover is exposed to air and sea water implies that it is subject to direct environmental forcing. This forcing determines, to a large extent, the behaviour of sea ice. The consequence of air-ice-ocean interaction is to induce various kinds of stresses acting on an ice cover forcing it to behave in accordance with environmental variations. I will examine in the following how stresses are induced by environmental forcing of various origins.

Thermal Tension Stress

Lying, as it does, along the interface between air and ocean, the upper and lower surfaces of an ice cover are under quite different influences due to different temperature variations in the air and ocean. Having a large heat content, the temperature variation in sea water is much less than that in air. As a result, the temperature of the lower surface of the ice cover tends to remain constant and close to the freezing point of sea water, while the upper surface is forced to match the greater temperature variation in the air. Because of the low thermal conductivity of ice , the ice cover is generally in a state of thermal imbalance, which induces thermal stress (either tensile or compressional) at the ice surface. If such a stress exceeds the strength of the ice cover, thermal fissures will appear at the ice skin, which will generate sound by thermal cracking. It is well known that, when cooled, the upper layer of an ice cover will be under tensile stress and contract. In the release of tensile stress, fissures will appear on the upper surface (Zubov [13]). Lewis [14] has hypothesised that when warmed the surface layer of the ice will be under compressional stress and expand. Since the lower layer resists any thermally related changes, the expansion of the upper layer will cause a build-up of tensile stress in the lower layer. Thus, fissures will appear on the lower surface. The forces inducing these two kinds of fissures are illustrated in Figure 1.5. However, field studies have shown that thermal cracking occurs mainly at night when the air temperature is dropping. On the other hand,
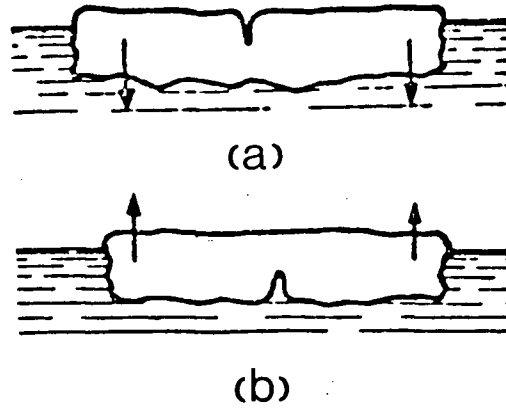
Figure 1.5: Cracks due to thermal stress (after Zubov).(a) Cooling induced tensile stress causing upper surface cracking. (b) Heating induced compressional stress causing lower surface cracking.

thermal expansion appears to produce much less sound than thermal contraction, which is probably due to the fact that thermal expansion causes compression in ice while thermal contraction introduces tension, and according to Pounder [6], for fresh water ice, its compressional strength is 2 to 3 orders greater in magnitude than its tensile strength.

Milne [15] carried out experimental studies of thermal cracking and found that the horizontal stress S_h induced by a temperature change ΔT is given as

$$S_h = \alpha_v \Delta T E/3, \qquad (1.18)$$

where E is Young's modulus of the ice and α_v is a thermal volumetric expansion coefficient which is strongly dependent on salinity and temperature. In the case of high salinity, α_v is negative over a wide range of temperature. For low salinity values,

α_v is generally positive, i. e. as temperature decreases , α_v will increase towards the value for pure ice. He also found that for thermal tension cracking to occur, the air temperature must be low enough, say, $\leq -20^0 C$ and the ice must have very low salinity ($\leq 5ppt$) so its behaviour approximates that of a brittle material. Therefore, thermal tension cracking tends to occur in old (multi-year) ice.

However, the above theory has been challenged by Cox [16] and Lewis [14]. Cox has shown, based on his observations, that α_v is almost independent of salinity. As a result, the value of α_v for sea ice is very close to fresh water ice. Lewis notices that the thermal cracking response of sea ice to cooling occurs only after the cooling has continued for one or two hours. He attributes this phenomenon to the plastic characteristics of sea ice. The first effect of cooling is to release the compressional strain built up from daytime heating; cooling will not cause thermal cracking until the compressional strain in the ice is released. On the other hand, snow is an insulator for thermal radiation. Thus, the complete snow covering typical of first-year ice areas, in contrast to multi-year ice, is the main reason why thermal cracking preferentially occurs in multi-year ice areas.

Another feature of ambient sound induced by thermal tension is that the noise level follows a strong diurnal pattern; the noise level increases during cooling at night and decreases substantially during the daytime. According to Farmer and Waddell [17], [18] it is observed that for thermal tension cracking to occur, a clear sky is required at night to allow for long-wave back-radiation; they also noticed that thermal cracking spectra have a peak at about $1000Hz$.

Wind Induced Stress

This stress is caused by wind drag, which is a frictional force between the moving air and rough surface of the ice. Wind induced stress is an important driving force keeping the ice in motion. It can be related to wind speed as (denoted by τ_a)

$$\tau_a = c_{10}\rho_a|\vec{v}_{10}|^2, \tag{1.19}$$

where $\vec{v}_{10}$ is the wind vector at 10 metres relative to the ice drift vector $\vec{v}_d$; c_{10} is the corresponding drag coefficient, which is in the order of 3×10^{-3}; ρ_a is air density.

Current Induced Stress

This stress is caused by water drag, i. e. frictional force between the lower surface of ice and water. If there is no water motion , then there is a retarding force slowing down the motion of the ice. The stress τ_w is expressed as

$$\tau_w = c_w \rho_w |\vec{v}_g|^2, \qquad (1.20)$$

where $\vec{v}_g$ is the current vector of the surface water relative to $\vec{v}_d$; c_w is the drag coefficient, which is typically $2c_{10}$ in magnitude; ρ_w is water density.

It should be noted that wind and current are frequently not independent forces, since the wind tends to drive the surface water, interacting with it in ice-free areas as well as by a coupling through moving ice floes.

Makris and Dyer [19] have studied the correlations between noise level and the two stresses mentioned above. Figure 1.6 shows their results. It is seen that these stresses are highly correlated with ice noise; thus, wind and current induced stresses are the major forcing factors contributing to noise.

Lateral Forces Resulting from Pressure of the Surrounding Ice Floes

The inhomogeneity of ice structure in an ice cover or the physical contact between different floes will induce inhomogenous stress distribution on the ice cover, which may create pressure ridges, buckling, and fragmentation in the ice and crushing and rubbing between adjacent ice floes. Using an energy dissipation concept, Pritchard [20] simulated source levels generated by ridging. His model was able to account for 64% of the acoustical energy associated with a ridge-building event. Buckingham and Chen [21] used a floe-floe collision model to evaluate the ambient noise level
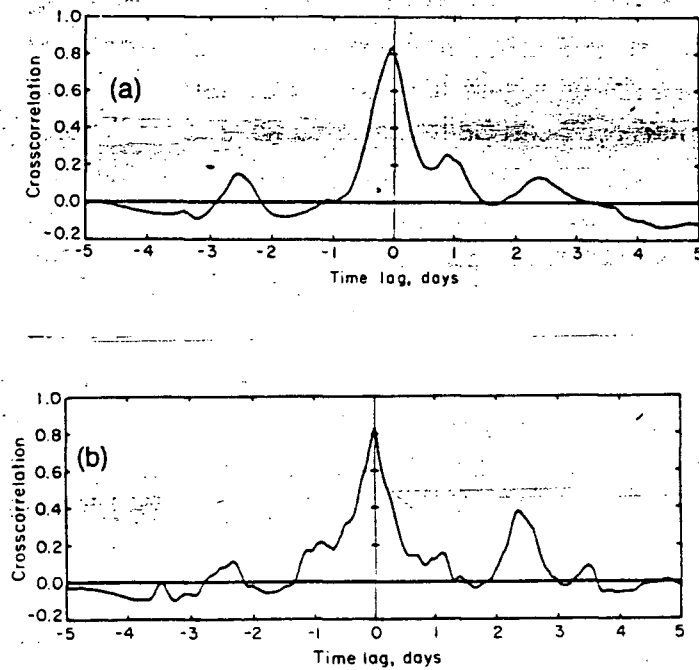
Figure 1.6: Time-lagged normalized cross correlation between noise and (a) wind stress $|\tau_a|$, (b) current stress $|\tau_w|$ (after Makris and Dyer).

below the marginal ice zone (*MIZ*). As far as ice rubbing sound is concerned, there have been no systematic studies published. Motivated by my own data analysis, I will investigate the generation mechanism of this unique sound in the Arctic in chapter 4.

1.5   Acoustical Properties of an Ice Cover

When ice cracks, the sudden displacement at the fracture zone excites various elastic waves. Some of the energy is trapped in the ice cover and may subsequently radiate into the water due to various mechanisms. The acoustic waves emanating directly from the source, and those leaking from the ice plate, contribute to the ambient sound level in the ocean.

In order to understand how sounds generated by ice cracking enter the water, it is first necessary to study wave propagation properties of an ice plate.

Wave propagation in an elastic plate is a classical problem in wave motion theory. Based on Lamb and Rayleigh's early work, Press and Ewing [22] derived an analytical solution to the problem of elastic wave propagation in a floating ice sheet. Consequently, a theoretical characteristic equation for vertically polarized shear (SV) waves and compressional waves was obtained. Based on this expression, they discussed the long-wave (wavelength $\lambda \gg$ ice thickness $2D$) and the short-wave ($\lambda \ll 2D$) cases, giving corresponding phase speeds C for waves travelling freely in horizontal directions. Assuming a value of Poisson's ratio $\sigma = 0.25$ which leads to analytical forms of expressions for C, the five types of waves are summarized as follows:

For short waves, there are three kinds of surface waves at the upper and lower surfaces of the ice cover. These are:

1. Rayleigh wave at the air-ice interface with $C = C_R = 0.9194\beta_1$ where β_1 is the shear wave speed in ice;

2. Attenuated Rayleigh wave at the ice-water interface with $C = C_R(1 + i\frac{1}{4})$ where $i = \sqrt{-1}$;

3. Stonely wave at the ice-water interface with $C = 0.87C_2$ and C_2 is the sound speed in water.

For long waves, there exist two types of waves in the ice. They are:

1. Longitudinal wave or P wave. The dispersion relation is:

$$C = 2\beta_1(1 - \beta_1^2/\alpha_1^2)^{\frac{1}{2}}(1 + ib),$$

where $b \sim O(\frac{D}{\lambda})^3$ and α_1 is the compressional wave speed in ice;

2. Flexural wave with a dispersion relation given by:

$$C^2/\beta_1^2 = (8/3)(\rho_1/\rho_2)(kD)^3(1 - \beta_1^2/\alpha_1^2)(1 + 2kD\rho_1/\rho_2).$$

Here, ρ_1 and ρ_2 are ice and water densities respectively, and k is the horizontal wavenumber.

As for the intermediate wave-lengths, there will be an unbounded number of normal modes corresponding to the roots of the characteristic equation. In this case, it is impossible to obtain an analytical form of the dispersion relation for the characteristic equation. Stein [23] has carried out a detailed numerical investigation of this equation and gained some interesting dispersion curves for P and flexural waves for $\sigma = 0.33$ (a typical value for sea ice). However, it is hard to get a clear physical picture of wave motion in the ice plate from his numerical results.

In accordance with shear deformation in the horizontal direction, there will be horizontally polarized shear (SH) waves. SH waves are also called Love waves, and both surfaces of the ice plate remain pressure free (with respect to this type of wave). Therefore, the SH wave propagation problem is equivalent to finding a solution for wave motions in a plate bounded by a vacuum. The corresponding phase speed is: $C = \beta_1/\sqrt{1 - (n\pi/kD)^2}$. The normal mode frequencies are given by $f_n = n\beta_1/2(2D)$ with $n = 1, 2, \dots$. Thus, the existence of water underneath the ice cover does not affect the characteristics of the ice plate as a perfect wave guide for trapping SH waves.

Another well trapped shear wave is the Crary wave which is an SV wave totally reflected from the ice plate boundaries. The phase speed of Crary waves is equal to the compressional wave speed in ice; that is $C = \alpha_1$, and the normal mode

frequencies are given by $f_n = (n+1)/(4D\sqrt{\beta_1^{-2} - \alpha_1^{-2}})$ with $n = 1, 2, \dots$. For Crary waves , it can be shown that the total reflection of SV wave energy at both surfaces of the ice is due to the incidence of SV waves at an angle $= \cos^{-1}(\beta_1/\alpha_1)$ with the horizontal. At this angle, the interference of incident waves with reflected waves results in a zero displacement at the boundaries, thus preventing energy from radiating into the water for this particular mode.

The SH wave and Crary waves are important in the seismic study of elastic parameters of sea ice and its thickness. Although they are well trapped in an ideal ice plate, they may contribute to underwater ambient sound by leaking their energy to the water once they interact with discontinuities at the ice-water interface. Since the frequencies associated with SH and Crary waves are quite unique (discrete bands), along with the direct acoustic waves, they can provide additional information on source positions and mechanisms.

I have discussed waveguide properties of an ice cover. However, ice is a visco-elastic material, which means that waves accommodated in the ice cover will be highly attenuated with increasing horizontal range. Stein [24] used his numerical model to derive an empirical formula of attenuation due to absorption for flexural and P waves. According to him, for a 10 Hz wave, the maximum range is a few kilometres. It is also known that sea ice is full of cracks, especially along its boundaries with air and water. These old cracks will allow wave energy to leak into the water and air. Consequently, waves trapped in this leaky and attenuating waveguide system will not be able to propagate for a great distance; their contribution to underwater sound is very local. If the background noise level is too high even the local effect of these waves would be masked.

The most important waves contributing to ambient noise are those radiating directly from fracturing zones, through the water to the hydrophones; these are the *direct path acoustic waves*. Sea water allows sound waves to travel a great distance without too much loss and distortion. The acoustical environment of the Arctic Ocean is upward refracting. Thus, the sound from distant sources may travel

great distances if it is not too severely scattered by successive interactions with the ice cover. However, sound sources within $2 \sim 3$ *km* of a hydrophone array can be detected before the sound strikes the ice bottom. Such direct path signals, which are the focus of the present study, contain a wealth of information about the mechanisms responsible for ice cracking.

Based on a spectrum analysis of Arctic ambient sounds, Dyer [25] has classified ambient noise as follows:

1. $10^{-2} \sim 10^{-1} Hz$ noise is due to velocity fluctuations of water flowing past the hydrophones;

2. $1 \sim 10 Hz$ noise results from cable strumming induced by the interaction of current and cables suspending the hydrophones;

3. $1 \sim 1000 Hz$ noise with a peak at about $10 \sim 20 Hz$ is caused by ice activities of different types, including snow saltation induced by wind blowing over ice covers, internal fracturing of ice due to internal stresses and bending moments;

4. $150 \sim 5000 Hz$ noise is due to thermal tension cracking of the ice or microfracturing in the ice.

Figure 1.7 shows Dyer's arctic noise spectrum. I have to emphasize that although this is the first statistical overview of underwater sounds in the Arctic ever proposed, the limited band width of the instruments used for data recording and the long term averaging, eliminates virtually all of the fine structure from the received signals. Therefore, the spectrum shown in Figure 1.7 is poorly resolved, especially at higher frequencies, and the underlying physics of sound generation cannot be recovered from this spectrum.
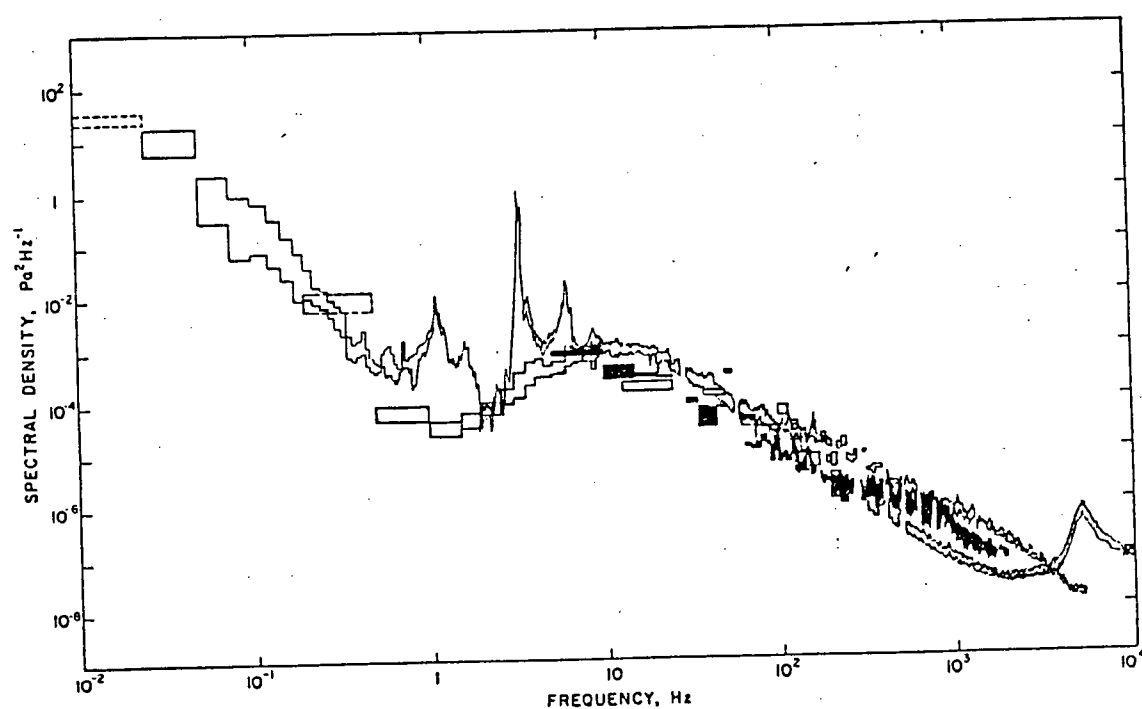
Figure 1.7: General spectral characteristics of central Arctic pack ice noise (after Dyer).

Chapter 2

The Beaufort Sea Ambient Sound Experiment and Ice Breaking Model

2.1 Motivation and Description of the Experiment

A primary source of sound in the Arctic Ocean arises from the response of the ice cover to stress. Thermal tension, and on a larger scale, the effect of wind and current, can build up internal stress within the ice to the point at which it will rupture. The stress generation mechanisms have been discussed in the previous chapter. The visible consequences are cracks, pressure ridges, buckling, and fragmentation. Catastrophic failure of the ice during these events triggers sound waves, and the associated acoustical energy enters the water contributing to the ambient sound levels of the ocean. The problem is interesting from many points of view, but the principal motivation in my work is the expectation that an understanding of the relationship between the observed acoustic signal and physical process of sound generation will lead to the development of remote sensing techniques suitable for the study of ice

behaviour and properties.

The sound field beneath moving pack ice in the Arctic Ocean is the result of a superposition of many such sources (Dyer [25]). While interpretation of this signal remains an important goal of Arctic acoustics, a simpler environment, where individual transient events can be observed in isolation, provides an opportunity for analyzing the detailed structure of the signal without contamination by the background noise. To this end, an experiment was carried out in March 1987 to study the sound of ice cracks beneath landfast ice in Amundsen Gulf in the Beaufort Sea. Figure 2.1 shows the location. A feature of the experiment was that measurements of the sound generated by cracking events were extended up to a frequency of 20 kHz, revealing previously unidentified high-frequency components of the signal. The observations show some similarities to seismic signals, and these similarities have motivated my approach to the analysis in which I adapt a theory of earthquake mechanics to the case of a floating ice sheet. A distinguishing aspect of the theory is that it explicitly incorporates the effects of crack propagation, which appear to account for certain features of the observed signals. The measurements were obtained with a self-recording four-hydrophone array suspended beneath a first-year ice floe as shown in Figure 2.2. Although the ice cover was initially landfast, it broke free during a storm. Fortunately, the floe chosen for our deployment remained intact, and the instruments were successfully recovered 6 days later, approximately 90 km west of the deployment site (Figure 2.1). The ambient sound field was relatively quiet before the storm, with only an occasional loud crack. There was little evidence of a systematic diurnal variation in the sound level associated with thermal tension cracking, as previously observed at the same time of year by Farmer and Waddell [17], [18] in the Amundsen Gulf. Once the ice mobilized, the background sound level rose and there was also a pure tone signal triggered by rubbing between ice floes. I will discuss this kind of sound in Chapter 4.
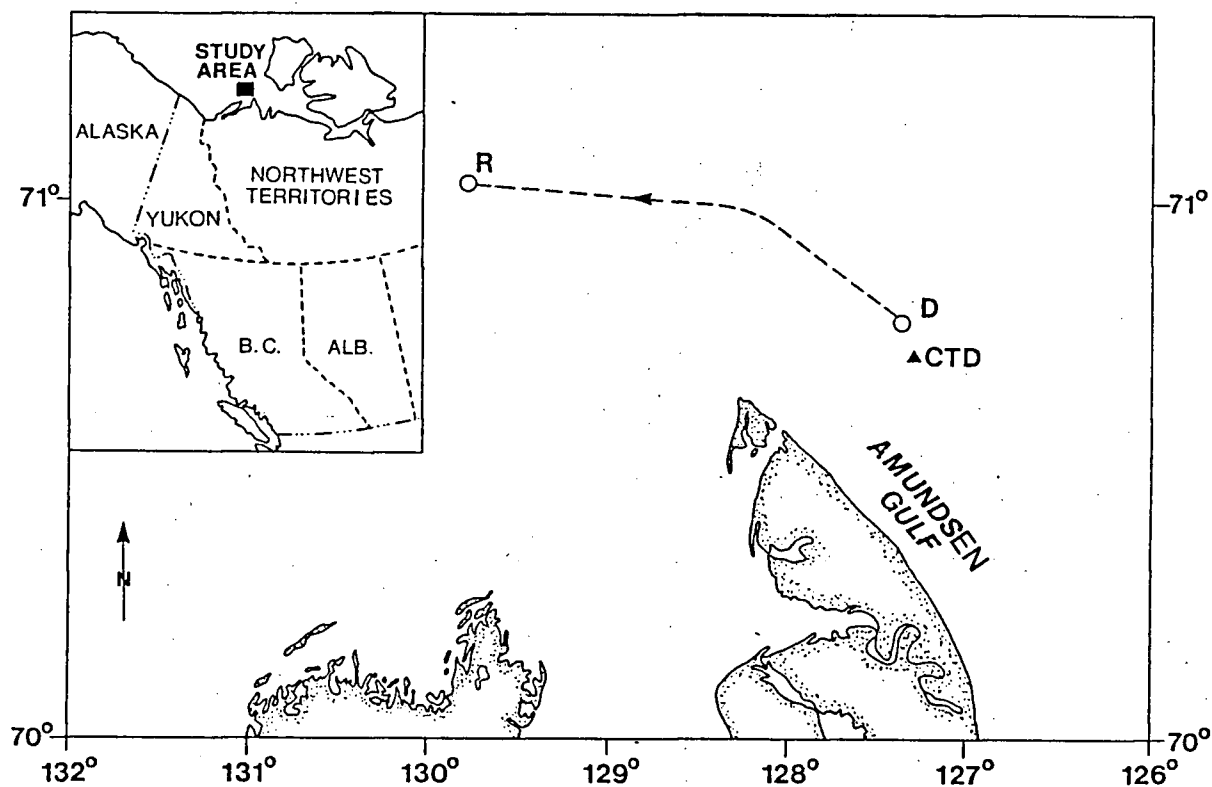
Figure 2.1: Site of the 1987 Ambient Sound Experiment. Also shown are locations of instrument Deployment **D**, and recovery **R**, and the **CTD** profile.
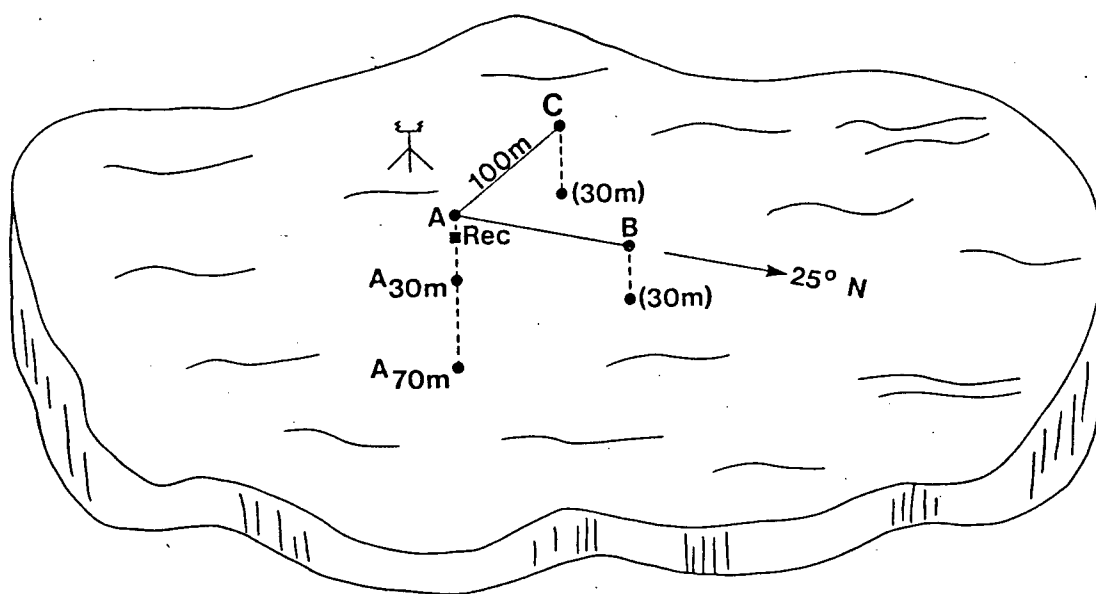
Figure 2.2: Deployment configuration of the hydrophone array and recording system (Rec) of the 1987 Ambient Sound Experiment in Amundsen Gulf.

2.2 Instrumentation

The deployment consisted of a recording anemometer, an air temperature and a snow temperature sensor, recording current meters, and a broad-band recording acoustic instrument with four hydrophones. All these instruments were deployed near the array centre labelled as **D** in Figure 2.1. Figure 2.1 also shows the location of a nearby conductivity-temperature-depth (CTD) profile obtained on March 27, 1987. The array deployment is shown in Figure 2.2, and Tables 2.1 and 2.2 give respectively details of performance of hydrophones used in the experiment and deployment periods.

Hydrophone	Low-frequency cutoff($-6dB\ V$)	Sensitivity $re:1V\ \mu Pa^{-1}$	Radiation pattern
A MetOcean NH4123	32 Hz	$-187\ dB$	Omni
B, C MetOcean NH4123	200 Hz	$-160\ dB$	Omni

Table 2.1: Summary of hydrophone parameters.

Deployed	22:00:00,	17 March 1987 UT
Deploy site:	70°46.13′ N;	127°23.01′ W
Recover site:	71°02.40′ N;	129°50.00′ W
Data starts	23:00:00,	17 March 1987
Data ends	20:05:30,	23 March 1987
Drift distance:	90 km	

Table 2.2: Summary of Deployment and Recovery.

Three hydrophones were located at the vertices of a right-angle triangle of side

$100m$ at a depth of $30m$. The fourth hydrophone was at a depth of 70 m. All the hydrophones were connected by cables beneath the ice to the control and recording system, which was itself suspended in the water. While this arrangement complicated deployment, it maintained the electronics at a reasonable temperature ($\sim -2°C$) and gave protection to the cables. A small computer switched on the recorder for $5.5min$ once every hour, provided a recording time of approximately $13hr$ of data over the 6-day deployment. Data were stored in two forms on a video cassette recorder. Signals from the two hydrophones in the vertical component of the array (A_{30} and A_{70}) were digitally processed using a pulse code modulator (PCM) for storage on the video channel. The two remaining channels were recorded as analog signals on the tape. The analog channels incorporate automatic gain control; precise amplitude levels cannot subsequently be recovered from these two channels, although accurate pulse arrival times can be determined. The two digital channels, however, are linear, and the large bandwidth ($22\ kHz$) and dynamic range ($90\ dB$) allow recordings of high quality.

On play back, the digital signals are transferred directly to a computer; the analog signals were digitized at the same speed and resolution as the PCM channels and also transferred to a computer. Timing marks at 30 second intervals, written on to all four channels during recording, are subsequently used to correct for a differential lag between digital and analog channels. The two digital channels are sampled synchronously, but a very small discrepancy between clock rates during initial recording of the digital signals and subsequent digitization of the analog channels was determined from the sample count between timing marks. A correction was made, yielding time information for all four channels with an error less than $1ms$.

2.3 Results

Wind, air temperature, water current, snow temperature, and a summary scan of sound level variability for the first 2 days of the experiment are shown in Figure 2.3. On March 18, the wind was light and variable, but the following day the speed picked up from the east, rising through $5 \ m \cdot s^{-1}$ at 1500 h. This is similar to the wind speed at which Milne [26] detected an acoustic signal that he attributed to the impact of blown snow crystals. However, our measurement of the wind-induced noise beneath the ice cover shows that a well-defined spectral peak appears at about $6kHz$, which is much higher than that observed by Milne [26].

The air temperature at 5 m was typically about $6°C$ below zero, and slightly more variable than the temperature 1 cm above the ice surface. The snow was about 5 cm deep. The measurement period did not include large temperature excursions, but there is a modest diurnal variation of about $6°C$. The currents are predominantly semidiurnal; there is little mean flow, and tidal amplitude is $8 \sim 10 \ cm \cdot s^{-1}$. The major axis of the tidal ellipse is NW–SE.

Acoustic variability is calculated from sets of 1.5-sec data segments based on data from hydrophone A_{30}. The second moment is found for each segment; for a succession of each of 20 consecutive values, spanning a period of 30s, the maximum calculated value is then plotted in Figure 2.3. This technique proved successful in identifying individual cracks, several of which can be seen between 0900 and 2100 h on March 18. At about the time that the wind speed rose above $5 \ m \cdot s^{-1}$, there is a noticeable increase in acoustic variability. It should be emphasized that the acoustic record is based not on continuous data, but on 5.5-min sampling segments once each hour.

Results from the CTD profile are shown in Figure 2.4. The sound- speed profile is upward refractive, with a relatively cool fresh layer extending over the upper 35 m. A temperature inversion at 40 m results in a small sound channel at the same depth; the small-scale structure has not been included in the subsequent refractive

corrections, however, and I represent the profile by a uniformly increasing sound speed ($dc/dz = 0.057s^{-1}$), which is shown by a dashed line in the figure.

From the acoustic data set, I examine four events in detail. The choice is based on the acoustic variability time series and indicated in Figure 2.3. Some other acoustic transients from the same period of light winds were also examined; the selection presented here appears representative. The quite different signals associated with wind and acoustic effects of mobilization of the ice field will be discussed in Chapter 4.

Time series plots of sound pressure from each hydrophone for a period of 220 ms are shown for each event in Figures 2.5, 2.6, 2.7 and 2.8. Event I consists of a short pulse followed after 30 ms by a longer and louder pulse. The dominant frequency is ~ 500 Hz. Events II, III and IV are different: A pulse of frequency $150 \sim 250$ Hz has a much higher frequency superimposed over the first a few cycles. The presence of higher frequencies is most clearly seen in Figure 2.8, The main pulse is repeated at 30- and 90-ms intervals in event IV, but with a much smaller, or negligible, high-frequency content.

The locations of each event are determined from the arrival times of the direct path pulses at different hydrophones. A ray-tracing model is set up based on the linear sound-speed profile in Figure 2.4 to estimate ranges of cracking sources to my array centre. Consistency in the position fixing procedure was checked, using hammer blows on a metal pipe inserted through holes in the ice at the known locations above each hydrophone. According to the calculation, the source ranges of events I and IV to the array centre are estimated as 1560 and 2270 metres respectively.

Due to the shallow water environment, cracking sounds arrive at the hydrophones through several paths in addition to the direct path, causing a multi-path effect on the received signals. Figure 2.9 shows the main paths through which acoustical energy associated with events I and IV arrives at a hydrophone beneath the ice. It is seen that sound striking the sea-floor, at a depth of ~ 200 m, is reflected and
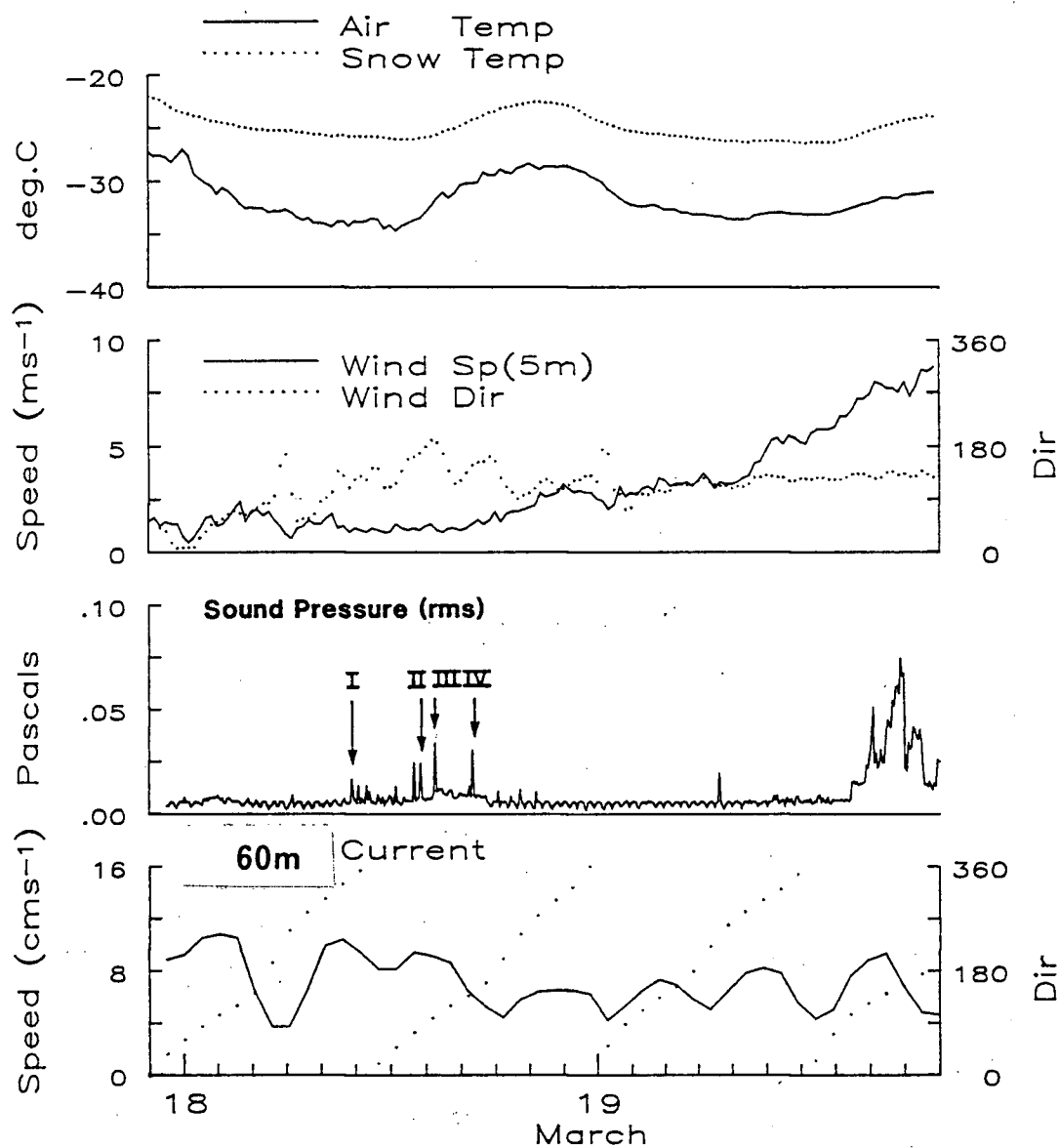
Figure 2.3: Overview of field data. Time series records of air temperature (5 m), snow temperature (1 cm above the ice), wind speed and direction(5m), rms sound pressure level based on A_{30}, and current speed and direction (60 m). Arrows identify 4 individual events.
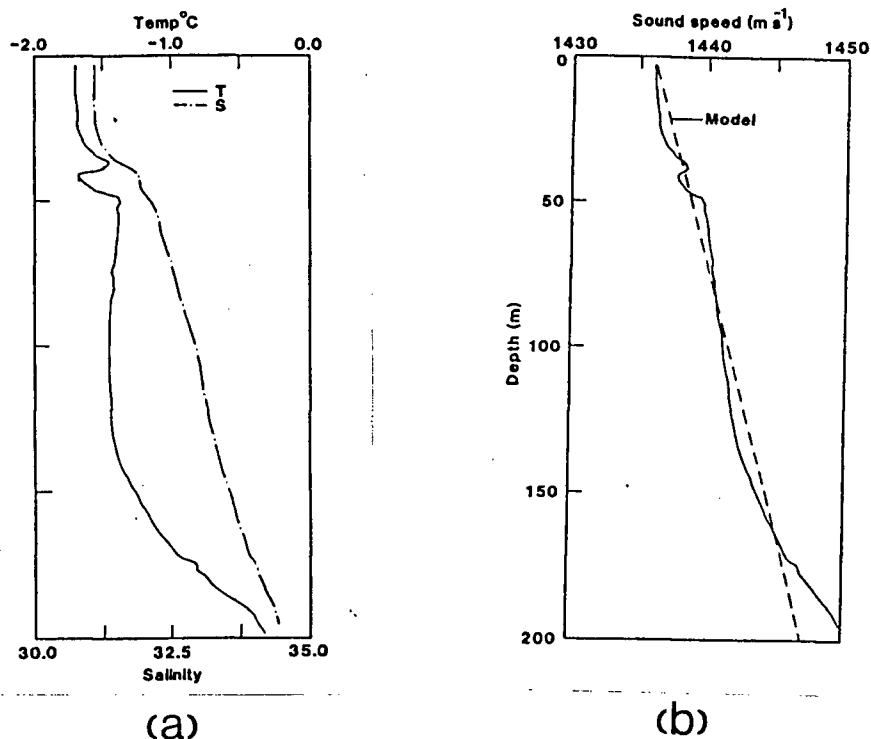
Figure 2.4: CTD and sound speed profiles near the site of the 1987 Ambient Sound Experiment.(a) Temperature and salinity profiles. (b) Derived sound speed profile which is modeled with a uniform sound speed gradient $C'(z) = 0.057$ s^{-1} (dashed line).

observed at the array after the direct signal. These reflections may also be used to fix the location of the sources, providing some redundancy in the data and confirming the acoustic interpretation. An especially clear-cut example is event I (Figure 2.5). The direct path signal arrives first, followed by a strong reflection. The time delay between direct and reflected paths is greater at A_{30} than at A_{70}, consistent with the geometry. The eigenvalue search procedure using the ray-tracing model confirms the source location to within 5 m of that found from the direct path with allowance for refraction; thus the bottom reflections provide additional arrival time information increasing the effective vertical aperture of the array. Multiple reflections can also occur (see Figure 2.9(b)). In event IV, a bottom reflection arrives approximately 30 ms after the direct path, and a bottom-surface-bottom reflection arrives $\sim$ 90 ms later.

The relative signal strengths of direct and reflected paths are related to the source radiation pattern and reflection coefficients of ice and seabed. For a monopole source in an ice sheet, Stein [23], [24] has found that the acoustic radiation has a dipole pattern. Under this assumption, a sonar equation can be solved to determine a seafloor reflection coefficient for the base frequency (150 $\sim$ 500 Hz) of 0.55 at an incident angle of 2.6° (with horizontal direction) for event I. The reflection coefficient found from the artificially generated sound is 0.15 $\sim$ 0.18 for normal incidence; as reflectivity increases at shallow angles. These results may be compared with previously reported values of 0.6 at an angle of 2.5° and 0.25 at normal incidence (Mackenzie [27]). A similar analysis for the multiple reflection of event IV is consistent with a reflection coefficient of 0.15 at 0.8° at the ice-water interface. However, the high-frequency component is essentially lost in all the reflected signals, most likely being scattered by roughness elements on the sea-floor and ice bottom.
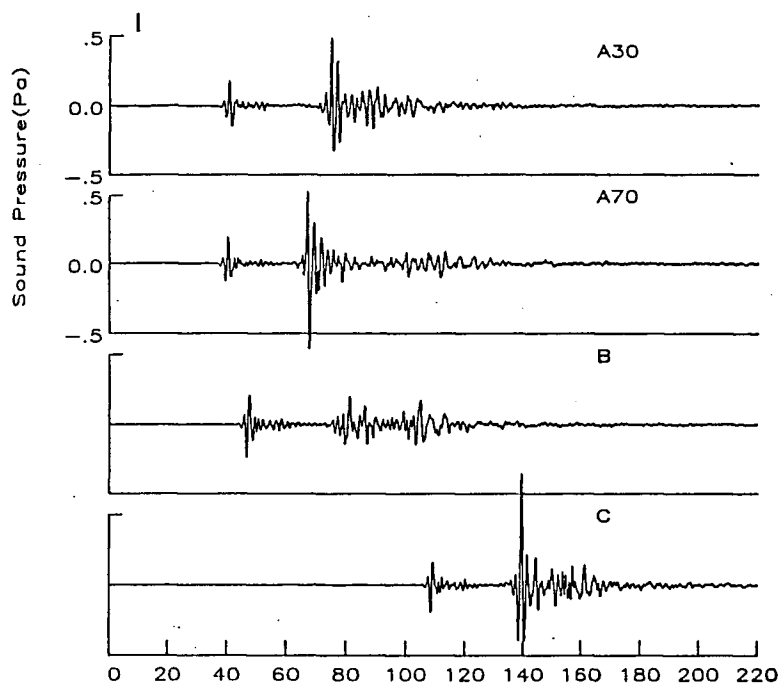
Figure 2.5: Sound pressure time series of each hydrophone for event I of 1987 experiment. Sound pressure levels are only indicated for hydrophones A_{30}, A_{70}.
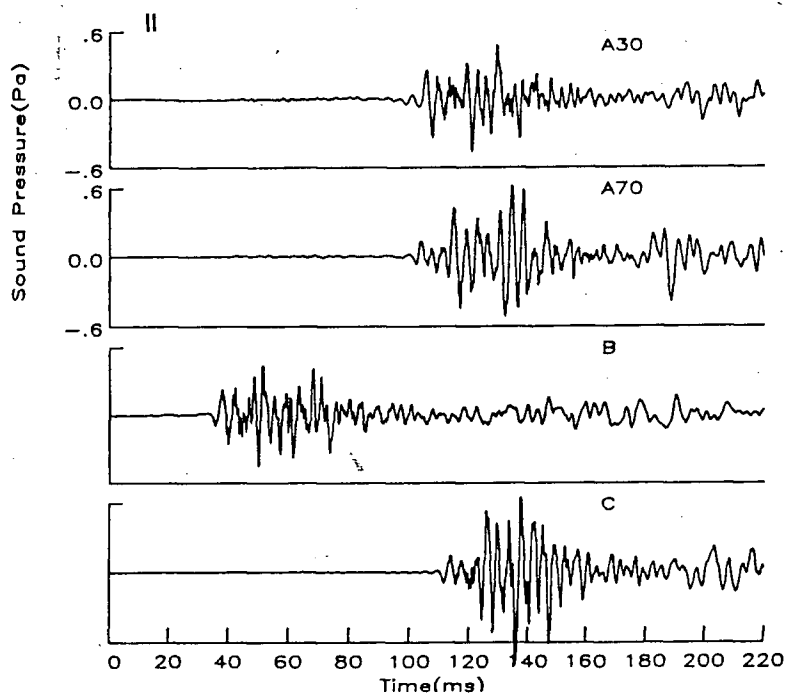
Figure 2.6: Sound pressure time series of each hydrophone for event II.
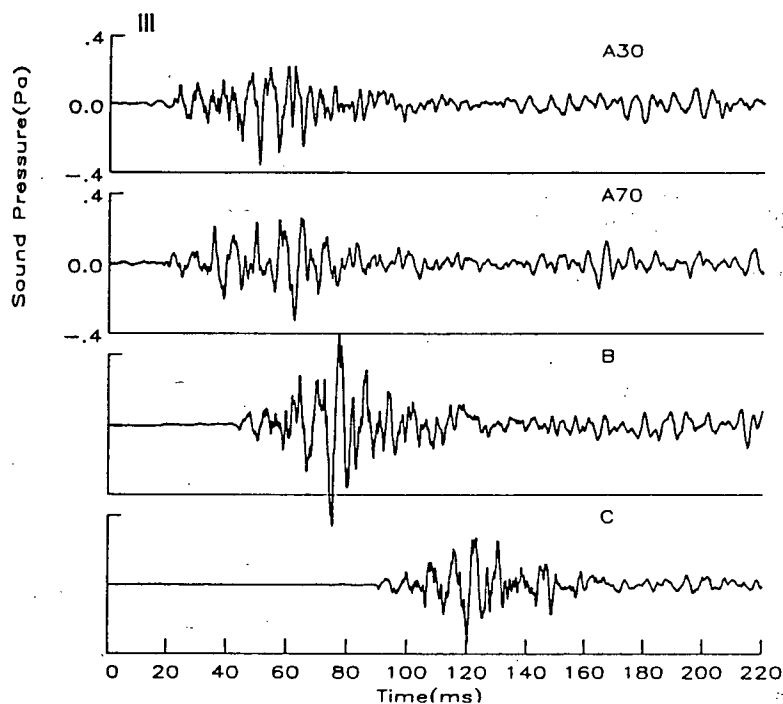
Figure 2.7: Sound pressure time series of each hydrophone for event *III*.
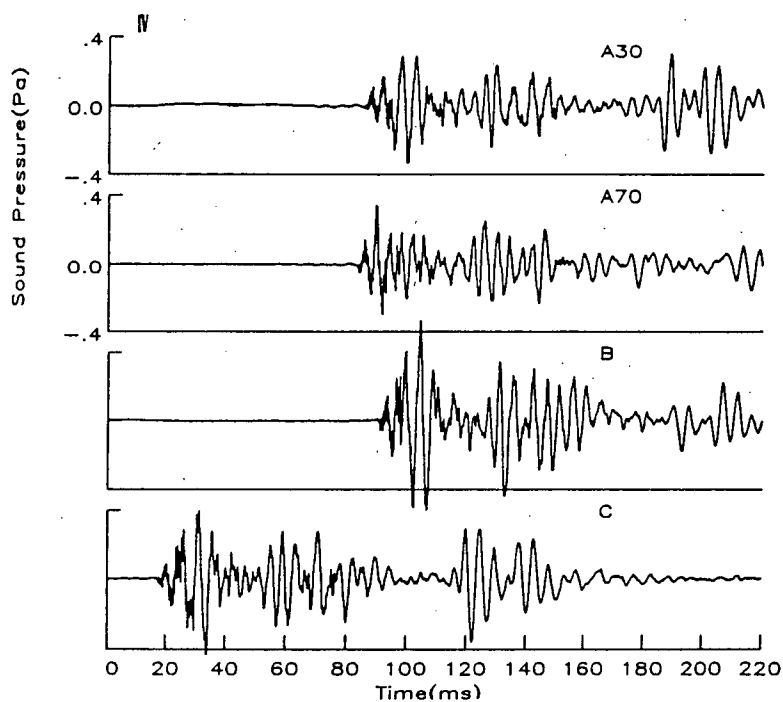
Figure 2.8: Sound pressure time series of each hydrophone for event *IV*.
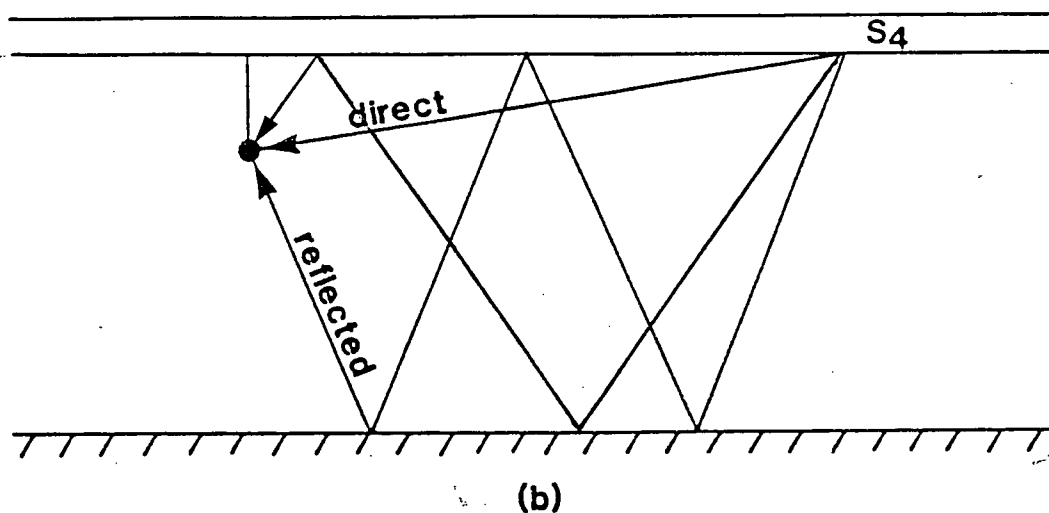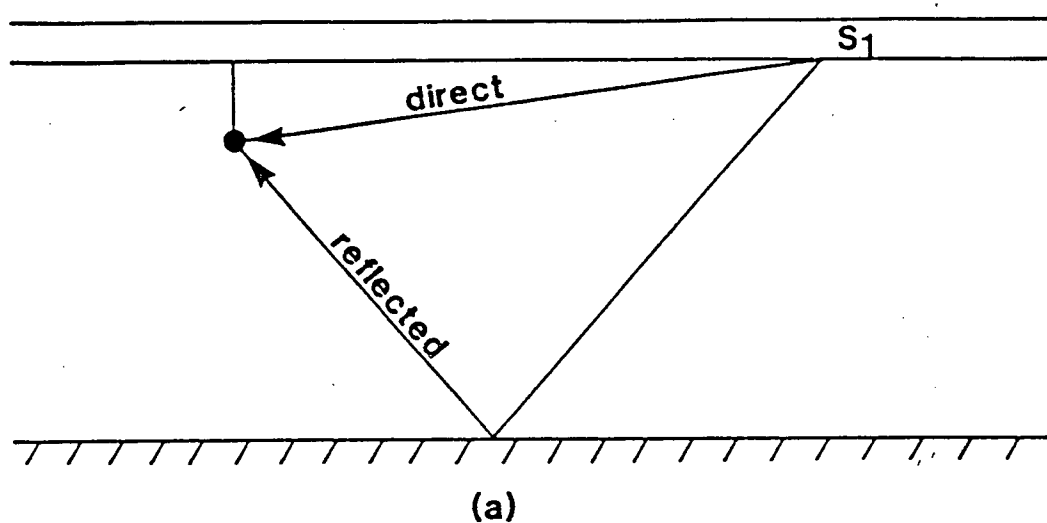
Figure 2.9: Sketch of inferred ray paths: (a) direct and single reflections observed for event I, (b) double and triple reflections observed for event IV.

2.4 A Seismic Model for the Ice Cracking Process and An Underwater Sound Field due to a Moving Fracture in the Ice Cover

I am interested in the relationship between the acoustic signal detected in the water and the physical process responsible for its generation in the ice. Stress relief in an ice sheet can be expected to have features in common with stress relief in the earth's crust, and earthquake mechanics provide a useful starting point for examining the acoustic signals. An excellent introductory textbook to earthquake mechanics was written by Kasahara [28]. Dyer noticed the similarity between earthquake seismology and cracking source mechanics in sea ice [29]. Kim [30] classified ice cracking sources in terms of seismic motion associated with various earthquake sources. A consolidated floating sheet of sea ice typically has a high aspect ratio: Its horizontal extent may be tens or hundreds of kilometres, while its thickness is only $1 \sim 3~m$. Moreover, buoyancy effects tend to resist its deformation and buckling under compression. Its strength in compression much exceeds its strength in tension or shear. I suspect that tensile cracking and shear failure are the major contributors to ice noise.

I am dealing with three linearly independent modes of motion of a crack, which are commonly discussed in earthquake mechanics (see [5]). They are:

1. Longitudinal shear fault, in which the relative displacement is parallel to the direction of crack propagation. This fault will excite SH modes in an ice cover. One of the geophysical examples associated with this fault is ice rubbing (see Chapter 4);

2. Transverse shear fault, where the displacement is normal to the crack propagation vector, yet remains in the fault plane. This type of fault is not commonly seen in ice fields, but can be generated by artificial means, for example, hammer blows (see Chapter 3);

3. Tensile fault, in which the displacement vector is normal to the fault plane. It is the common fault which occurs in the Arctic sea ice because of the lower tensile strength of sea ice. Tensile faults can be created by various forcing mechanisms, for example, internal stress in an ice floe; thermal stress at the ice surface, etc.

Judging from the results present in Figure 2.3, I see no close correlations between the four acoustical events and environmental variations. As a matter of fact, the environment was very quiet when the four individual cracks occurred. I suspect that a large scale internal stress transmitted through the ice was responsible for these ice cracking events, and the type of failure was probably tensile at least for event IV. The process of tensile failure excites strong P waves in the ice which may be observed in the water. Indeed, distinct P wave signals were observed in event IV (see Figure 2.11). Since I do not have enough information to specify failure types for the other three events, I will call the four events analysed in this chapter *large scale cracking events*.

The observations illustrate two features that must be reconciled with any model of the cracking process. First, event IV exhibits more than one well-separated frequency component: a high-frequency signal of relatively small amplitude superimposed on the lower frequency "base-band" component. Figure 2.10 shows the time evolving power spectrum of event IV. This, and subsequent similar spectra are calculated using the Maximum Entropy Method developed by Burg [31] with colours being assigned for different spectral levels. The routine is given in Press, *et al*, [32]. Second, although having a similar amplitude envelope at the different hydrophone locations, the signals in events II and III are quite distinct in detail. Table 2.3 lists maxima of cross-correlation among 4 hydrophone channels for each event.
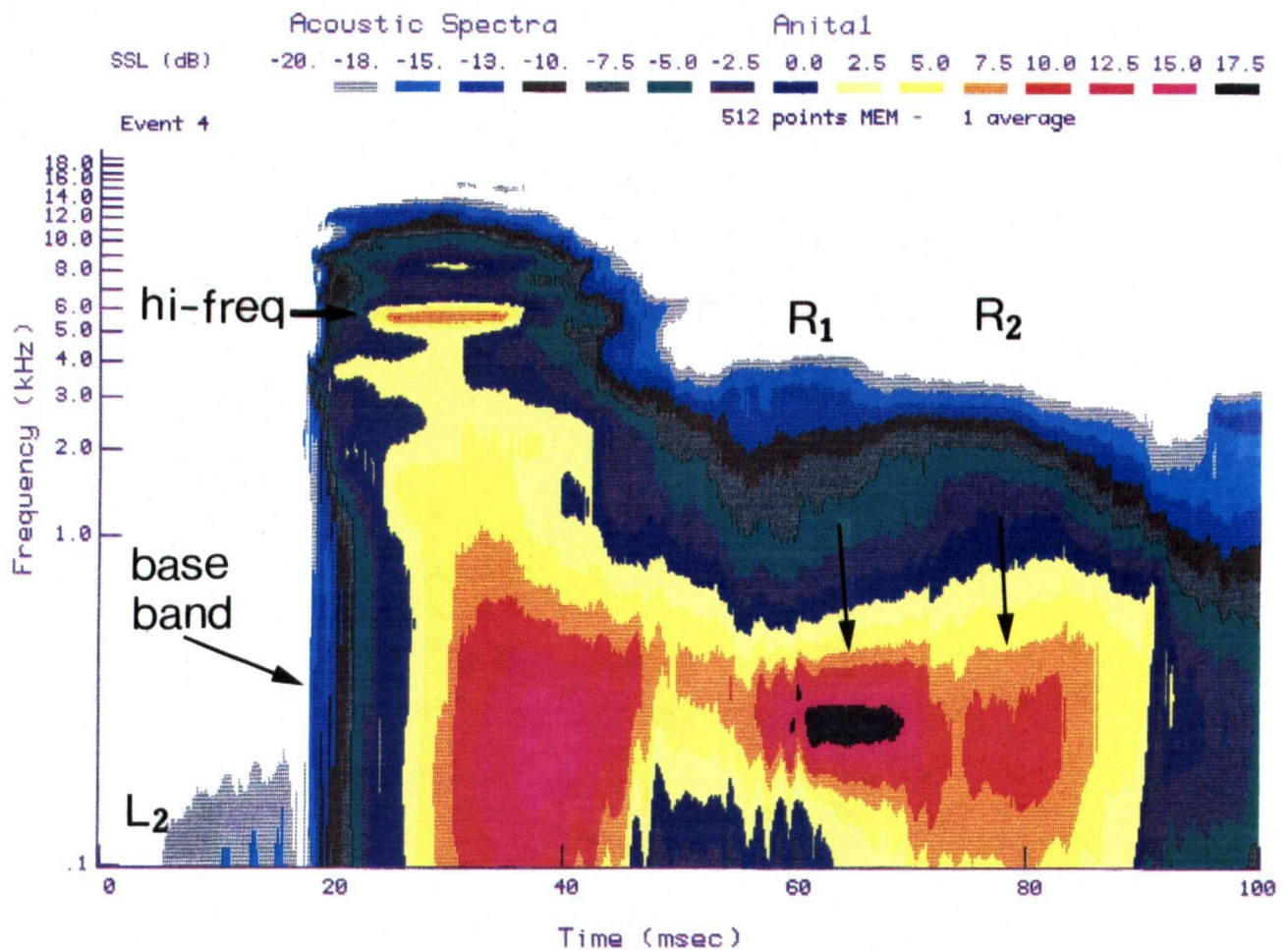
Figure 2.10: Spectral intensity (indicated by colours) of event IV signal, showing second P wave (L_2), direct path signals, and reflected signals from sea floor and ice. An $11ms$ wide window moving at a $0.2ms$ step is used as a moving filter on the raw data for spectral calculations; a mean slope ($-14dB/decade$) has been subtracted from the spectrum.

Event	Range, m	Hydrophone	Cross-correlation	Mean
I	1560	A_{70}	0.881	
		B	0.811	0.80
		C	0.706	
II	255	A_{70}	0.513	
		B	0.556	0.51
		C	0.466	
III	295	A_{70}	0.379	
		B	0.376	0.37
		C	0.354	
IV	2270	A_{70}	0.512	
		B	0.706	0.63
		C	0.659	

Table 2.3: Cross-correlation maxima for direct path signals of the 4 events. A_{30} is chosen as reference channel.

My interpretation of these features is, first, that there is more than one scale associated with the cracking process, and second, that by analogy with results of theoretical models of propagating earthquake cracks, the source moves with the developing crack. The two primary length scales associated with a crack are those of horizontal and vertical extent; moreover, there is no reason to suppose that the cracking process will always be free of finer scale features which contribute to the signal.

Although little energy appears to radiate from the ice sheet far from the source, I can identify some of the components in my data. Stein [24] has observed radiation from flexural waves using a hydrophone 1 m below the ice; however, the evanescent nature of this radiation, and the fact that our hydrophones are 30-m deep, make it

hard to detect. On the other hand, there are two forms of longitudinal waves in the received signal of event IV.

Figure 2.11 shows an expansion of the record from A_{30}, event IV. The first signal, with a frequency of 200 Hz, corresponds to radiation from the longitudinal or P wave. Its identity is confirmed by the delay of approximately 20 ms between 30 and 70 m, corresponding to a radiation angle of 62° (with horizontal direction), and an arrival time that is 812 ms ahead of the direct path acoustic signal at 30-m depth.

Just before the arrival of the direct path acoustic wave, a second 200-Hz signal appears. From the frequency content of the signal, I believe that this is a longitudinal wave excited by the cracking. However, as far as its propagation path is concerned, there are two possible cases explained in the following:

1. This signal is consistent with a longitudinal wave that has undergone successive reflections in the ice cover at the upper and lower surfaces. From the arrival time and source range, an internally incident angle of 60° (with the horizontal) is obtained for this so called *reflected longitudinal wave*;

2. This signal is from the same origin as the first arrival longitudinal wave (see Figure 2.11). However, this part of the P wave energy is radiated into the water from the ice region near the crack. Once the wave enters the water, its speed is the same as that of acoustic waves, but its frequency is determined by the ice cover waveguide. Since most of the path for this signal is in the water, the wave arrives at the hydrophone almost at the same time as the direct path acoustic wave, the spectrum of which is determined by the mechanical properties of the ice at the source region as well as the actual seismic motion during crack formation.

Based on the fact that ice is a highly attenuating medium for P waves, it seems that the possibility of case 1 is slim, but not zero. Lacking information about source
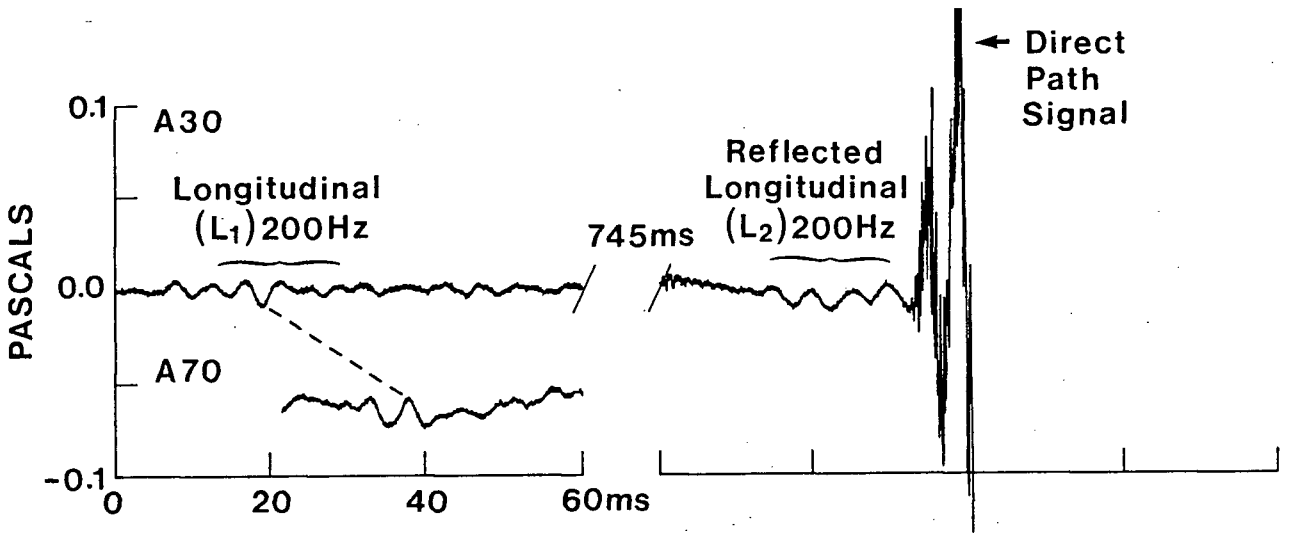
Figure 2.11: Expanded time series for event *IV* showing arrival (to A_{30}) of primary (L_1) and secondary (L_2) *P* waves, and direct path acoustic wave. Also shown is L_1 wave received by A_{70}.

levels of the longitudinal waves associated with this event, I will call this later-arrival longitudinal wave *the second P wave.*

The spectral image in Figure 2.10 shows the second *P* wave, the direct path signal with both base-band and high-frequency components, the sea floor and sea floor – ice bottom reflections (R_1 and R_2). Each of these components of the signal is readily distinguishable by its arrival time and frequency. It is clear from these results that the direct acoustic transmission dominates the observed signal.

In the following, I consider a simplified representation where waves associated with shear deformation are ignored for now. As a result, the sound field is described by a scalar potential and the problem is equivalent to wave propagation in a multi-layered liquid (see Ewing, *et al.* [33], p. 126-131). I also neglect the wave energy that propagates in the ice, which my data show is of minor significance compared to the acoustic field observed in the water. Only the direct path acoustic waves are considered. Although the model treats the ice as a fluid under these assumptions, the model allows for an easy implementation of a seismic model describing
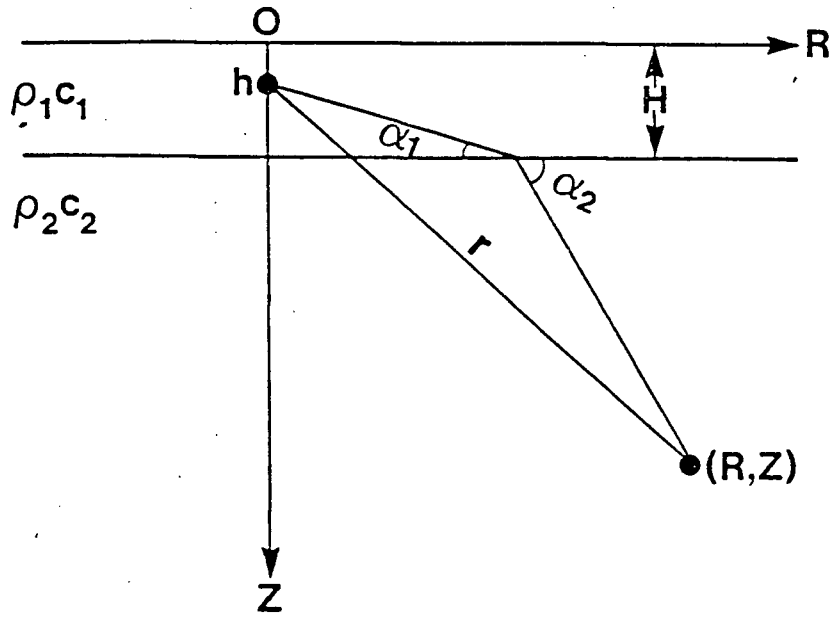
Figure 2.12: Cylindrical coordinate system $(R, \ Z)$, with a slant range r, used for a point source model.

ice breaking processes and I gain an analytical result that provides useful insight on the connection between the directly transmitted signal and source.

A more comprehensive model is, of course, preferable, for example Schmidt and Jensen's SAFARI model (Seismo-Acoustic Fast field Algorithm for Range-Independent environments) [34], or Stein's monopole model [23]. Owing to these models, otherwise inaccessible numerical solutions to elastic wave equations have been obtained in an air-ice-water system. However, these numerical models are computationally expensive and time consuming. Moreover, it is hard to get a clear physical insight from them. I believe that a simple theoretical model will be complementary to the existing numerical models, and deepen our understanding of ice failure processes.

Figure 2.12 shows a cylindrical coordinate system $(R, \ Z)$ used for the derivation of this theoretical model. Assuming the velocity potential, Φ, is harmonic in time, $\Phi_{1,2}(R, Z, t) = \Phi_{1,2}(R, Z)e^{-i\omega t}$ and $\Phi_{1,2}(R, Z)$ is a function of radius R in the horizontal plane and depth Z (see Figure 2.12), with the subscript 1,2 referring to

the ice and water respectively. For a time-harmonic point source located at $(R = 0,$ $Z = h)$, $\Phi_{1,2}(R, Z)$ satisfies the following Helmholtz equations:

$$\frac{1}{R}\frac{\partial}{\partial R}(R\frac{\partial \Phi_1}{\partial R}) + \frac{\partial^2 \Phi_1}{\partial Z^2} + k_1^2\Phi_1 = -4\pi\delta(R, Z - h), \qquad (2.1)$$

and

$$\frac{1}{R}\frac{\partial}{\partial R}(R\frac{\partial \Phi_2}{\partial R}) + \frac{\partial^2 \Phi_2}{\partial Z^2} + k_2^2\Phi_2 = 0, \qquad (2.2)$$

where $k_{1,2}$ is the wavenumber in the ice and water, respectively. The right-hand term in equation (2.1) represents a point source of unit strength. The corresponding boundary condition at the ice surface, neglecting the small coupling to the atmosphere, is then

$$\Phi_1 = 0, \qquad at \ \ Z = 0, \qquad (2.3)$$

which means that no waves are transmitted into the air. At the ice-water interface, both the vertical displacement and pressure should be continuous, i. e.

$$\left.\begin{array}{rcl} \frac{\partial \Phi_1}{\partial Z} & = & \frac{\partial \Phi_2}{\partial Z} \\[2mm] \\ \rho_1\Phi_1 & = & \rho_2\Phi_2 \end{array}\right\} \qquad at \ \ Z = H. \qquad (2.4)$$

At the source, I incorporate Pekeris's source condition (Ewing *et al.* [33] p. 130)

$$\frac{\partial \Phi_1}{\partial Z}|_{h^-} - \frac{\partial \Phi_1}{\partial Z}|_{h^+} = 2\int_0^\infty J_0(\eta R)\eta d\eta \ , \qquad (2.5)$$

where η is the horizontal wave number and $J_0(\eta R)$ is the zero order Bessel function.

Solutions to (2.1) to (2.5) are derived in Appendix A. Since I am concerned only with the direct acoustic propagation through the water, I only need the solution for Φ_2:

$$\Phi_2 = \int_0^\infty S(\eta)e^{i\beta_2(Z-H)}J_0(\eta R)\eta d\eta, \qquad (2.6)$$

and

$$S(\eta) = \frac{2\sin\beta_1 h}{m\beta_1 \cos\beta_1 H - i\beta_2 \sin\beta_1 H}, \tag{2.7}$$

where $\beta_1 = (k_1^2 - \eta_2)^{1/2}, \beta_2 = (k_2^2 - \eta_2)^{1/2}$ are vertical wave numbers in the ice and water respectively, and $m = \rho_2/\rho_1$. $S(\eta)$ given by the integrand of Equation (4-46) of [33] is the same as equation (2.7) except for a sign difference in their denominator. Using the method of stationary phase, (2.6) and (2.7) may be evaluated as (see Appendix A for detailed derivations)

$$\Phi_2(r,t) \approx \frac{k_2|\sin\alpha_2|S(\eta_0)}{r}e^{ik_2 r - i\omega t}, \tag{2.8}$$

where $\eta_0 = k_2 \cos\alpha_2$ and α_2 is the angle of refraction (see Figure 2.12). It is worthwhile pointing out that equation (2.8) represents only the principal value of the integral given by equation (2.6). This principal value describes the most important contribution of the monopole source to the underice sound field. A full solution of the integral will include the contribution of reflected sound from the air-ice interface or the contribution of normal modes, which will not be discussed in this thesis. Interested readers are referred to Ewing *et al*'s early work [33].

I have assumed a harmonic point source of form $e^{-i\omega t}$. Since the source will be of finite volume and frequency bandwidth for a real crack, the rate of volume change Q is

$$Q = \int_s U_s(t)ds = 2AU_s(t), \tag{2.9}$$

where $U_s(t)$ is the amplitude of the displacement velocity at the source and A is the area of the fault plane per unit length. The source model (2.9) incorporates the assumption that the sound is generated by a tensile crack acting uniformly over the area A, centered at depth h. This result is now applied to a more realistic source model.

Motivated by the structure of our observations and their similarity to those seen in certain earthquake records, I follow Haskell [35] and take a sinusoidally

roughened ramp function for the displacement of the fault planes, except that I allow the roughness elements to be some fraction ϵ of the primary amplitude. The physical concept here is of a "slip-stick" shear fault, or of a tensile fault where the yield point advances in small jumps determined by the thickness of the ice sheet. The normalized fault displacement is modelled as

$$G(t) = \begin{cases} 0 & t < 0 \\ \frac{1}{T}[t - \epsilon \cdot \frac{\sin(2n\pi t/T)}{2n\pi/T}] & 0 \le t \le T \\ 1 & t > T \ . \end{cases} \qquad (2.10)$$

where n is an integer equal to the displacement roughness elements in the fault formation. If $\epsilon = 0$, equation (2.10) reduces to a linear ramp function. Figure 2.13 shows the displacement function for a roughened fault ($n = 4$, $\epsilon = 0.5$), together with the corresponding displacement velocity:

$$\frac{dG(t)}{dt} = \begin{cases} 0 & t < 0 \\ \frac{1}{T}[1 - \epsilon \cdot \cos(2n\pi t/T)] & 0 \le t \le T \\ 0 & t > T \ . \end{cases} \qquad (2.11)$$

The slip or tear on the fault is presumably controlled by the narrowest dimension of the rupture surface, which is the ice thickness H. In earthquake mechanics, it is generally assumed that, at any given point, the crack continues to widen until the rupture front is $H/2$ past that point (Savage [36]). Following this assumption, I assume that the tear at a point begins as the rupture front passes that point and continues until a time roughly equal to $T = H/2v_r$, where v_r is the rupture velocity. I identify T as the rise time of the displacement function.

For a total fault displacement D_0 the speed of the fault planes at the source is then $U_s = D_0 G'(t)$, and its Fourier Transform is

$$\widehat{U}_s(\omega) = D_0 e^{i\omega T/2} \frac{\sin(\omega T/2)}{\omega T/2} \frac{1 - (1 - \epsilon)(\omega T/2n\pi)^2}{1 - (\omega T/2n\pi)^2} . \qquad (2.12)$$

If $\epsilon = 1$, this expression simplifies to
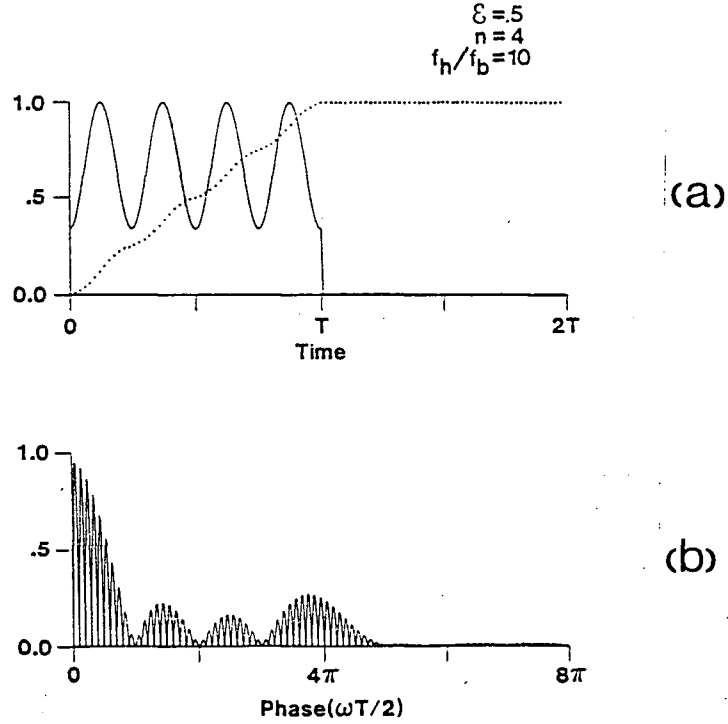
Figure 2.13: Seismic model for crack formation in the ice. (a) Model displacement function (dotted line) and corresponding speed for $\epsilon = 0.5$, $n = 4$. (b) Spectrum of model displacement speed for $f_h/f_b = 3$. f_h and f_b are related to depth and length of a crack through Eqs. (2.29) and (2.30) respectively .

$$\widehat{U}_s(\omega) = D_0 e^{i\omega T/2}\frac{\sin(\omega T/2)}{(\omega T/2)(1 - (\omega T/2n\pi)^2)}, \qquad (2.13)$$

which was originally derived by Haskell [35]. The rate of change of source displacement U_s can be expressed in terms of its transform:

$$U_s(t) = \frac{1}{2\pi}\int_{-\infty}^{+\infty}\widehat{U}_s(\omega)e^{-i\omega t}d\omega. \qquad (2.14)$$

From (2.9),

$$Q(t) = \frac{1}{2\pi}\int_{-\infty}^{+\infty}2A\widehat{U}_s(\omega)e^{-i\omega t}d\omega = \frac{1}{2\pi}\int_{-\infty}^{+\infty}\widehat{Q}(\omega)e^{-i\omega t}d\omega. \qquad (2.15)$$

It follows from (2.15)

$$\widehat{Q}(\omega) = 2A\widehat{U}_s(\omega). \qquad (2.16)$$

Equation (2.8) gives the velocity potential for a source of unit strength at a single

frequency ω. For a source of strength $\widehat{Q}(\omega)$, the corresponding velocity potential for a single frequency ω is then

$$\widehat{\Phi_2}(\omega) = \frac{\widehat{Q}(\omega)k_2|\sin\alpha_2|S(\eta_0)}{r} = \frac{2A\widehat{U}_s(\omega)k_2|\sin\alpha_2|S(\eta_0)}{r}. \qquad (2.17)$$

For a source of finite bandwidth, the velocity potential is found by integration over frequency space:

$$\Phi_2(t) = \frac{1}{2\pi}\int_{-\infty}^{+\infty}\widehat{\Phi_2}(\omega)e^{-i\omega t}d\omega = \frac{2Ak_2|\sin\alpha_2|S(\eta_0)}{2\pi r}\int_{-\infty}^{+\infty}\widehat{U}_s(\omega)e^{-i\omega t}d\omega. \qquad (2.18)$$

At a point distant r from the source,

$$\Phi_2(t - \frac{r}{c}) = \frac{2Ak_2|\sin\alpha_2|S(\eta_0)}{2\pi r}\int_{-\infty}^{+\infty}\widehat{U}_s(\omega)e^{ik_2r-i\omega t}d\omega, \qquad (2.19)$$

which is the delayed signal in the water due to direct acoustic transmission from a crack of unit area A. Thus Φ_2 is the Green's function for my moving source model, while c is the mean sound speed in water. The directly transmitted signal for a moving source is then found by integration of (2.19) over the length of the crack (Kasahara, [28] pp. 103-104).

I now define a new coordinate ζ that moves with the source from the epicentre ($\zeta = 0$) to the two ends of the crack length ($\zeta = \pm L$). Figure 2.14 illustrates this new coordinate. In terms of the acoustic pressure, $P = \rho\frac{\partial\Phi}{\partial t}$, the total field of sound pressure at the point of observation (see Figure 2.14) is

$$\begin{aligned}
P_2(r,t) &= \rho_2\int_0^L\frac{\partial}{\partial t}\Phi_2(t - \frac{r}{c} - \frac{\zeta}{c}(\frac{c}{v_r} + \cos\theta))d\zeta \\
&\quad + \rho_2\int_0^{-L}\frac{\partial}{\partial t}\Phi_2(t - \frac{r}{c} - \frac{\zeta}{c}(\frac{-c}{v_r} + \cos\theta))d\zeta \\
&= \frac{\rho_2 L}{\tau_+}[\Phi_2(t - \frac{r}{c}) - \Phi_2(t - \frac{r}{c} - \tau_+)] \\
&\quad + \frac{\rho_2 L}{\tau_-}[\Phi_2(t - \frac{r}{c}) - \Phi_2(t - \frac{r}{c} - \tau_-)] \qquad (2.20)
\end{aligned}$$

where
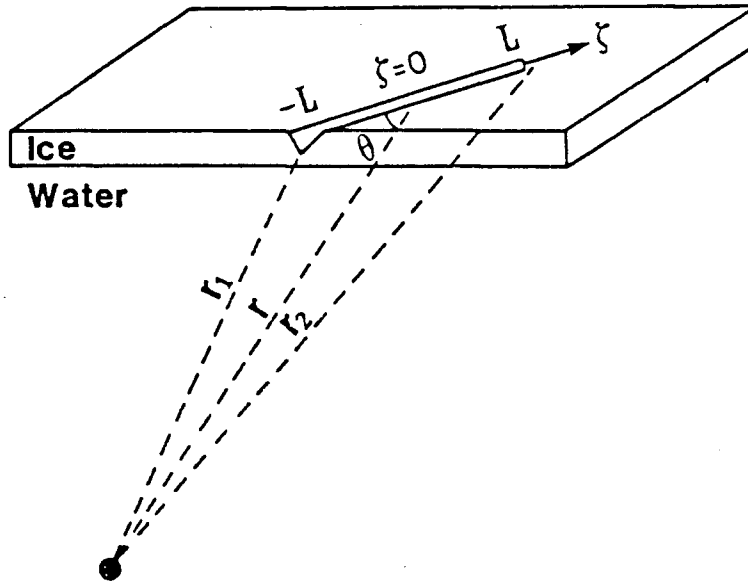
Figure 2.14: Sketch of spreading crack showing coordinate system ζ with origin at epicentre.

$$\tau_+ = L(c/v_r + \cos\theta)/c,$$

$$\tau_- = L(c/v_r - \cos\theta)/c. \tag{2.21}$$

v_r is the crack propagation speed and θ is the crack orientation (see Figure 2.14). I have made the far-field assumption that the length L of an acoustically identifiable segment of the crack is short relative to its range r.

The magnitude of the Fourier Transform of (2.20) is

$$|\hat{P}_2(\omega)| = \omega\rho_2 L|\Phi_2(\omega)||F_2(\omega,\tau_+,\tau_-)|, \tag{2.22}$$

and $F_2(\omega,\tau_+,\tau_-)$, the effect of bilateral propagation of the crack on the sound spectrum, is

$$F_2(\omega,\tau_+,\tau_-) = \frac{1}{2}[(F_1(\omega,\tau_+))^2 + (F_1(\omega,\tau_-))^2$$
$$+ 2F_1(\omega,\tau_+)F_1(\omega,\tau_-)\cos(\omega(\tau_+ - \tau_-)/2)]^{1/2}, \tag{2.23}$$

where

$$F_1(\omega, \tau) = \frac{\sin(\omega\tau/2)}{\omega\tau/2},$$

(2.24)

is associated with unilateral propagation of the crack.

The crack is assumed to travel in both directions away from the epicentre, but I can most easily identify the effect of crack propagation on the detected signal by considering the unilateral propagation case only, i. e. I retain only the first term [ ] in (2.20), and drop the subscript to τ. The magnitude of the Fourier Transform of this expression is then

$$|\widehat{P}_2(\omega)| = \omega\rho_2 L|\Phi_2(\omega)||F_1(\omega, \tau) = \omega\rho_2 L|\Phi_2(\omega)|\frac{\sin(\omega\tau/2)}{\omega\tau/2}.$$

(2.25)

The Fourier Transform of $\Phi_2(t - r/c)$ is obtained from (2.12) and (2.19):

$$|\Phi_2(\omega)| = \frac{2AD_0k_2|\sin\alpha_2||S(\eta_0)|}{r}\frac{\sin(\omega T/2)}{\omega T/2}\frac{1 - (1 - \epsilon)(\omega T/2n\pi)^2}{1 - (\omega T/2n\pi)^2}.$$

(2.26)

Combining (2.25) and (2.26),

$$|\widehat{P}_2(\omega)| = \frac{m(\rho_1 V_0)k_2|\sin\alpha_2||S(\eta_0)|}{r}[\frac{\sin(\omega T/2)}{\omega T/2}\frac{1 - (1 - \epsilon)(\omega T/2n\pi)^2}{1 - (\omega T/2n\pi)^2}][\frac{\sin(\omega\tau/2)}{\tau/2}].$$

(2.27)

The quantity $V_0 = 2HLD_0$ can be interpreted as the volume of ice expelled from the crack during the process of sound generation; $\rho_1 V_0$ is the expelled mass and $m = \rho_2/\rho_1$ is the density ratio.

Thus the sound pressure spectrum is proportional to the product of two terms (in square parentheses in equation (2.27)). The first represents the envelope of the source while the second shows the effect of the source motion. The source spectrum has the argument $\omega T/2$, where $T = H/2v_r$, which is determined by the time taken for the crack to propagate through the ice depth. I model the fault displacement speed as the product of a rectangular function and a sine wave (2.11). The corresponding argument of the source motion term is $\omega\tau/2$, where $\tau = L/v_r$ for $\cos\theta = 0$ is determined by the time taken for the crack to propagate over a path of length L.

An identical result occurs for propagation to $-L$. The source motion introduces nulls in the spectrum at $\omega\tau/2 = 0, \quad \pi, \quad 2\pi, \ldots$.

The combination of large and small scale components of the crack, together with the crack propagation, determine the form of the signal detected in the water. Fracture of the ice from its surface to a certain depth d (which for larger cracks will be the ice thickness) takes a time T, the rise time, which depends on the ratio d/v_r. This is the general process and is described by a rectangular modulation of the pulse of width T as described by (2.10) and shown in Figure 2.13. A rectangular pulse concentrates most of its energy at low frequencies and provides the necessary condition for the existence of a base frequency signal in my data. The dominant component of the base band signal however is determined by the modulation of the source spectrum resulting from its motion. If the source remained motionless, the dominant base band signal would be determined by the rise time T. However its motion at speed v_r over the crack length L introduces a sequence of lobes, the first of which will be dominant. One would not necessarily expect identifiable nulls in the spectrum to occur as indicated in (2.27), since in a real environment the source will never be perfectly coherent. However, source motion will alter the spectrum and ensure that the details of the detected signal will vary with hydrophone position at least in the near field.

For given values of n and T, the envelope of the spectrum is defined and expressed by the first term in square parentheses in equation (2.27). However, the second term in square parentheses in (2.27) depends upon τ, and thus on the crack orientation with respect to the hydrophone. This term defines the fine structure in the spectrum, since, typically, $\tau \gg T$. In the near field, the angle θ and, hence, τ, will be a stronger function of hydrophone location than in the far field, which probably is responsible for the higher correlations observed between hydrophones for the more distant events (I and IV) than for the nearby events (II and III).

The effect of different propagation delays τ can be seen by considering an asymp-

totic example. If $\tau \sim T$, (2.27) reduces to

$$|\hat{P}_2(\omega)| = \frac{m(\rho_1 V_0)k_2|\sin\alpha_2||S(\eta_0)|}{r}[(\frac{\sin(\omega T/2)}{\omega T/2})^2\omega\frac{1-(1-\epsilon)(\omega T/2n\pi)^2}{1-(\omega T/2n\pi)^2}]. \quad (2.28)$$

In this case, there will be no maximum at $\omega = 0$, and no distinctive higher frequency component.

If $\tau > T$, I can identify two characteristic frequencies with which to describe the crack. This can be easily seen by calculating the spectrum of the acceleration G''', as shown by Haskell [35]. The high-frequency peak occurs at $\omega = 2n\pi/T$. This peak occurs at a slightly higher frequency in the velocity spectrum than that given by equation (2.27). Although, an analytical solution cannot be obtained for this case, numerical evaluation shows the relative error to be 0.0625 (see Figure 2.13 (b)). For the present purpose, I neglect this error and take the high frequency to be centered at

$$f_h = n/T = 2nv_r/d \quad (n > 1). \quad (2.29)$$

I define the base-band frequency as the location of the first peak of $\sin\omega\tau/2$, or,

$$f_b = 1/2\tau = v_r/2L. \quad (2.30)$$

The relative contribution of the high-frequency component will be governed by the physics of the cracking process. Figure 2.13 (b) shows the corresponding spectrum for $n = 4$, $\epsilon = 0.5$, and $T = 0.8\tau$.

2.5   Application of the Model to Data Interpretation

The essential features of the observations that I am seeking to explain are the predominant frequency components, both base and high frequency, and the difference in the signal between different hydrophones. I try to relate some of the observed acoustical features to seismic activities in the formation of a crack through the theoretical model derived in the previous section. The model interpretation is based on the crack propagation speed v_r, depth d, length $2L$, the number of crack roughness elements n, the relative amplitude of the secondary components ϵ, and the direction of propagation or crack orientation θ.

A close examination of the time series records (Figures 2.5– 2.8) reveals that for both events I and IV, the signals received by each hydrophone are very similar, while for events II and III there are much greater differences (see also table 2.3). I refer here to the relative amplitude of successive sound pressure fluctuations in the baseband signal. Both event I and IV are distant (1560 and 2270m, respectively), while events II and III are relatively close (255 and 295m). The frequency shift of each component in the signal, due to motion of the source, is a function of the component of source velocity resolved on to the vector determining the source position relative to the hydrophone; i. e. for frequency component ω_0, $\omega = \omega_0/[1 - (v_r/c)\cos\theta]$. For a nearby source, the orientation θ of this vector will differ significantly between hydrophones. In addition, there will also be a change in θ as the crack propagates, thus changing the frequency shift during the period of the pulse. This picture will be further complicated if the crack is not straight. The change in frequency shift will differ appreciably for different hydrophones, resulting in difference in the detected waveforms. For a distant source, the relative change in the source position vector for different hydrophones, as well as the relative source motion, will be less.

Event I lacks any significant high-frequency component and is much shorter than the others; I suspect that a different physical mechanism is responsible.
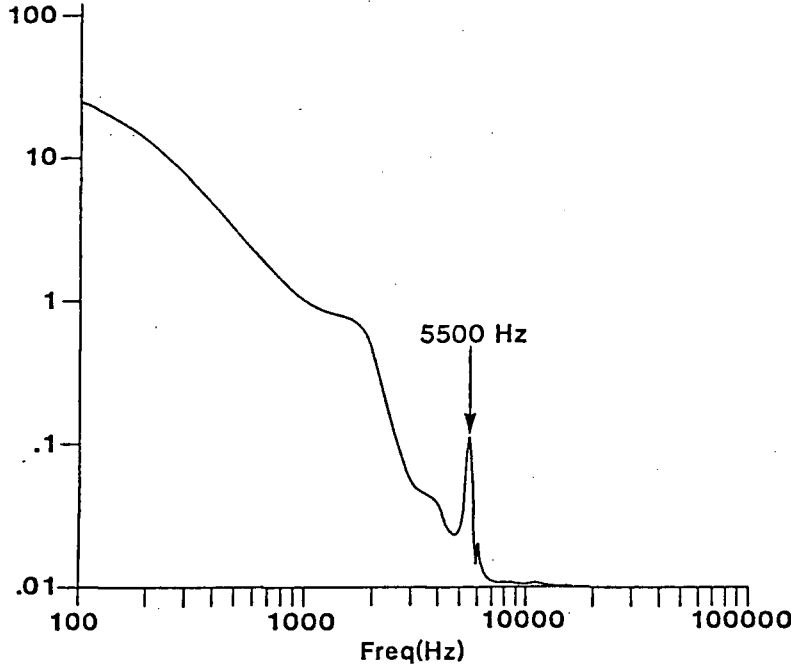
Figure 2.15: Normalized maximum entropy spectrum of 11 ms data segment for event IV (direct path signal) showing high-frequency peak at 5500 Hz.

Calculation of event parameters requires an assumption regarding the rupture velocity v_r. Mansinha [37] finds

$$v_r(max) \approx 0.63\beta, \qquad (2.31)$$

where β is the shear wave speed. Lacking independent information on crack orientation θ, I assume for simplicity that the crack is roughly perpendicular to the vector connecting our hydrophones and the centre of the crack ($\theta \approx 90°$). The high-frequency component is especially clear in event IV (see Figure 2.8 and 2.15), and $f_h = 5500$ Hz. I assume the ice broke throughout its depth of approximately $1m$. Then, from (2.31),

$$v_r = df_h/2n = 2750/n \quad (n > 1). \qquad (2.32)$$

Elastic rebound theory [28] stipulates that $v_r < \beta$; for sea ice, $\beta \approx 1900$ $m \cdot s^{-1}$, implying that $n > 1$. The maximum possible value of v_r would then be achieved for $n = 2$, which gives $v_r(max) = 1375 m \cdot s^{-1}$, consistent with (2.31). Events II

and *III* have similar high-frequency components, but they are not as well defined as in event *IV*. I, therefore, adopt this value in the remaining calculations. From equation (2.30), the crack's length is related to the base-band frequency as

$$2L = v_r/f_b. \tag{2.33}$$

Establishing f_b from the data, I list estimated values for L for each event in Table 2.4.

Event	Range (m)	f_b (Hz)	f_h (Hz)	ϵ	Coherent length, L_c (m)	High-freq duration (msec)	Max length, L_T (m)
I	1560	500	$\cdots$	$\cdots$	2.8	$\cdots$	$\cdots$
II	255	150	~ 5000	0.06	9.2	50	69
III	295	250	~ 5000	0.04	5.5	38	52
IV	2270	200	5500	0.12	6.9	20	27

Table 2.4: Event Parameters.

In a real crack, I do not expect the fine structure to be a simple sine function, nor do I expect the successive horizontal segments of the crack to be coherent with respect to each other. That is part of the reason why I prefer to use *frequency shift* instead of *Doppler shift* to describe the difference in received signals by different hydrophones. The calculated crack length, therefore, represents the minimum length, which in an average sense is derived from the coherent part of the transmitted signal. By *coherent*, I mean that the crack can be treated as a fault propagation analogous to a wave motion with a constant speed v_r. The total length can then be expressed as

$$L_T = \sum_{i=1}^{N} L_{ci},$$
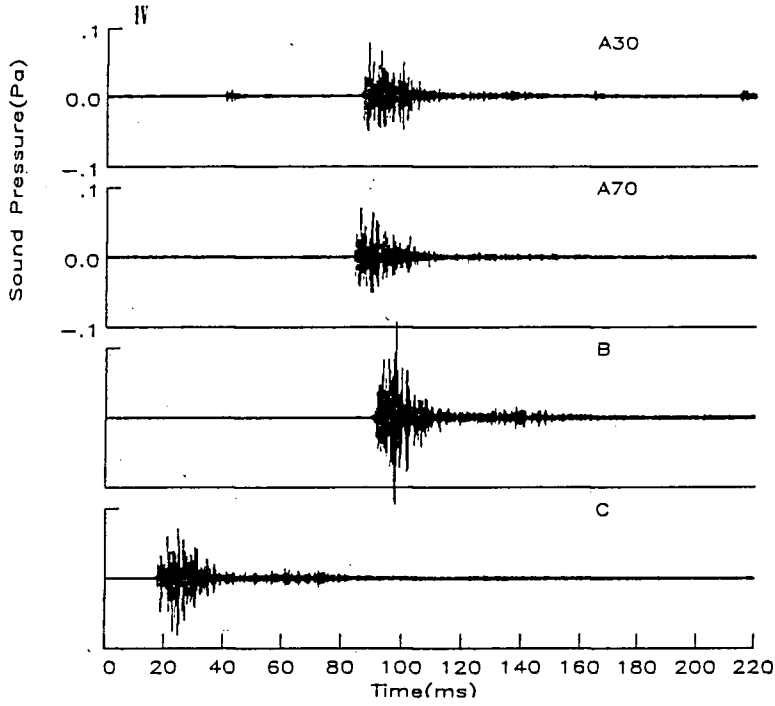
Figure 2.16: Time series of sound pressure for event IV, high-pass filtered at 2 kHz.

where L_{ci} is the length of the ith coherent segment, and the N is the total number of segments.

I can also obtain an independent estimate of crack length from the duration of the high-frequency component, which is not reflected from the sea floor and, therefore, lasted only as long as the source. It corresponds to a lower bound for τ_- and an upper bound for τ_+, since I take $\theta = 90°$. Figure 2.16 shows the high-pass filtered signal at $2kHz$ for event IV. Event IV evidently lasted for $20ms$. For $v_r = 1375m \cdot s^{-1}$, I find a maximum length of $27m$. From equation (2.33), the length of each coherent segment is $L_{ci} \sim 6.9m$, so that N is of order L_T/L_c, or approximately 4.

2.6   Concluding Remarks on Chapter 2

The 1987 experiment has demonstrated the importance of ice cracking sound radiation from the direct acoustic path to the ocean sound field. The ice cover is a waveguide of high attenuation; once a sound wave is trapped in this waveguide, little energy can travel along this path for a long distance (say greater than a few kilometres) and leak into the water. Nevertheless, leakage of P waves can be detected within a range of $1 \sim 2km$. Although the P wave's contribution to the under-ice sound field is negligible compared with the direct path acoustic signal, it reveals the acoustical properties of the ice cover. Earthquake mechanics appears to provide a useful starting point for developing models of the sound generation. An essential component of the sound generation mechanism appears to be the source motion, which is to be expected, since any realistic model of a developing crack must account for its propagation. However, it is worthwhile pointing out that the alternation of waveform of the detected sound can also be caused by a so-called angular frequency dependent radiation pattern associated with antisymmetric mode motion of the ice cover. I will examine this effect in chapter 3.

Without possessing a detailed model of the fracturing process, I assume by analogy with the theory of earthquakes that the rise time is controlled by the ice thickness, and that fine structure in the rupture is responsible for fine structure in the radiated acoustic energy. The crack propagation modulates the source spectrum; I adapt a concept introduced by Haskell [35] and model the source as a sinusoidally roughened ramp function, thereby including a significant fraction of the energy in a primary or base-band lobe. The frequency of this lobe is governed by the propagation speed and by the coherent length of a crack segment. It thus reflects a key horizontal scale in the ice cracking process. The fine structure, on the other hand, has a frequency determined by the roughness elements in the mechanical failure. The fine structure is much weaker than the base-band signal; for example, in event IV, it has a relative amplitude of only 0.12. while there is an ambiguity in the

interpretation concerning the number of elements associated with propagation of a crack through the ice, I can nevertheless relate the fine structure signal components to the vertical scale of the rupture.

Such a model is consistent with the observations that, for nearby sources, there is a significant variability in the signal between hydrophones, whereas the signal is relatively independent of hydrophone locations for distant sources. The terms *nearby* and *distant* are used in the sense of near field and far field, with respect to the aperture of the array; the important criterion is the relative crack velocity as observed from different parts of the array. In principle, a comprehensive analysis should allow recovery of the full vector properties of the sound source using signals derived from several hydrophones. Inversion of the data along these lines lies beyond the scope of the relatively simple treatment described here, and may, in fact, require a much larger array of hydrophones. Instead, I use the dominant frequency components f_b and f_h, and the pulse duration deduced from the high-frequency signal, to derive essential scales of the cracking process (Table 2.4).

The observation presented here differs significantly from previously reported measurements in the open ice pack (see, for example, Figure 3 of Stein [24]) in that the acoustic signal rises sharply out of a very low background noise level. None of the data presented in this chapter have been further low-pass filtered; the low-pass cutoff is determined by hydrophone response (-6 dB at $32Hz$). Dyer [29] has suggested that low-frequency sources are associated with macroscopic ice motions. Evidently such source mechanisms are not shown in my data either because the low-pass cutoff frequency of the hydrophones used is too high ($32Hz$) to allow observations of this sound or because the low frequency signals were not present at the experimental site.

Chapter 3

The Central Canadian Arctic Ambient Sound Experiment and Radiation Models for Surface Cracking

3.1 Motivation and Description of the Experiment

In the previous chapter, I have examined individual cracking events. Those events do not have strong correlations with the local environmental forcing (see Figure 2.3): their origins might be related to large scale internal stresses that are transmitted through the rigid ice pack. Moreover, lacking information of local ice conditions makes it impossible to study the sound generation mechanisms in terms of ice type. Our understanding of sea ice response to stress would be deepened if a more comprehensive data set including ice conditions is collected.

Tensile stress induced by thermal effects is the most common force that causes surface fracturing in an ice sheet during the Arctic spring. Thermal cracking pro-

cesses lead to the release of surface tension and consequent generation of acoustical radiation into the water from the ice over a large ice field. An ice field subjected to neither strong wind nor water currents but to dropping air temperature $(< -20C)$ is desirable for the study of thermal cracking sound.

As part of a continuing program aimed at resolving sound generation mechanisms in sea ice, a second ambient sound experiment was conducted in the spring of 1988 near the west end of Barrow Strait. Figure 3.1 shows the site.
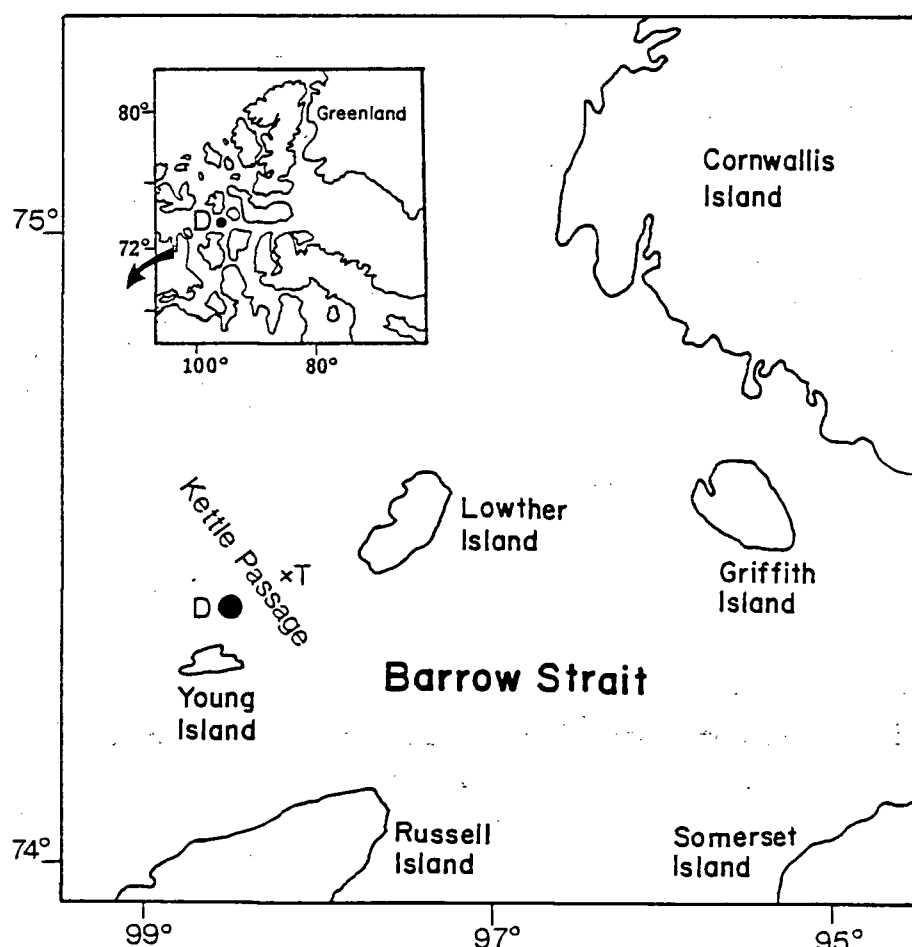
Figure 3.1: Site of the 1988 Ambient Sound Experiment. Also shown in the chart are the instrument deployment site D and current measurement site T.
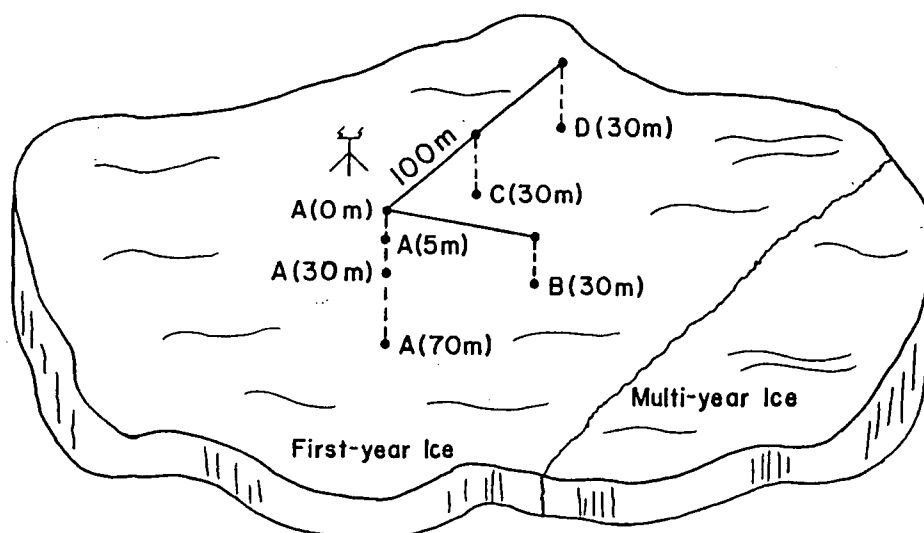
Figure 3.2: Deployment configuration of 7 hydrophones used in 1988 experiment. B, A_{30}, C, D form approximately a right angled triangle at 30 metres depth with $100m$ spacing between adjacent hydrophones.

The instrumentation used in this experiment is similar to that used in the 1987 Beaufort Sea experiment. However, on this occasion a 7-hydrophone system was deployed to record the ambient sound field as shown in Figure 3.2. One of the hydrophones(A_0) was placed in a hole drilled into the ice, which was filled with anti-freeze fluid. The site was selected because of its location near the boundary of two quite distinct ice fields: first year ice of about 1.75 m thickness, and multi-year ice (see the air photograph in Figure 3.3). The experiment lasted about 8 days during which excellent data sets were recorded, including ambient sound generated by the effects of wind, current, air temperature changes and also marine mammals.

In this chapter, I will focus on events occurring when the air temperature was decreasing sharply (down to $-20C$). These events might not be caused exclusively by thermal stress. However, the close correlation between the cooling and sound spectral level, strongly suggests a thermal stress origin and I refer to the signals hereafter as thermal cracking events.
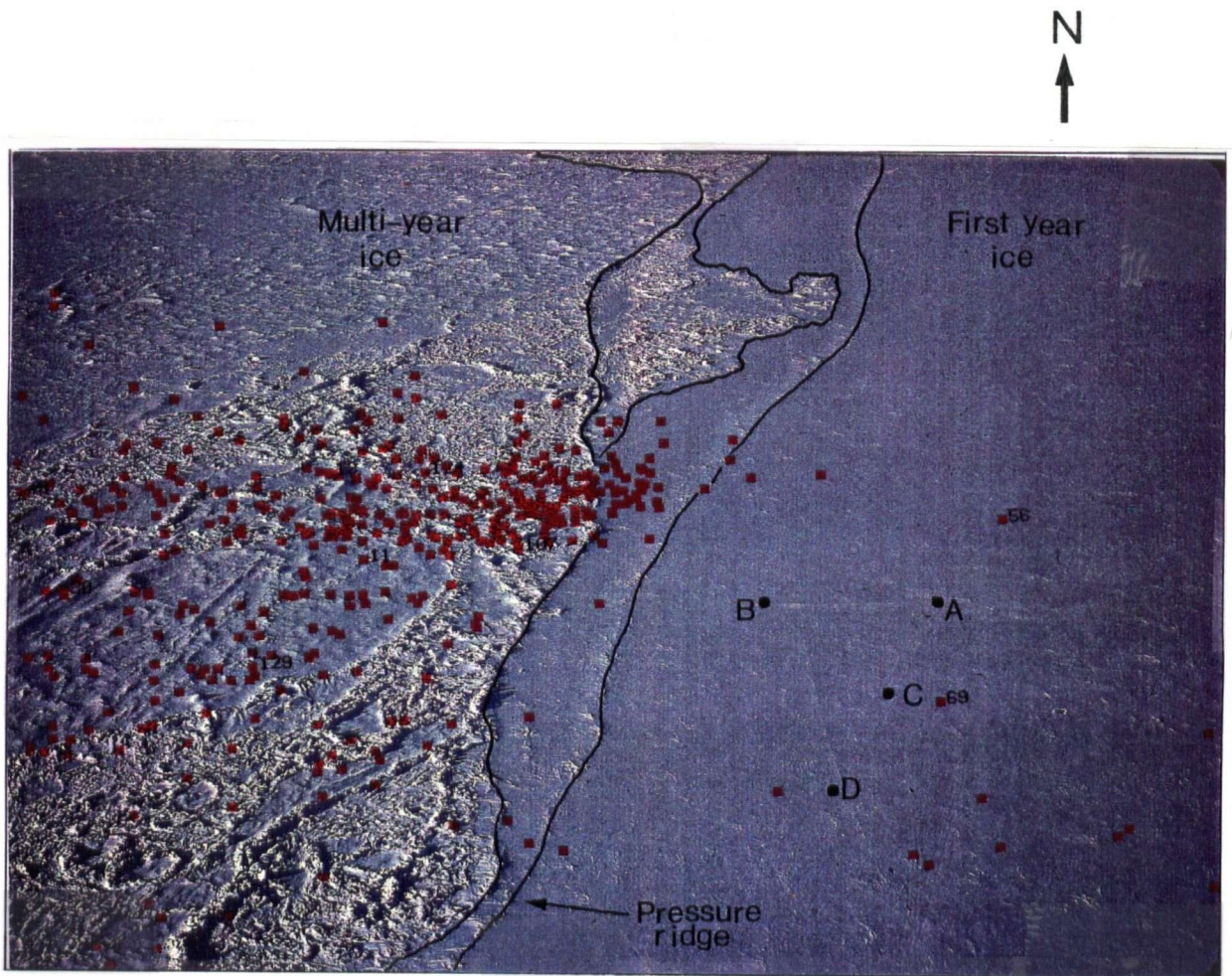
Figure 3.3: An air photograph showing near-field ice conditions with A, B, C, D indicating the 4 deployment locations for the 7 hydrophones. Plotted in red is an ice cracking source map showing about 400 events the locations of which are represented by red dots. The photograph covers an area of approximately $540m \times 1439m$.

3.2 Measurement Approach

With the array system shown in Figure 3.2, ambient sound was recorded with 7 hydrophones for 5.5 minutes every half hour. All the electronic instruments were housed in a thermally insulated and thermostatically controlled housing, installed on the ice surface (see Figure 3.4). Approximately 35 hours of data were collected over an 8 day period. Table 3.1 summarises the entire experiment. Only 6 hours of Section A data are analysed here.

Deployment periods(UTC) (3 Sections)	Sec.A : 04/18/88 22:00:00 to 04/21/88 03:05:00
	Sec.B : 04/22/88 04:04:30 to 04/23/88 16:05:30
	Sec.C : 04/23/88 23:00:00 to 04/25/88 22:00:00
Site	$74°23.5'N; 98°39.3'W$
Hydrophone Type	MetOcean NH4123; Bandwidth: $32Hz$ to $\geq 25kHz$
Data recording (7 hydrophones)	A_0, A_5, A_{30}, A_{70}: 16 bit, $44.1kHz$ PCM-VCR
	B, C, D: $20kHz$ BW, analog VCR channels
Anemometer, Air temperature	Aanderaa, 5.5 minute recording every 30 minutes

Table 3.1: Instrument deployment details.

Acoustic data were stored in two forms on two video cassette recorders. Signals from hydrophones B, C, and D (see Figure 3.2), were recorded as analog data. Although exact sound pressure levels cannot be recovered from these analog channels due to the use of automatic gain control, they are nevertheless suitable for precise determination of arrival time. Signals from the 4 hydrophones in the vertical component of the array (A_0, A_5, A_{30} and A_{70}) were digitally processed using a pulse code modulator (PCM) for storage on the video channels with a sampling frequency of
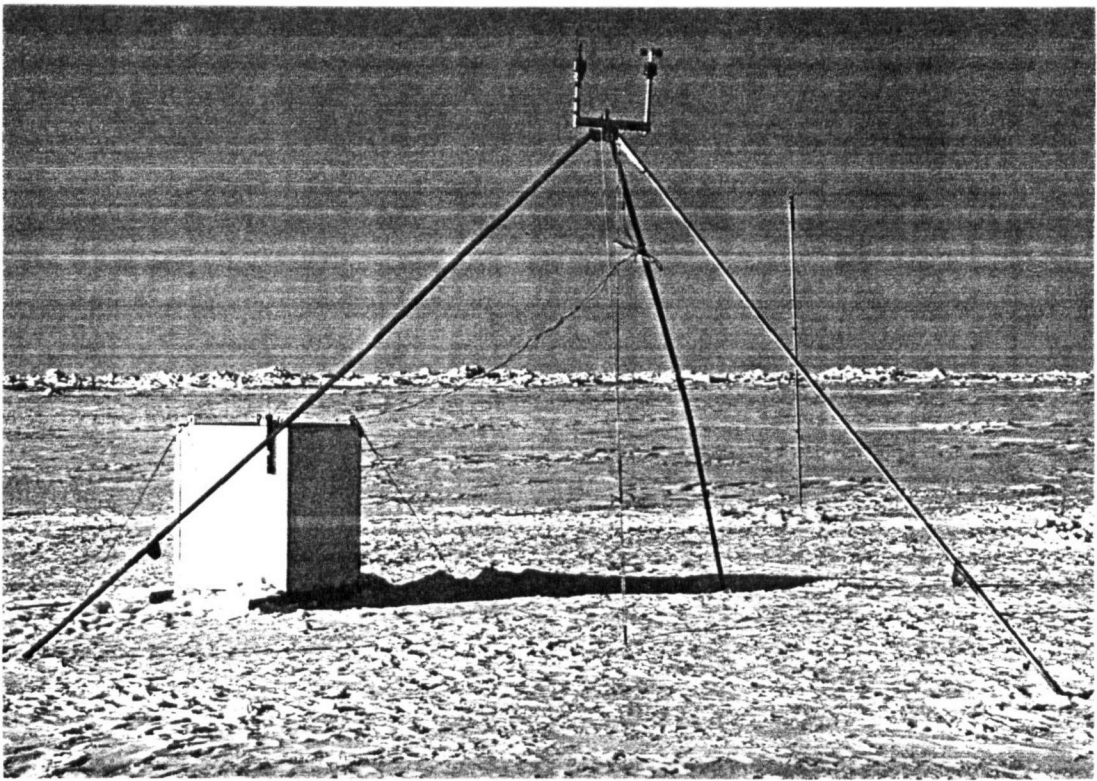
Figure 3.4: Photograph showing instrument housing and weather station. Rubble ice in the multi-year ice field can be seen on the horizon.

44.1 kHz and a dynamic range of $90dB$. These signals are suitable for detailed analysis.

A small anemometer was set up at the site to record wind speed and direction. A temperature sensor was installed on the instrumentation housing to provide a record of the air temperature. These data were digitally recorded on the VCR analog channels.

Three conductivity-temperature-depth (CTD) casts were obtained for each of the three experimental periods; sound speed profiles were calculated for each. A typical profile is shown in Figure 3.5 indicating an upwardly refractive acoustic environment with a sound speed gradient of $+0.055s^{-1}$ providing a best fit.

Ten ice samples were taken to measure the salinity values of the first year ice. The depth of the samples ranges from 0 to $4cm$ from the ice surface. A mean salinity value of 8.5 *ppt* is obtained for the first year ice while the multi-year ice was essentially fresh. As for the accumulated snow in multi-year ice areas, its density
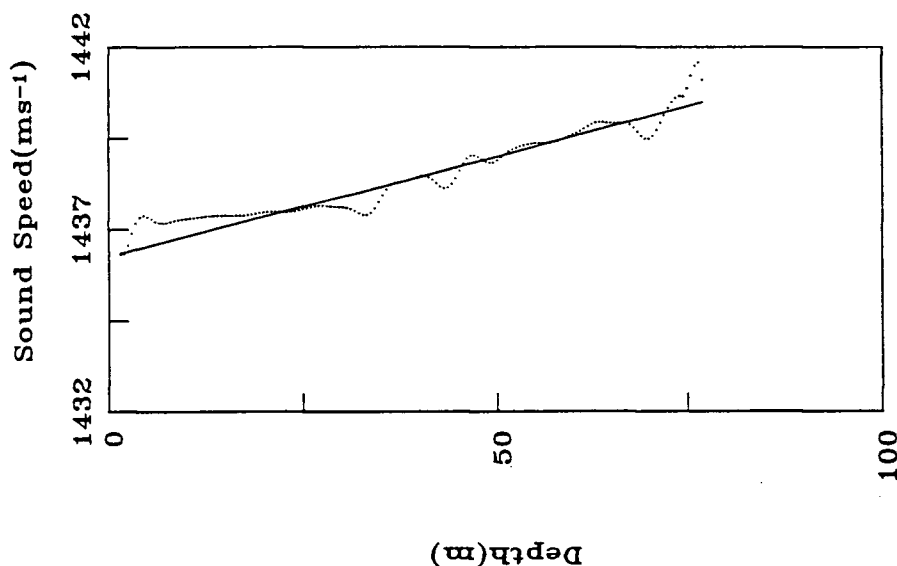
Figure 3.5: Sound speed profile (dotted line) based on *in situ* CTD casts in the water column. The profile is approximated by a uniform sound speed gradient (solid line).

was about $0.35g \cdot cm^{-3}$ whereas snow on the first year ice had a density of $0.1g \cdot cm^{-3}$.

On flat surfaces of new ice, the snow was well packed and about $10cm$ thick. However, in areas of multi-year ice the snow depth was very variable, with numerous exposed ice surfaces (see Figure 3.6).

Echo sounder measurements at locations A, B and D (Figure 3.2), reveal a nearly uniform depth of 110 meters. This flat and shallow sea floor is responsible for reflections of sound radiated from the ice sheet.

I do not have *in situ* current measurements for this experimental site. However, my observations were obtained in Kettle Passage, close to the site of previous measurements (see Figure 3.1) acquired in the 1978 tidal current survey in the Eastern Viscount Melville Sound [38]. Harmonic constituents calculated from these historical records, which were dominated by the semi-diurnal tide, were used to calculate predicted tidal currents at the same location for the period of our observations by the method described by Foreman [39] (courtesy of A. Douglas, Tides and Currents
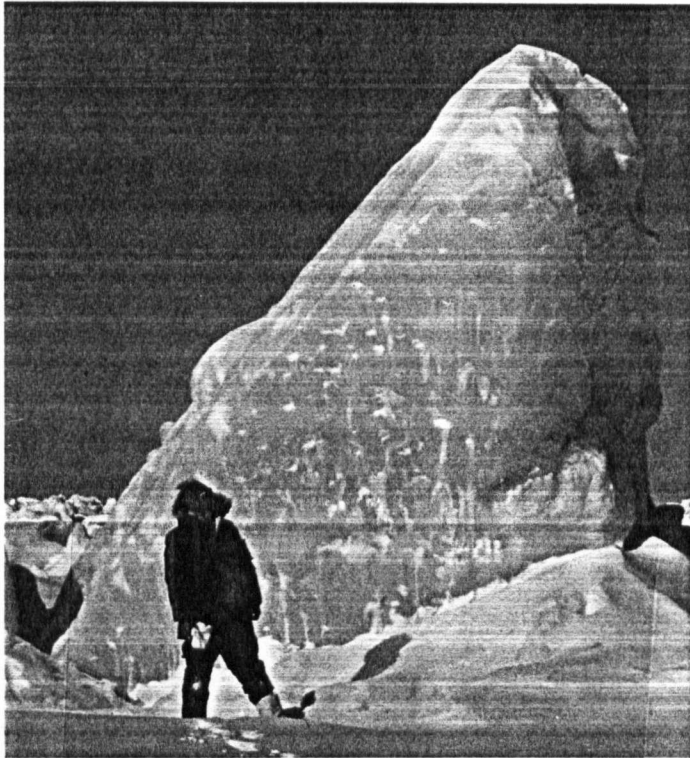
Figure 3.6: Photograph showing a piece of rubble ice in the multi-year ice area. Note snow free vertical surface.

Survey Group, the Institute of Ocean Sciences). The resulting tidal current prediction is shown in Figure 3.7, along with meteorological data and sound pressure levels. In addition to acoustical, oceanographic and meterological data, I also obtained an excellent synthetic aperture radar (SAR) image of the area from the Ice Centre of Environment Canada. Although the SAR image was obtained on February 19, 1988, comparison with air photographs taken at the time of my experiment shows no observable changes in this fast ice environment. The SAR image therefore provides a useful map of the distribution of different ice types.

One of the air photographs (see Figure 3.3) has been digitized and transformed into a rectified plan view image (not shown here). The near field transformation matrix for this image was obtained through the known geometry of the hydrophone array, which can be seen in the photograph, while the far field distortion due to nonlinear transformation of the camera lens is numerically corrected through comparison between the air photo and corresponding SAR image (Figure 3.8). Thus
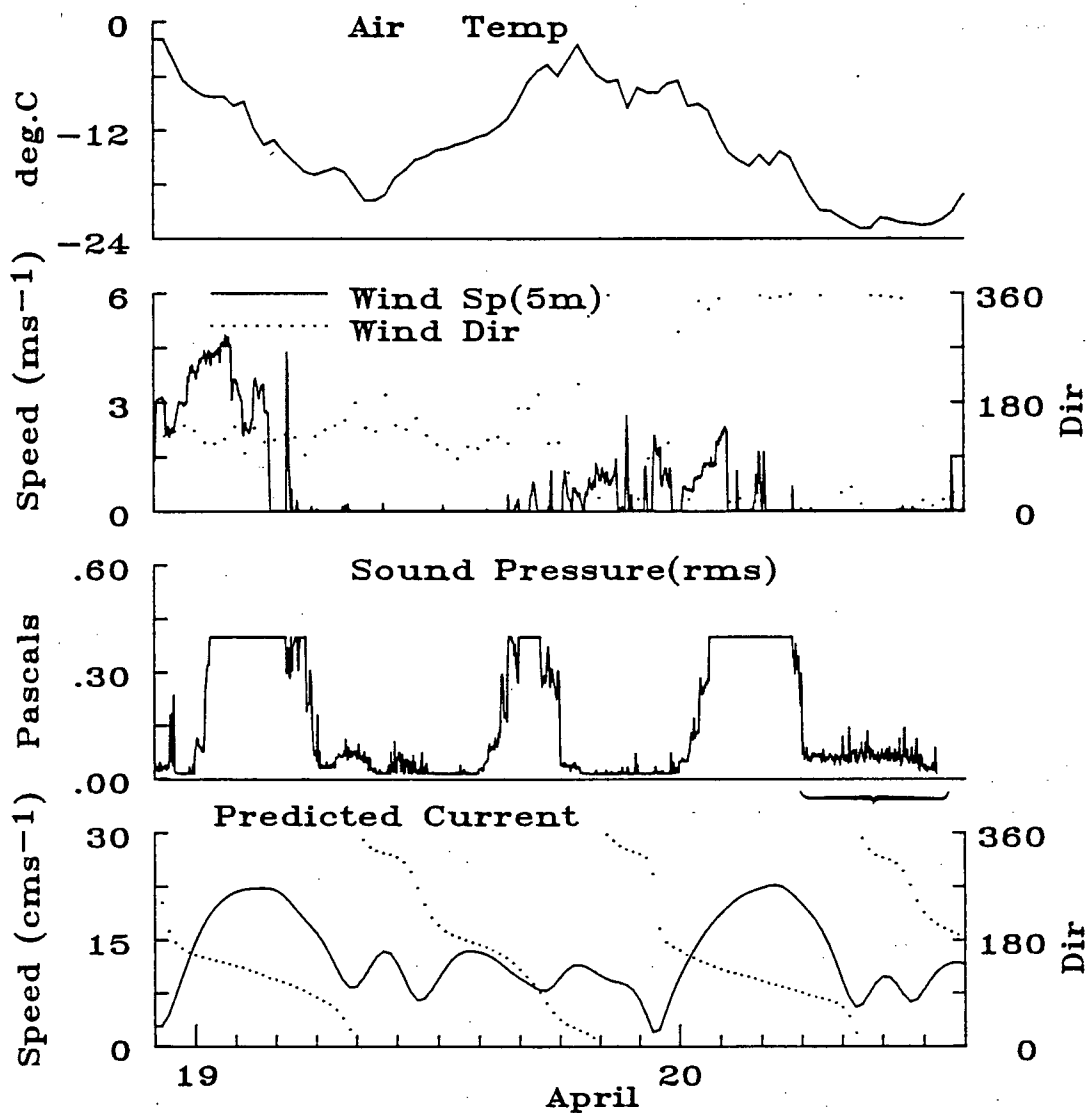
Figure 3.7: Time series records of air temperature(5m), wind speed and direction(5m), underwater sound level (rms) and predicted current speed and direction.

I can reference both air photograph and SAR image to a common rectangular coordinate system, and the source locations obtained through acoustical analysis can be represented on both the air photo and radar image.
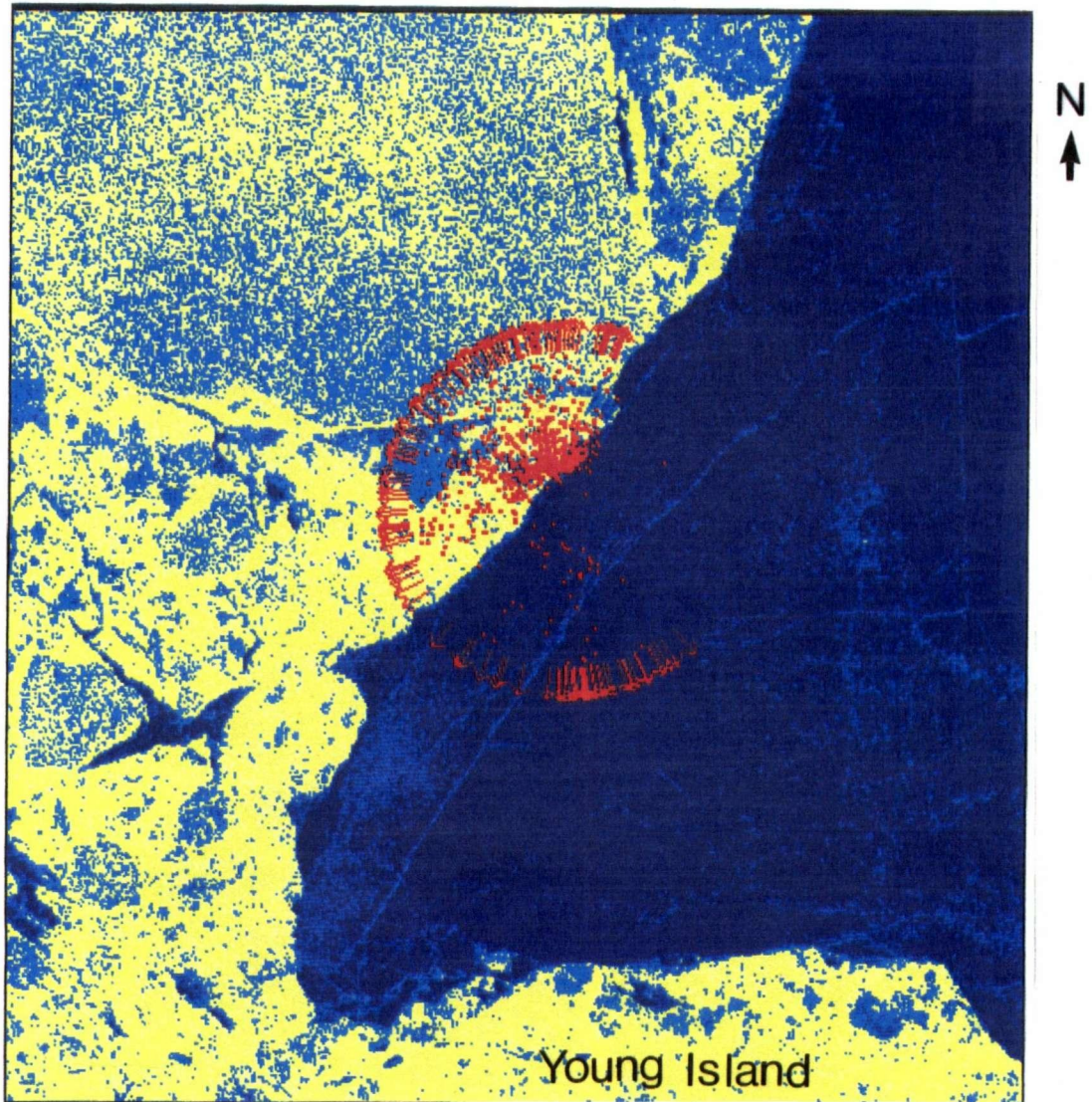
Figure 3.8: SAR image showing the site with blue and yellow indicating snow covered 1st year ice, and rough multi-year ice respectively, and red dots indicating locations of ~ 1000 cracking sound sources; arrows pointing at sources with ranges $> 1km$. The image covers an area of $6000m \times 6500m$.

3.3 Results

Wind, air temperature, predicted current and the root mean square (RMS) of underwater ambient sound level for the first two days of the experiment are shown in Figure 3.7. The two troughs in the temperature curve indicate a diurnal variation which is associated with greatly increased acoustical emissions as shown by many small spikes in the corresponding parts of the sound level curve.

The calculation of acoustical variability (in terms of RMS) is carried out in the same fashion as in the previous study (see Chapter 2). It should be emphasized again that the acoustical record is based not on continuous data, but on $5.5min$ sampling segments once every 30 minutes. Systematic, low frequency signals ($10 \sim 15Hz$) appear in the acoustical data whenever the predicted tidal current exceeds about $15cm \cdot s^{-1}$, and occasionally at other times (see Figure 3.7). These signals may be due to strumming of the hydrophone cables.

Cable strumming is a common phenomenon in underwater engineering. The physics responsible for this phenomenon is the so-called *Strouhal effect*. According to Tritton [40], a sequence of flow patterns occur in a cylinder wake when the Reynolds number (Re) is in the range of $10 \sim 200$. Within this range, a coherent but unsteady flow field will be established behind the cable and cause it to vibrate. The vibration frequency is linearly dependent on the flow speed or the current through the *Strouhal number*. Noise due to cable strumming is usually within the frequency band of $1 \sim 10$ Hz. Since the frequencies of natural cracking sound are beyond $100Hz$, it is not hard to separate the strumming noise from ice cracking sound using spectral analysis. However, if the strumming noise is so strong that it saturates the recording system, then the useful analysis during these periods will be precluded.

Similar noise can also be generated due to the interaction between strong wind and the frame of the nearby weather station (see Figure 3.4).

Since I have plenty of data to work with, I can avoid using those data sets that

have been heavily contaminated. The statistical overall view of ambient sound level shown in Figure 3.7 proves very helpful in determining which data sets should be chosen for detailed analysis. The data selected for analysis, identified by the bracket below the sound pressure plot in Figure 3.7, is free of both wind and current effects. Audio playback of the tape for this period revealed clean ice-cracking sounds with no detectable strumming noise or other contamination. It can be seen from Figure 3.7 that there are many cracking events occurring during this $6hour$ period (indicated by many small spikes), and the only environmental effect is due to the decrease of air temperature (down to $\sim -24^{\circ}C$), which induces thermal tension on the ice surfaces exposed to air. The data are very clean with a high signal to noise ratio. I estimate audible cracks happen at a rate of $> 1sec^{-1}$ for some very intense cracking periods.

A simple peak-detection routine is used to identify events on channel A_{30} for a given threshold ($40 \sim 50dB$ re background noise). An example of some typical events extracted by this routine is shown in Figure 3.9. In principle, with the array geometry formed by hydrophones A_{30}, B, C, and D, the source location can be found from three sets of hyperbolic equations. However, it became apparent during data processing that the hyperbolic system is extremely sensitive to errors in time delay estimates, especially for far field events. In order to overcome this difficulty, reflected signals from the sea floor are used to obtain a better range estimate for the source; this information is then used with data from the horizontal array to determine the azimuthal angle. For those events not exhibiting a strong sea floor reflected component, a graphic method was used to find the roots of the three hyperbolic equations for three given delays of direct path signals using hydrophones A_{30}, B, C and D. This approach is justified based on the following facts:

1. during the 6 hour cooling period most cracking events occurred on multi-year ice; fewer events occurred on first year ice;

2. multi-year ice events often showed strong sea floor reflected signals but noisy background, which tends to guarantee better time delay estimates between
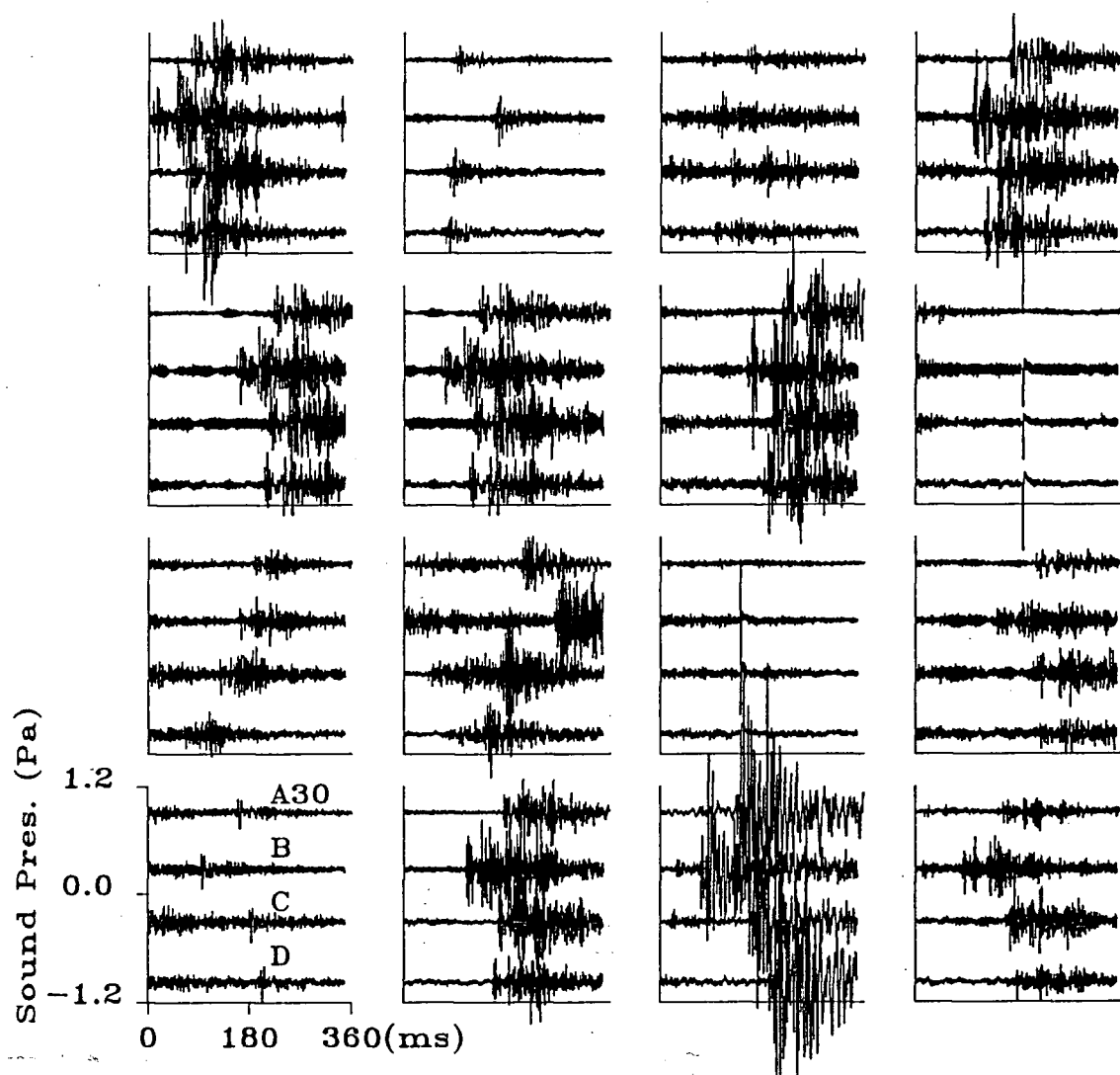
Figure 3.9: Selected events found using an event searching program.

the direct path and sea floor reflected signals received by one hydrophone but poor time delay estimates between the direct path signals arrived at different hydrophones;

3. first year ice events often showed much sharper leading edges in their direct path signals and the much weaker sea floor reflections (explained later), which leads to an opposite tendency of inaccuracy in time delay estimates in contrast to the multi-year ice case.

Only direct path signals are used in azimuth determinations of source location. For this purpose, cross-correlation analysis of the leading portion of the signal detected at each hydrophone is used to extract the arrival time relative to A_{30}. I have ignored the effect of refraction on range estimation. A ray tracing routine shows that for those sources located within $1 km$ distance from the array center, a maximum relative error of 5% in range estimate will occur if refraction is ignored.

Approximately 1000 thermal stress cracking events are processed in this way from the 6 hour period identified in Figure 3.7. Their $2 - D$ spatial distribution is shown in the synthetic aperture radar image in Figure 3.8, and air photo in Figure 3.3. The distribution present on Figure 3.3 is not random, and reveals a close relationship to ice type. Most events during this period occur on multi-year ice, especially rough areas where the ice was free from snow and thus exposed to the effects of rapid cooling. It seems likely that many of these events were caused by thermal stress at exposed ice faces. Second, there are a few cracks near the weak first year ice ridge. These events may be related to the ridge building force and I will examine one of them at the end of this chapter.

Turning next to the same source distribution on a smaller scale (Figure 3.8), it is again apparent that most of the cracks occur on multi-year ice. In this figure, the direction of origin of acoustical sources too distant ($> 1 km$) for accurate range determination is shown by arrows. It is seen that these events are limited to the sector that includes nearby multi-year ice while no far field events occur in the

azimuthal sector facing the first year ice area which extends for about $25km$ before encountering Lowther island as is clearly shown on a even smaller scale SAR image in Figure 3.10. This result implies that either the cracks occurring on first year ice radiate relatively weaker sound or the cooling effect cannot penetrate the snow layer to induce a tensile stress at the ice surface that fractures the ice. It seems to me that the second mechanism is responsible for the distribution shown in Figure 3.10.

Very few cracks occur on first-year ice; the few that do, exhibit somewhat different acoustic features in terms of their radiation pattern and pulse lengths which are discussed below. As an example, records of the sound pressure time series for far field event 104 and near field event $n3$ originating in first year ice are shown in Figure 3.11(a) and (o).
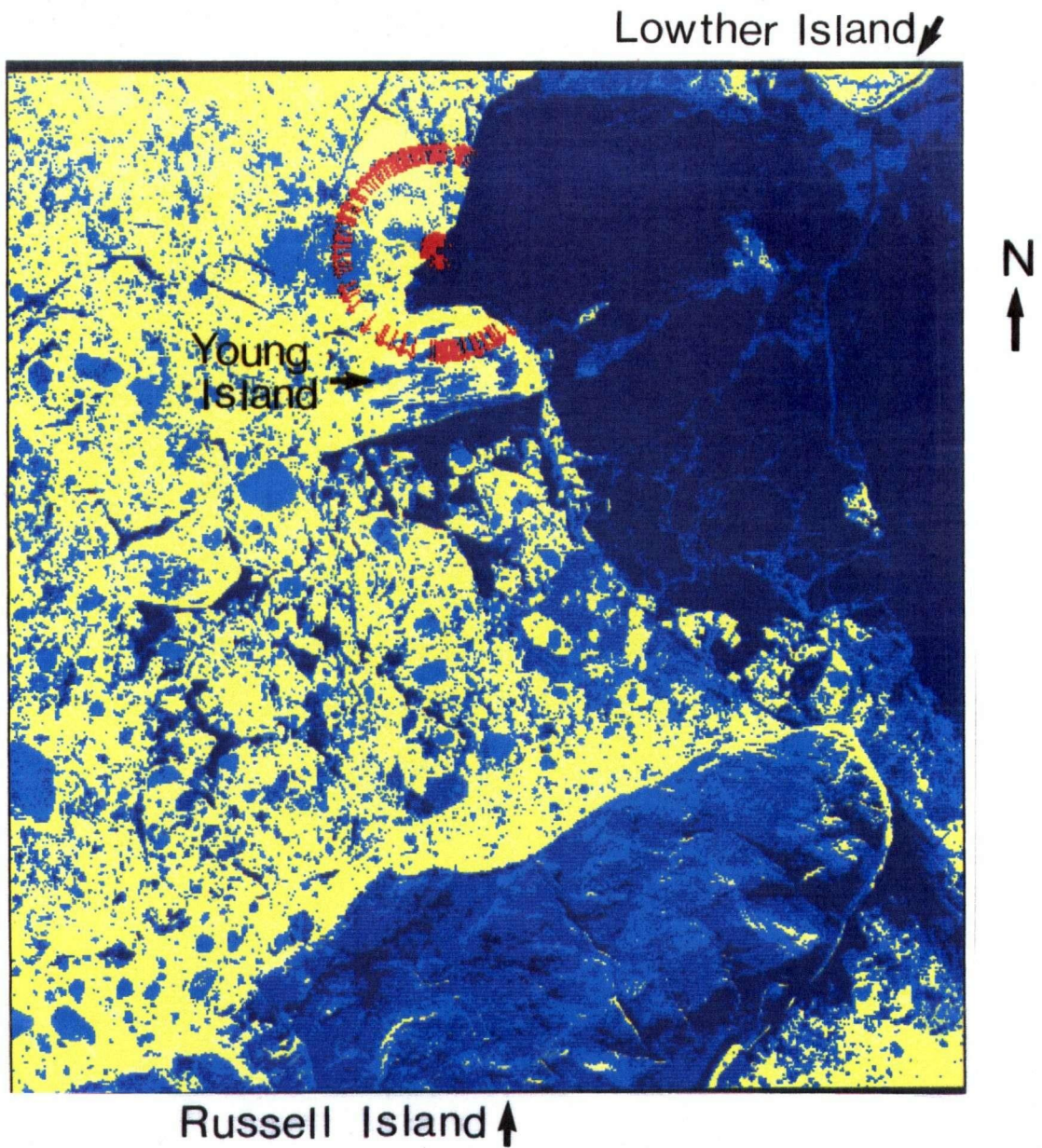
Figure 3.10: SAR image showing the directional distribution of thermal cracking events (indicated by arrows) over a $62km \times 62km$ ice field. Also shown in the image are Young Island, part of Lowther Island and Russell Island.
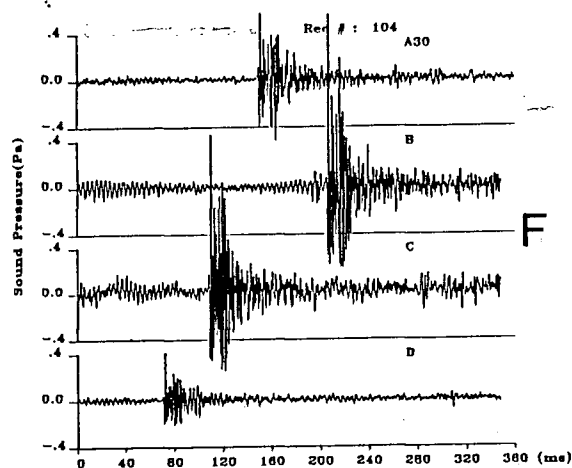
(a) Range $\simeq 1000m$
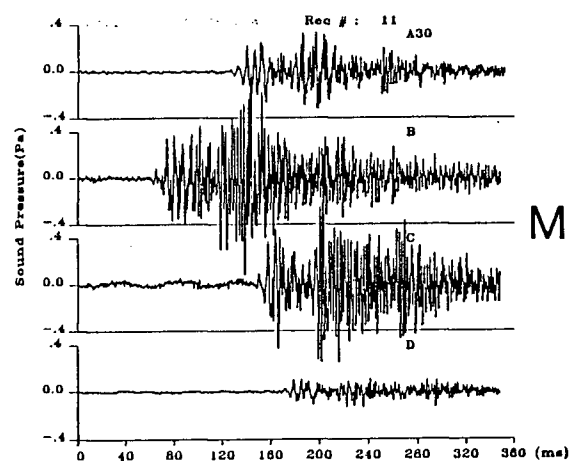
(b) Range $\simeq 325m$.
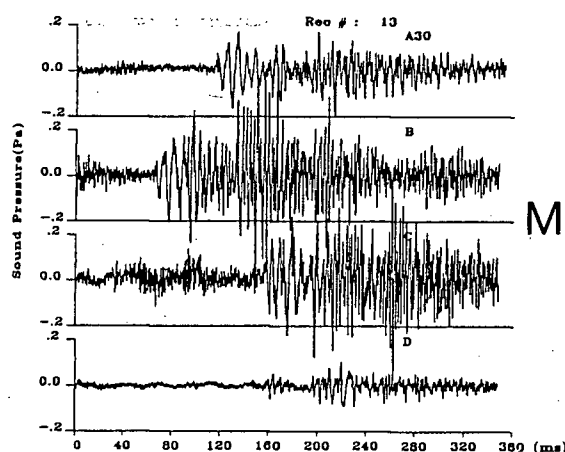
(c) Range $\simeq 417m$
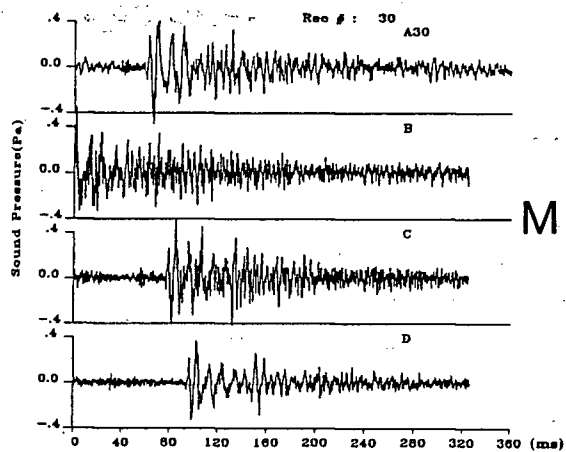
(d) Range $\simeq 312m$.

Figure 3.11: Sound pressure time series recorded by the 4 horizontally spaced hydrophones for 16 cracking events (a)104, (b) 11, (c) 13, (d) 30, (e) 43, (f) 90, (g) 124, (h) 129, (i) 35, (j) 56, (k) 69, (l) 107, (m) n1, (n) n2, (o) n3, (p) n4. F and M denote events occurring in first year and multi-year ice respectively.

This page is for events e, f, g, h.
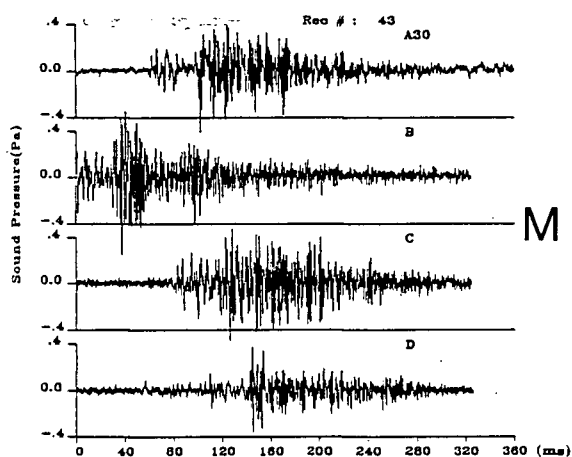
(e)　Range $\simeq 513m$
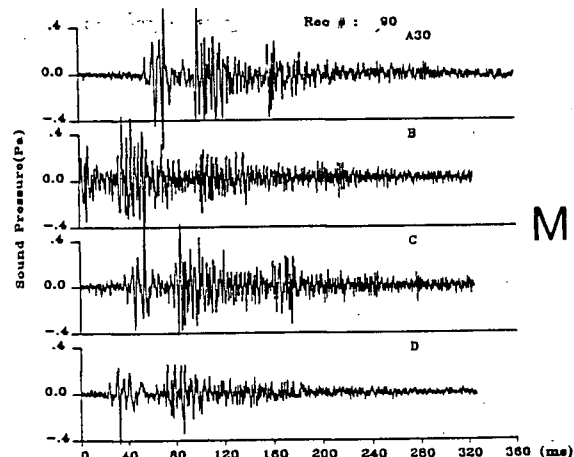
(f)　Range $\simeq 374m.$
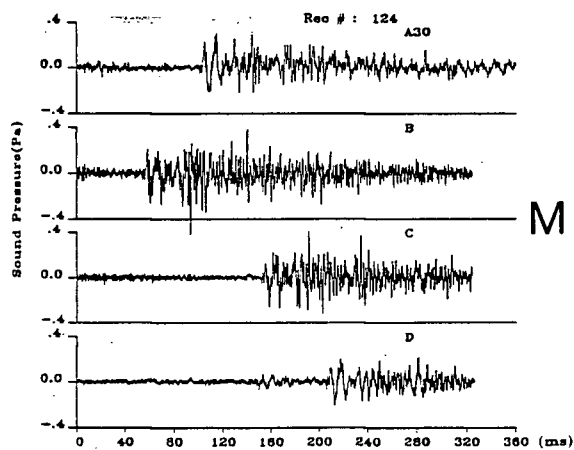
(g)　Range $\simeq 386m$
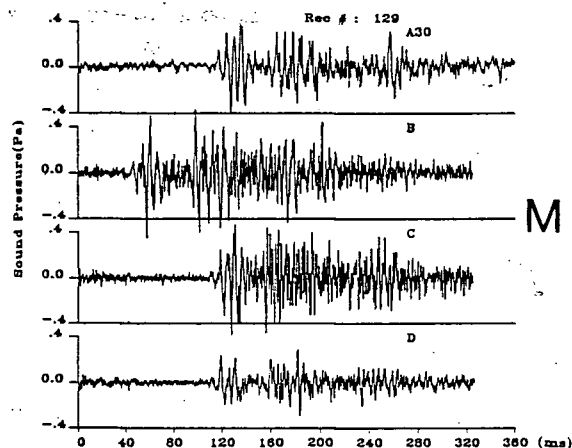
(h)　Range $\simeq 375m.$

This page is for events i, j, k, l.
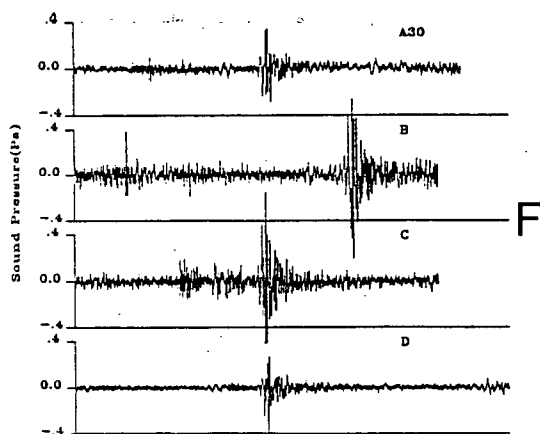
(i)   Range > 1500m
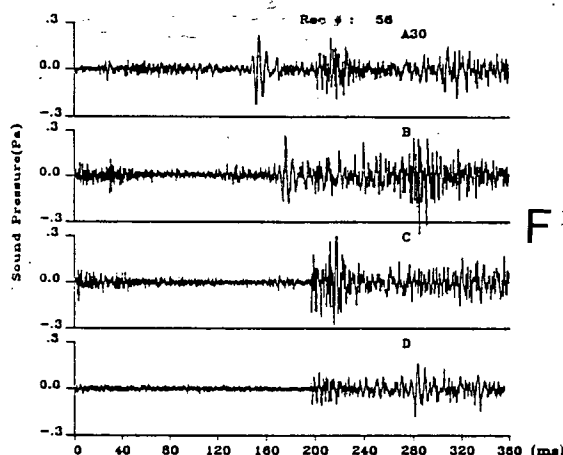
(j)   Range ≃ 150m.
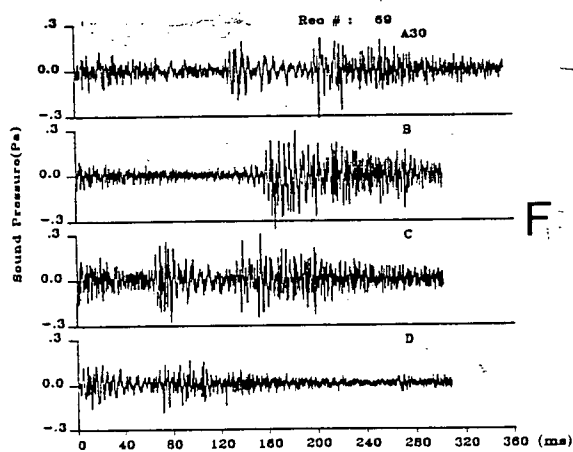
(k)   Range ≃ 120m
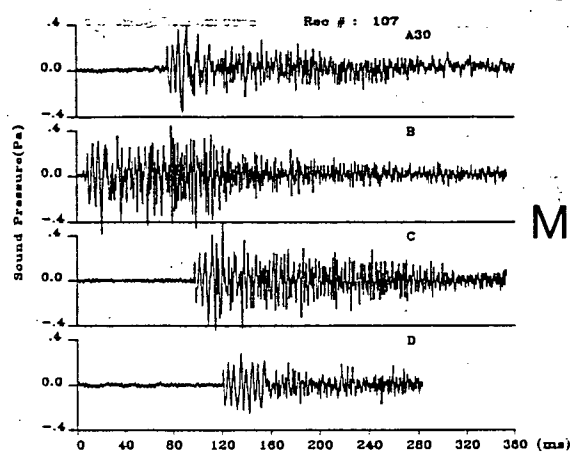
(l)   Range ≃ 226m.

This page is for events m, n, o, p.
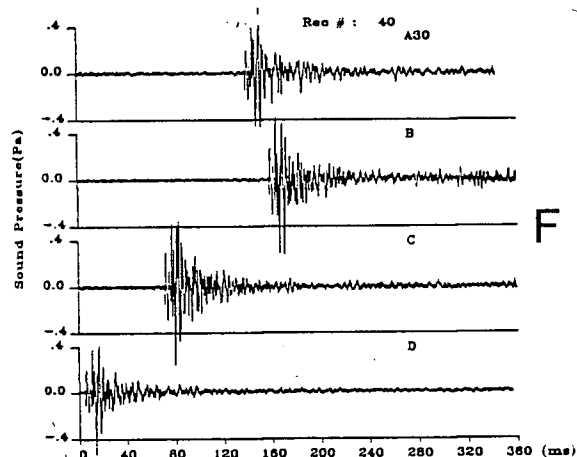
(m)   Range $\simeq 1000m$
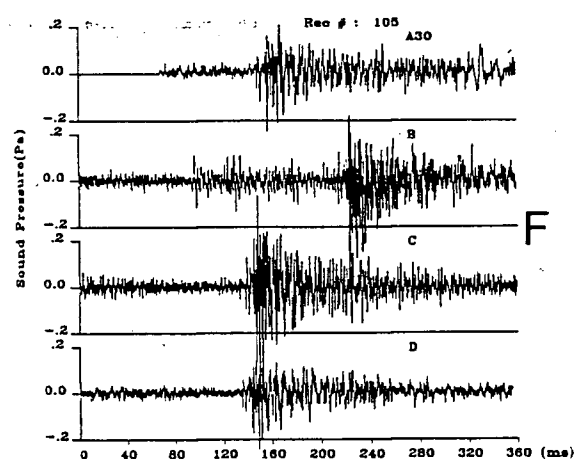
(n)   Range $\simeq 500m$.
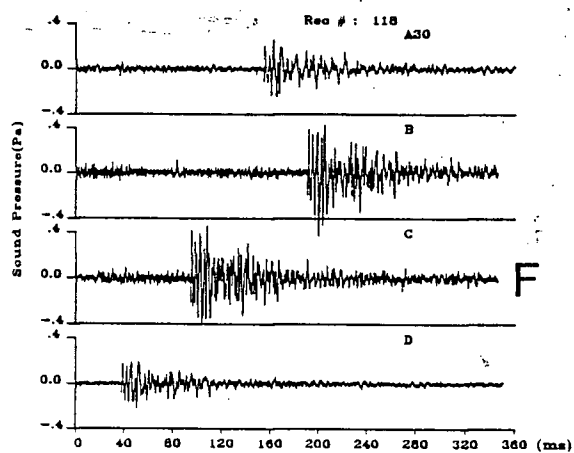
(o)   Range $\simeq 200m$
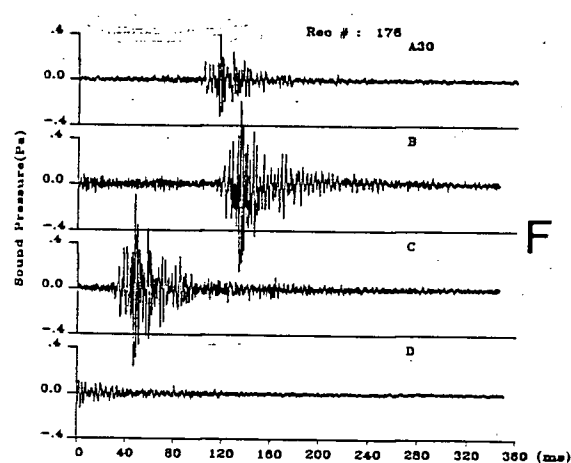
(p)   Range $\simeq 1000m$.

Here I focus primarily on events originating in the multi-year ice, a few of which are analyzed in detail. Figure 3.11(b) to (h) show seven examples. These bear some similarity to cracking events analyzed in the previous chapter (see Figures 2.5, 2.6, 2.7 and 2.8). In some events, for example, event 11, the direct path signal possesses a high frequency component ($> 1kHz$) superimposed on the baseband signal although the high frequency component in this case is not as strong as that in event 4 observed in the 1987 experiment (see Figure 2.8). This latter effect has been interpreted in the previous chapter in terms of a fine scale process involved in the ice rupture. However an unexpected result in the present data, which provides motivation for the subsequent analysis, is that the reflected signal possesses higher frequency components than the direct path signal. This result is more apparent in Figure 3.12 where the signal has been transformed into frequency space using the maximum entropy method. The direct path signal has a frequency range of $100 \sim 300Hz$ while the reflected signal is centered at approximately $400 \sim 600Hz$. Analysis of the underlying physics should lead to deeper insight on the nature of this type of ice failure mechanism and its contribution to ambient sound in the Arctic Ocean.
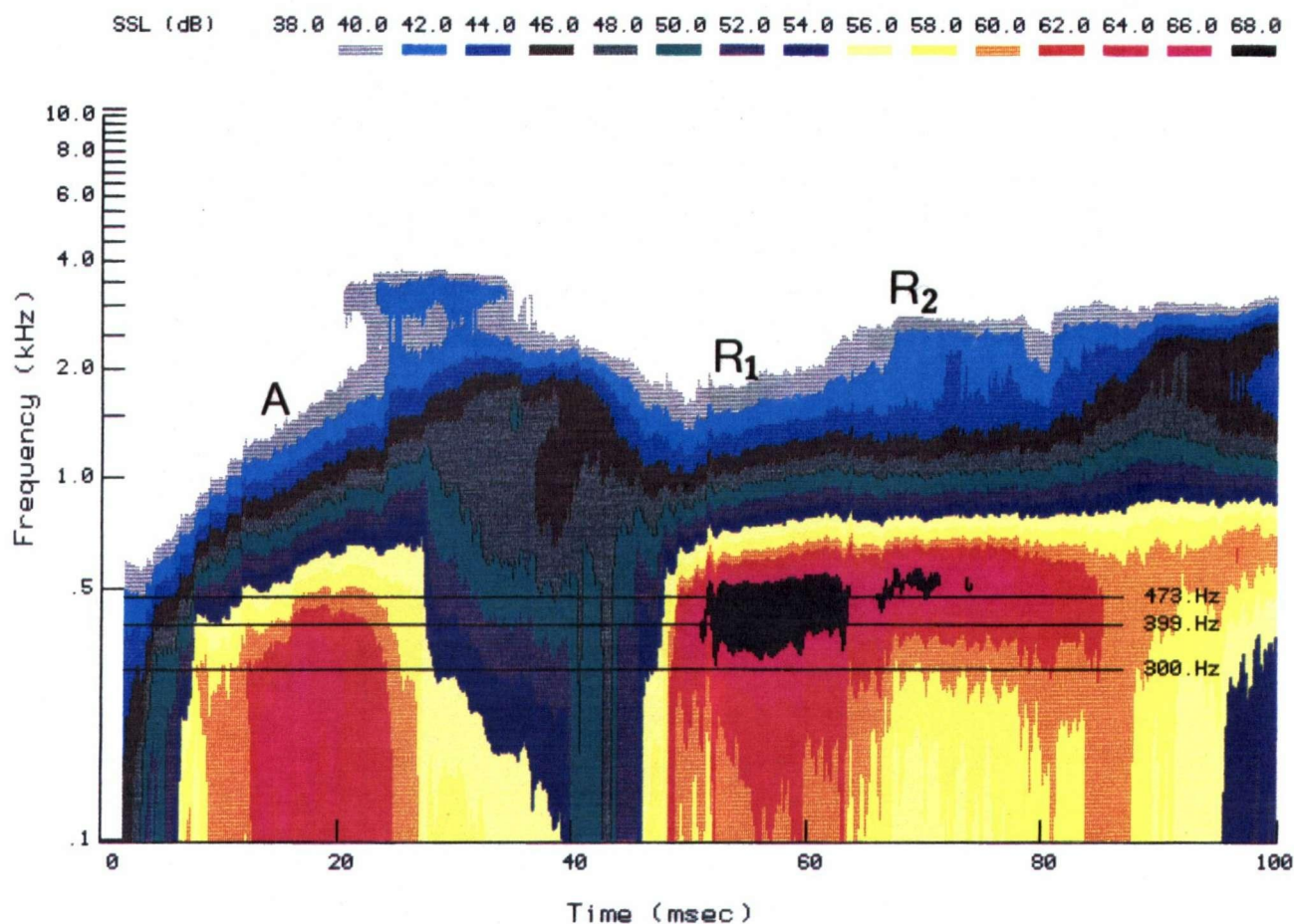
Figure 3.12: Spectral intensity (colours) as a function of time for event 11 detected at hydrophone C. Horizontal lines represent 3 predicted dominant frequencies for the direct path A (300Hz), the sea floor reflected path R_1 (399Hz) and the sea floor-ice double reflected path R_2 (473Hz) respectively.

3.4 Radiation Mechanisms

Arctic acoustics is appropriately treated as a linear problem Press and Ewing [22], Ewing *et al* [33]. Therefore, the sound field beneath sea ice is a result of interaction between natural cracking sources and the ice cover from which they originate. In other words, the sound spectrum beneath ice is the product of the source spectrum and impulse response spectrum of the ice cover. Here the propagation effect of water is ignored. The acoustical features of ice cracking sounds that I have observed motivate me to study the acoustical radiation associated with ice failure in terms of *ice mode radiation* and *water mode radiation*.

By *ice mode radiation*, I mean that energy associated with a cracking sound must travel in a way determined by wave equations and boundary conditions. That is, before radiating energy into the ocean, the cracking sound has travelled for some distance within the ice cover, and experienced the effect of the waveguide formed by air, ice and sea water. This model was first proposed by Press and Ewing in the early 1950s [22]. Although this is an oversimplified, ideal waveguide model, difficulty remains in obtaining a general form of analytical solution which would be valid for all wavelengths. As mentioned in chapter one, only asymptotic solutions can be achieved and these are valid for wavelengths either much less or much greater than the ice thickness. In this case, one can have 5 types of eigenvalues for the horizontal wavenumber (see chapter 1). Despite the simplified nature of this model, it does reveal some essential acoustical properties of an ice cover from the point of view of waveguide propagation. More than three decades later, Stein [23] used a numerical approach to solve Press and Ewing's characteristic equation, and obtained some interesting results. However, Press and Ewing's elegant theory as a prototype model for ice acoustics, has probably been exploited as far as it usefully can be in searching for explanations of Arctic ambient sound.

By *water mode radiation*, I mean that acoustical energy generated by cracking processes radiates into water directly beneath the source region in the ice. Waves
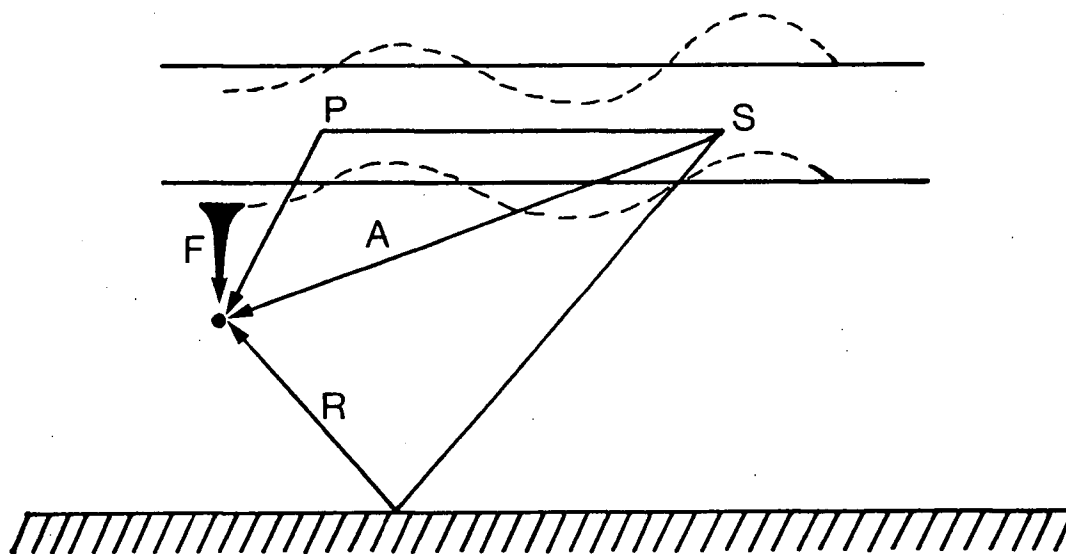
Figure 3.13: Paths showing the arrival of 4 waves at a hydrophone from a hammer blow source.

associated with this kind of energy are not subject to waveguide propagation as they are in the *ice mode* case. Rather, their signatures are determined by the mechanical properties of the local ice within the source region. In this case, the behaviour is better described as a vibration problem than a waveguide problem, and it is the sound matching mechanism or transmission coefficient between ice and water that determines how much energy, and which frequency components are radiated into the water. Direct path (A) and reflected (R) acoustical waves sketched in Figure 3.13 illustrate such a radiation mode.

Observations obtained from both 1987 and 1988 experiments make it clear that most of the ice cracking sound energy detected in water comes from water mode radiation while the contribution from ice mode radiation can be ignored. There are

two pieces of evidence that support this hypothesis. First, the time delays for all the events shown in Figure 3.11 between direct path, sea floor reflection and sea floor–ice bottom reflection signals confirm that primary signals arrive at hydrophones from crack regions through water channels. Second, a broadband ice cracking sound would appear as a signal of low energy and low frequency (probably $< 200Hz$) with a much narrower band in water had it followed a path through the ice cover as its primary signal channel, owing to the higher attenuation and frequency constraints of propagation in the ice cover waveguide. For most of the recorded events, this narrow band low frequency energy is not observed. Therefore, the local vibration of ice at the source is a predominant mechanism for sound radiation from sea ice into the ocean, at least for the observations I describe. I believe that the study of sound coming directly from the source will lead to insight into the source mechanism in terms of seismic movement associated with structural failure in the ice. On the other hand, if the source is broadband, the signals will probably reveal local mechanical properties of an ice cover in terms of its response function. In any case my attention will be focused on the analysis of sound radiation due to water mode propagation.

3.5 Impulse Response of Sea Ice Subject to a Normal Impact

One gains a vivid picture of the acoustical behaviour of sea ice by examining the impulse response of an ice cover experimentally. Here I discuss two cases. In the first case, the impulse source is generated on the first-year ice, close to the hydrophone array. Therefore, signals due to both water mode radiation and ice mode radiation may be detected. In the second case, the source is located on the multi-year ice. The presence of a boundary between the two types of ice serves as a barrier to ice mode radiation so that one can detect water propagation mode radiation only. In both cases, the impulse source is simulated by a normal impact on the ice and results in an expected acoustical dipole radiation pattern beneath the ice cover. The radiation pattern due to a horizontal force will be discussed later.

3.5.1 Acoustical Radiation from First Year Ice

The impulse source in this case was a hammer blow delivered to the ice surface near hydrophone B (Figure 3.2) with an eight pound sledge hammer. An example is shown in Figure 3.14 where time series of sound pressure are shown for each of the 4 vertically spaced hydrophones (saturation occurs for the hydrophone located in the ice A_0). At the $5m$ hydrophone (A_5), one can see a weak precursor of about 140 Hz, identified as P in the figure, arriving first. This is the dilatational or P wave, excited by the blow; it travels at a phase speed of about 2630 $m \cdot s^{-1}$ in the ice and radiates into water at an angle of about $33°$ (with the vertical). Following the P wave is the acoustic wave (identified as A in Figure 3.14) with a frequency of $516 Hz$. This wave arrives directly from the source through the water due to *water mode radiation*. It is weak because of the low radiation gain of the dipole source at this shallow angle with the horizontal. Almost simultaneously, a low frequency pulse arrives. This signal (identified as F) is anomalously dispersive with higher frequency(~ 60 Hz)
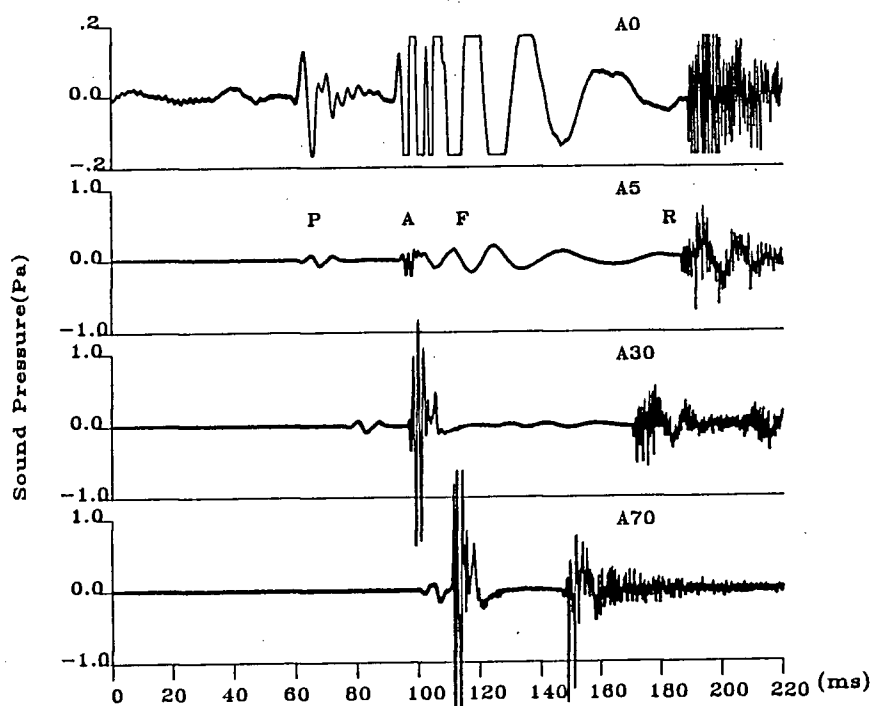
Figure 3.14: Sound pressure time series recorded by the 4 vertically spaced for a hammer blow near B. Letter P stands for P wave; A: direct path acoustic wave; F: flexural wave; R: sea floor reflected wave.

components arriving first, followed by lower frequencies (down to 30 Hz). This is the SV wave, or for very long wavelengths as in this case, a flexural wave, which propagates as an inhomogenous plane wave in water, because its maximum phase speed in ice is less than the sound speed in water. The evanescent property of the flexural wave is apparent from its rapid decay with depth: it is barely detectable at $30m$. Finally, a strong reflected acoustic wave (identified as R) arrives from the sea floor. Figure 3.13 illustrates the paths of each of the four types of waves.

It is immediately apparent that there is a shift in spectral peaks between direct and reflected signals just as is also found in the naturally occurring signals of the twelve events mentioned above (Figure 3.11).

A spectrum of the pressure signal at $5m$ is shown in Figure 3.15 where the spectrum has been prewhitened with a $-14dB$ per $decade$ filter. Here I again emphasize that P and F(flexural) waves are caused by the *ice mode radiation* of
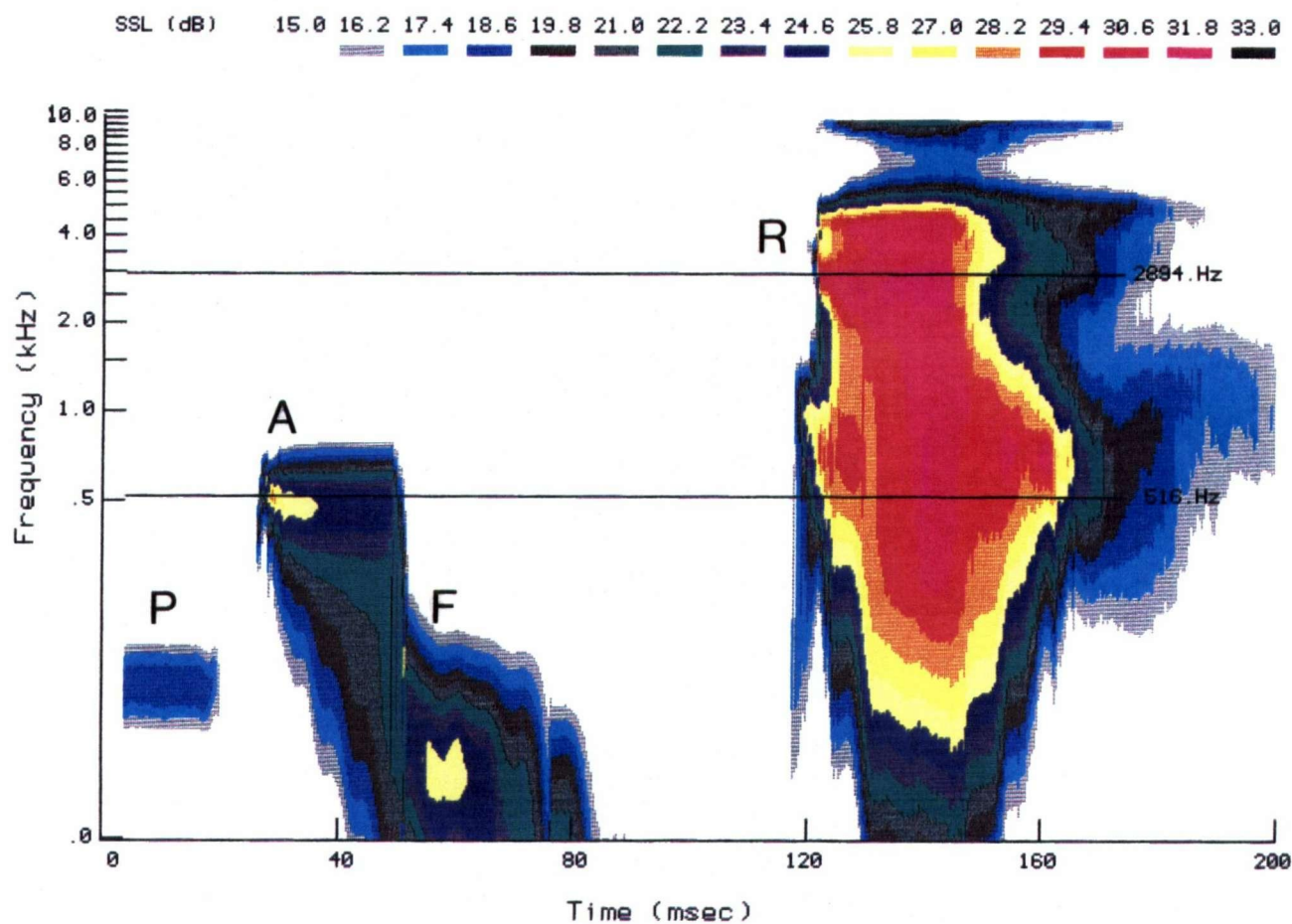
Figure 3.15: Spectral intensity (represented by colours) as a function of time for a hammer blow near B with P: P wave; A: direct path acoustic wave; F: flexural wave; R: sea floor reflected wave. The data are based on record A_5.

the ice cover (i. e. waveguide propagation), while the A (acoustic) and R (reflected) waves radiate into the water from the local ice region at the source.

The experimental analysis of ice response to a hammer blow provides me with an approximate solution to an impulse response of the air-ice-water system. It is interesting that even for a broadband source such as a hammer blow, signals detected by my hydrophones have relatively narrow bandwidths; it appears that the ice cover serves as a filter of multiple pass-bands.

It is clear that the frequencies of spectral peaks associated with the P and F waves are determined by eigenvalues of a waveguide system formed by air (or a vacuum in the model representation), ice and water. Although, Press and Ewing's theory predicted that there could be an infinite number of possible eigenmodes existing in the waveguide, we really see in this example that only two modes are excited. Other modes associated with both symmetric and anti-symmetric forms of solutions may of course exist, but the data imply that in a real environment, the P and F waves we see here are dominant. Since the waveguide character of the ice-water system is well developed in Press and Ewing's theoretical model [22], I will not pursue analysis of the waveguide components due to ice mode radiation. Rather, I will focus on the way in which the frequency of water mode signals corresponding to A and R waves, depends upon the angle of radiation.

3.5.2 Acoustical Radiation from Multi-Year Ice

Two types of impulsive sources were used to study the radiation from multi-year ice: a hammer blow and a small explosive charge placed on the ice surface. The source location was on a small, relatively flat old ice floe about 350 meters away from the array centre along the direction from hydrophone A_0 to B, (see Figure 3.2). Figure 3.16 shows the time series of sound pressure recorded by the 4 vertically spaced hydrophones, where A, R_1 and R_2 indicate direct path, sea-floor reflected and sea-floor and ice-bottom double reflected acoustic waves respectively. An extremely weak
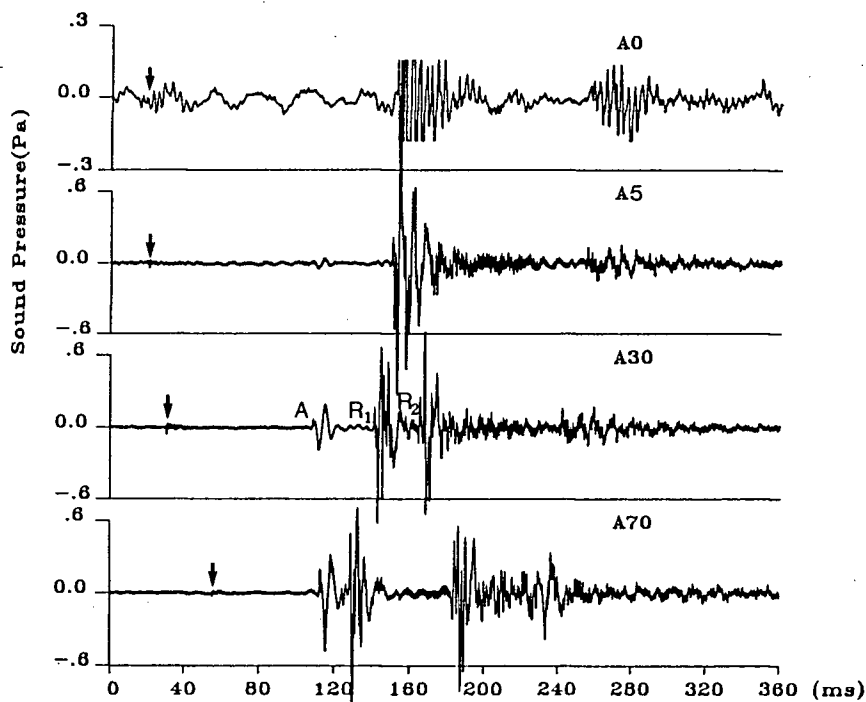
Figure 3.16: Sound pressure time series recorded by the 4 vertically spaced hydrophones for a hammer blow on multi-year ice showing A, R_1 and R_2 waves. Arrows indicate the arrival of a very weak P wave. The A_0 channel has a higher gain, and shows an enhanced background signal due to distant ice cracking events.

signal associated with P wave was barely detected in this case (denoted by arrows in Figure 3.16) while no significant signal associated with flexural wave arrived at the hydrophones. I believe that the existence of the boundary between the first year ice and multi-year floe acts as a barrier to the passage of the P and F waves into the first year ice. Thus the ice mode radiation in this case is greatly weakened or inhibited due to the destruction of the horizontal waveguide properties by the ice ridge or by other irregularities in the ice field nearer the source. Consequently, only water mode radiation contributes to the underwater sound. As in the other examples, there is a shift in spectral peaks between the direct path and sea floor reflected signals; this feature is more clearly seen in the frequency domain (Figure 3.17).

Similar signal structures can be reproduced when the explosive source is used
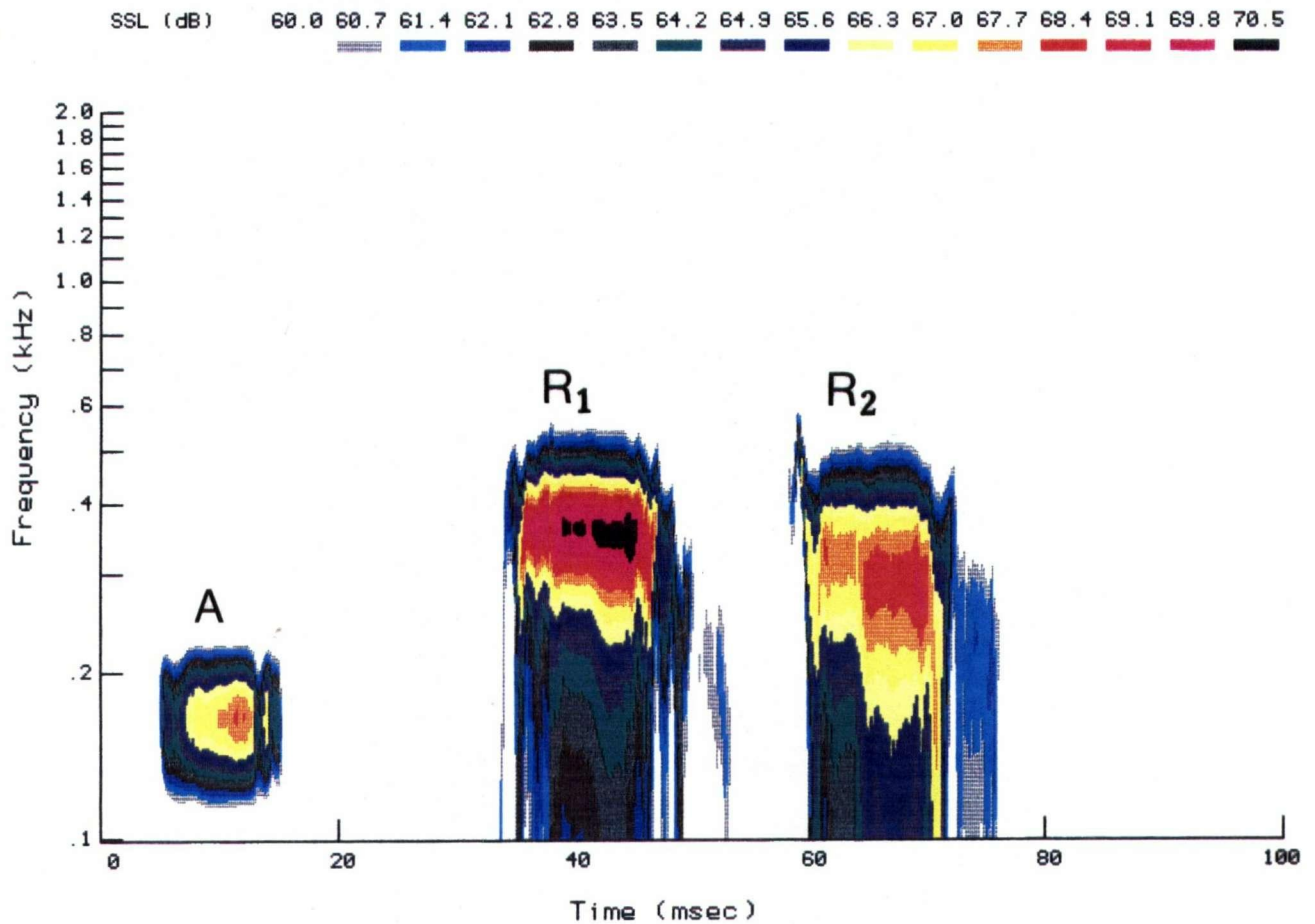
Figure 3.17: Spectral intensity as a function of time for a hammer blow event shown in the previous Figure with A: direct path acoustic wave; R_1: sea floor reflected wave; R_2: sea floor–ice bottom reflected wave. The data are based on the record of the A_{30} hydrophone.
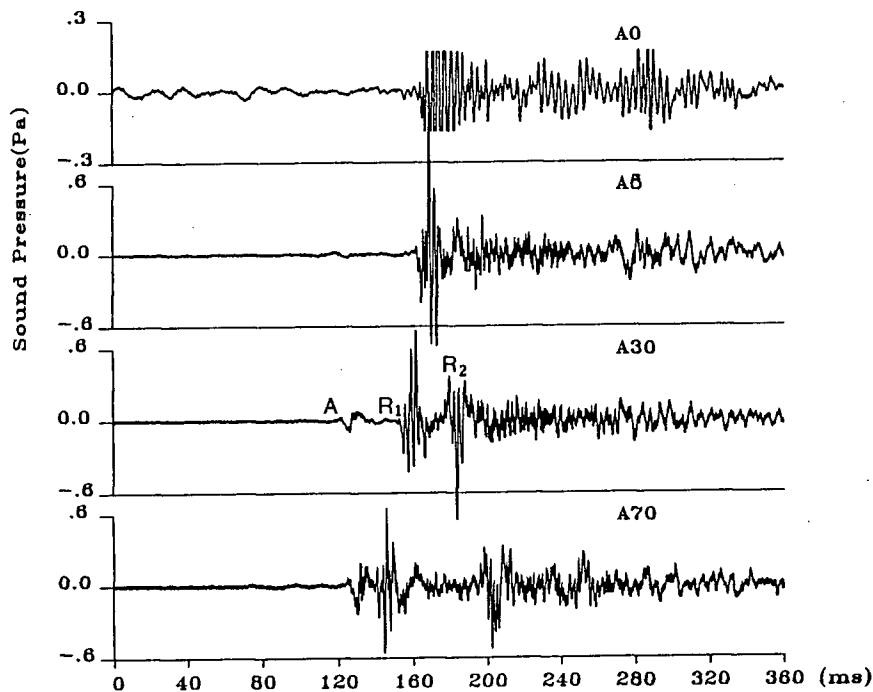
Figure 3.18: Sound pressure time series recorded by the 4 vertically spaced hydrophones for an explosive source on multi-year ice showing A, R_1 and R_2 waves.

(see Figures 3.18 and 3.19). The explosive was placed in a shallow hole, about $10cm$ deep, on the ice surface. However, for this case the direct path acoustic wave is much weaker and the signal has a slightly lower central frequency with a broader bandwidth than for the hammer blow case (see Figure 3.16). As far as reflected signals are concerned, they are quite similar in each case. No P or F waves were observed in this example. These features are clearly shown when comparing Figures 3.17 and 3.19. The dissimilarity between the direct path signals triggered by the hammer blow and explosive may be due to the difference in forcing mechanisms between the hammer blow and explosive. Neverthless the same feature of spectral peak shift between direct path and sea floor reflected signals is apparent.
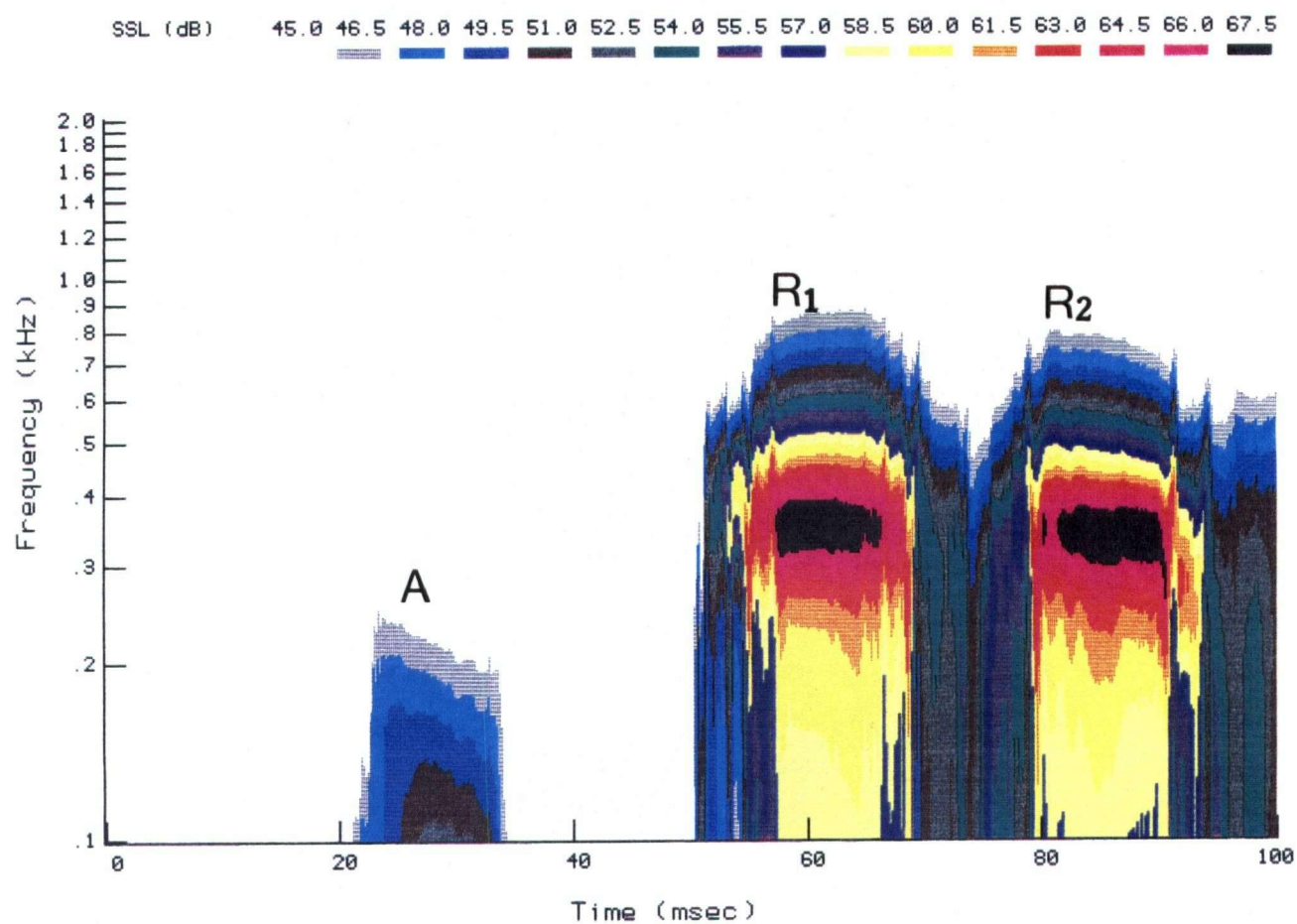
Figure 3.19: Spectral intensity as a function of time for the event shown in the previous Figure. The data are based on the record of the A_{30} hydrophone.

3.6 Theoretical Considerations on Transmission Coefficient of an Elastic Plate and Angular Frequency Dependent Sound Radiation from An Ice Cover

I have shown from the observations of both naturally cracking sound and artificially generated sound that cracks near ice surfaces tend to excite acoustical radiation which results in a relatively narrow band signal in the water, and the dominant frequency of the signal is path- or angle-dependent. In this section, I will examine this observed feature from the point of view of plate vibration theory, and extract some essential physics from a theoretical model. For convenience, I will call this feature *angular frequency dispersion* hereafter.

It is a well known fact that dispersive waves can be excited in an elastic plate bounded by a vacuum. This is true both from a wave propagation point of view (see Ewing and Press [33] pp. 281), and from the view point of plate vibration due to an external forcing or a forced bending (see Morse and Ingard [41] pp. 214). However, one should notice the difference in physics involved in each of the two cases. The former is a wave propagation problem, and waves are caused by some combination of bulk and shear deformations at any locations along the entire plate. The process is described by a standard wave equation (Eq. (6-2) in Ewing and Press [33]) together with the appropriate boundary conditions. In contrast, the latter is a plate vibration problem and waves are generated by local deformations at sources. For example, the flexural waves are induced by bending moments of a local forcing system at the source and the process is described by a 4th order partial differential equation (Eq. (5.3.1) in Morse and Ingard [41]). Therefore, the dispersion relationships are different for the two cases. On the other hand, the wave propagation theory and plate vibration theory describe two most important aspects of wave nature in a given medium. Thus, the two theories illustrate two different behaviours of the same

phenomenon. Qualitatively, near the source, motions governed by plate vibration theory will be dominant in the wave motion; far from the source, motions governed by the propagation theory will be dominant in the wave motion. It is beyond the scope of this thesis to provide a theoretical criterion that distinguishes regions where either of the two theories is valid and transient regions where neither of the two are valid. Motivated by the observations, I believe that the radiation of acoustic waves from an ice cover is better represented by a vibration model than by a propagation model.

I approach the theoretical problem in two ways. In this section I develop the transmission coefficient of the floating ice plate for a sound wave impinging on the upper surface. This might seem a rather artificial representation of an ice cracking source, but in fact it serves as a prototype for discussing an arbitrary sound source at the ice surface, provided the bulk mechanical properties of the ice cover are not significantly altered. The analysis yields certain essential characteristics, including what I have called the angular frequency dispersion of radiated sound.

In the subsequent section I will derive an asymptotic solution for a surface stress response representative of a thermal cracking event, and also an exact solution for a point impact representative of a hammer blow. Although the radiation pattern differs for these different specific examples, it will be shown that the angular frequency dispersion characteristics developed in this section are unchanged, and would appear to be quite general for radiation from an ice plate where the fracture damage is superficial.

The model presented below consists of an ideal infinite plate of uniform thickness H (see Figure 3.20). The plate is bounded by two infinite media, air above and water beneath. Suppose an incident plane wave of unit amplitude P_{oi} insonifies the upper surface of the plate. As a result, a reflected wave P_{or} will be excited with the rest of the sound energy penetrating the plate, and a transmitted wave P_t will radiate into the water.

Taking the x, z frame as shown in Figure 3.20, the three waves can be expressed
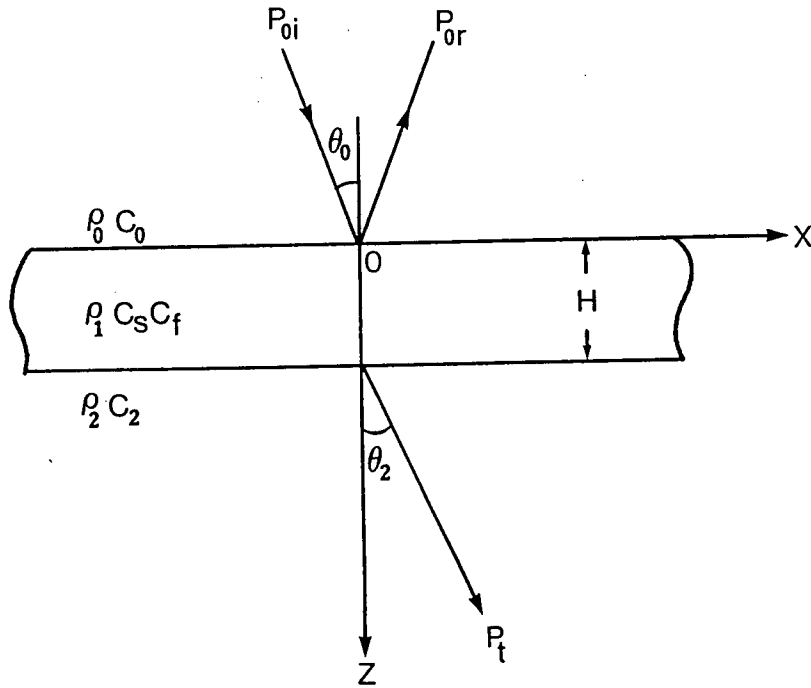
Figure 3.20: An (x, z) coordinate system used for the derivation of the transmission coefficient of an elastic plate.

as follows:

$$P_{oi} = e^{ik_0(x \sin \theta_0 + z \cos \theta_0)}, \tag{3.1}$$

$$P_{or} = A e^{ik_0(x \sin \theta_0 - z \cos \theta_0)}, \tag{3.2}$$

$$P_t = B e^{ik_2(x \sin \theta_2 + (z-H) \cos \theta_2)}. \tag{3.3}$$

Therefore, the sound pressure in the upper space is

$$P_0 = P_{0i} + P_{0r}, \tag{3.4}$$

and in the lower space

$$P_2 = P_t. \tag{3.5}$$
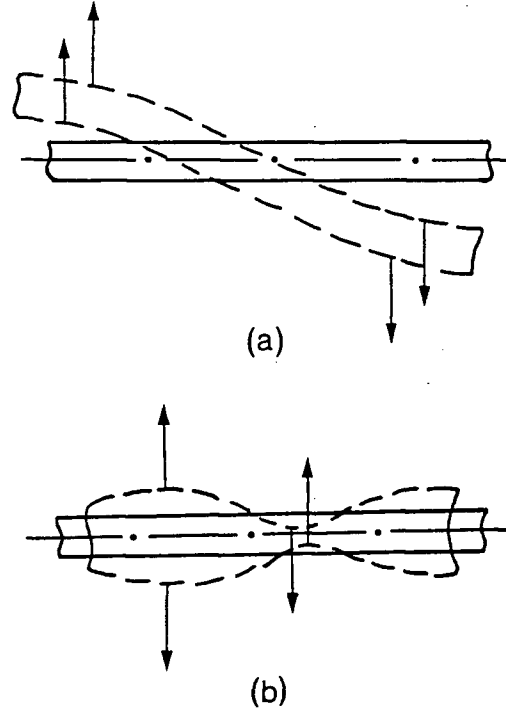
Figure 3.21: Two basic classes of vibration modes existing in an elastic plate. (a). Anti-symmetric mode; (b). Symmetric mode. Arrows indicate displacement vectors at the two surfaces of the plate.

Here, A and B are coefficients of reflection and transmission respectively, and k_0 is the wavenumber in air, and k_2 in water. I have omitted the harmonic time dependence factor $e^{-i\omega t}$.

The excited motion in the plate is the superposition of two classes of eigenmodes causing a vibration of the plate in the z direction (see Brekhovskikh [42] pp. 76). They are the *symmetric* and *antisymmetric* modes, which are illustrated in Figure 3.21. My goal is to determine B, the transmission coefficient of the plate. This parameter is analogous to the system function of a linear system. I want to express B in terms of the acoustic impedance of each of the two modes.

For a thin plate, $H \ll \lambda$ (wavelength), the governing equation of symmetric mode motion is (Eq. (11.3) of Brekhovskikh [42]):

$$\frac{\partial^2 U_s}{\partial t^2} - C_s^2 \frac{\partial^2 U_s}{\partial x^2} = -\frac{H}{2E_1}[(\sigma_1^2 - 1)\frac{\partial^2 P_s}{\partial t^2} + C_s^2 \frac{\partial^2 P_s}{\partial x^2}], \tag{3.6}$$

while for the antisymmetric mode (Eq. (11.8) of [42]):

$$M\frac{\partial^2 U_a}{\partial t^2} + \frac{E_1 H^3}{12}\frac{\partial^4 U_a}{\partial x^4} = P_a, \tag{3.7}$$

where U is the vertical displacement of the plate, and P is the applied sound pressure. Subscripts s and a denote symmetric and antisymmetric mode respectively, and $E_1 = E/(1-\sigma^2)$, is the elastic modulus for the plate where E and σ are the Young's modulus and Poisson's ratio of the plate material, respectively; $\sigma_1 = \sigma/(1-\sigma)$ is Poisson's ratio for the plate; $M = \rho_1 H$ is the mass per unit area of the plate; $C_s = \sqrt{E_1/\rho_1}$ is the longitudinal wave speed in the plate. The parameter $E_1 H^3/12$ corresponds to the plate's flexural rigidity.

Assume U and P are harmonic:

$$U = U^0 e^{i(k_1 x \sin\theta_1 - \omega t)}, \tag{3.8}$$

and

$$P = P^0 e^{i(k_1 x \sin\theta_1 - \omega t)}, \tag{3.9}$$

where $k_0 \sin\theta_0 = k_1 \sin\theta_1 = k_2 \sin\theta_2$; and U^0 and P^0 are the amplitudes of U and P respectively. Then the impedance of the plate vibration due to either mode is

$$Z = \frac{P}{V} = \frac{P}{i\omega U}, \tag{3.10}$$

where V is the vertical component of plate vibration velocity. Substitution of (3.8) and (3.9) into (3.6) and (3.7), together with (3.10), leads to the expressions of acoustic impedance for a thin plate (denoted as ZZ_s and ZZ_a respectively):

$$ZZ_s = \frac{2iE_1[1-(C_s \sin\theta_2/C_2)^2]}{\omega H[1-\sigma_1^2-(C_s \sin\theta_2/C_2)^2]}, \tag{3.11}$$

and

$$ZZ_a = -i\omega M(1 - \frac{C_f^4}{C_2^4}\sin^4\theta_2), \tag{3.12}$$

where,

$$C_2 = \frac{\omega}{k_2}$$

is the sound speed in water and

$$C_f = (\frac{\omega^2 E_1 H^3}{12M})^{\frac{1}{4}},$$ (3.13)

is the flexural wave speed in the plate.

I may now derive the transmission coefficient B for the plate. It is clear that the symmetric oscillations are caused by a sum of pressures acting on its two surfaces. From (3.4) and (3.5) I have for the symmetric response,

$$P_s = P_0|_{z=0} + P_2|_{z=H} = (1 + A + B)e^{ik_2 x \sin \theta_2}.$$ (3.14)

The antisymmetric oscillations are caused by a pressure difference between the two surfaces of the plate, i. e.

$$P_a = P_0|_{z=0} - P_2|_{z=H} = (1 + A - B)e^{ik_2 x \sin \theta_2}.$$ (3.15)

At the upper surface, V is the sum of velocities of symmetric and antisymmetric modes while at the lower surface, V is their difference. From (3.14) and (3.15) I thus find

$$V|_{z=0} = [\frac{P_a}{Z_a} + \frac{P_s}{Z_s}] = [\frac{1 + A - B}{Z_a} + \frac{1 + A + B}{Z_s}]e^{ik_2 x \sin \theta_2}$$ (3.16)

and

$$V|_{z=H} = [\frac{P_a}{Z_a} - \frac{P_s}{Z_s}] = [\frac{1 + A - B}{Z_a} - \frac{1 + A + B}{Z_s}]e^{ik_2 x \sin \theta_2}.$$ (3.17)

On the other hand, the vertical component of the plate vibration velocity can also be expressed in terms of P_0 and P_2 given by Eqs. (3.4) and (3.5):

$$V|_{z=0} = \frac{1}{i\omega \rho_0} \frac{\partial P_0}{\partial z}|_{z=0},$$ (3.18)

$$V|_{z=H} = \frac{1}{i\omega \rho_2} \frac{\partial P_2}{\partial z}|_{z=H},$$ (3.19)

where ρ_0 and ρ_2 are air and water densities respectively. Substituting (3.1), (3.2) and (3.3) into the above equations yields

$$V|_{z=0} = \frac{ik_0 \cos \theta_0}{i\omega \rho_0}(1 - A)e^{ik_0 x \sin \theta_0},$$ (3.20)

$$V|_{z=H} = \frac{ik_2 \cos\theta_2}{i\omega\rho_2} B e^{ik_2 x \sin\theta_2}. \tag{3.21}$$

Equating the right hand sides of (3.20) and (3.21) to the right hand sides of (3.16) and (3.17) respectively, yields two linear equations with respect to A and B. These may be solved to obtain:

$$A = \frac{Z_s Z_a - 4Z_0^{(0)} Z_0^{(2)} - (Z_0^{(0)} - Z_0^{(2)})(Z_s + Z_a)}{Z_s Z_a + 4Z_0^{(0)} Z_0^{(2)} + (Z_0^{(0)} + Z_0^{(2)})(Z_s + Z_a)}, \tag{3.22}$$

$$B = \frac{2Z_0^{(2)}(Z_s - Z_a)}{Z_s Z_a + 4Z_0^{(0)} Z_0^{(2)} + (Z_0^{(0)} + Z_0^{(2)})(Z_s + Z_a)}, \tag{3.23}$$

where $Z_0^{(0)} = \frac{\rho_0 C_0}{\cos\theta_0}$, $Z_0^{(2)} = \frac{\rho_2 C_2}{\cos\theta_2}$, and C_0, C_2 represents the sound speed in air and water respectively.

As for the transmmision coefficient from media 2 to 1, it can be shown

$$B_{21} = \frac{2Z_0^{(0)}(Z_s - Z_a)}{Z_s Z_a + 4Z_0^{(2)} Z_0^{(0)} + (Z_0^{(2)} + Z_0^{(0)})(Z_s + Z_a)}. \tag{3.24}$$

Equations (3.22), (3.23) and (3.24) are valid for plate of any thickness. The thin plate approximation is implemented only after equations (3.11) and (3.12) are substituted for Z_s and Z_a respectively. In the problem of radiation from an ice sheet, I can ignore the existence of air and set $Z_0^{(0)} = 0$. As a result, equation (3.23) simplifies to

$$B = \frac{2Z_0^{(2)}(Z_s - Z_a)}{Z_s Z_a + Z_0^{(2)}(Z_s + Z_a)}. \tag{3.25}$$

It is seen from (3.25) that B has a maximum when either $Z_s = 0$ or $Z_a = 0$. For $Z_s = 0$, from (3.11) (using thin plate approximation):

$$\theta_b = \sin^{-1}(\frac{C_2}{C_s}) = \sin^{-1}(\frac{C_2}{\sqrt{\frac{E_1}{\rho_1}}})$$

or

$$E_1 = \rho_1 (\frac{C_2}{\sin\theta_b})^2, \tag{3.26}$$

where θ_b is a frequency-independent radiation angle at which the plate becomes a broadband system and signals of all frequency components will pass through the plate at the same transmission rate. From now on, I will call θ_b the broadband radiation angle. When $Z_a = 0$, I have from (3.12)

$$\frac{C_f}{C_2} \sin \theta_2 = 1. \tag{3.27}$$

Substitution of (3.13) into (3.27) leads to

$$\omega_c = \frac{C_2^2}{\sin^2 \theta_2} (\frac{12 \rho_1}{E_1 H^2})^{\frac{1}{2}}. \tag{3.28}$$

This result implies that if the phase speed of free flexural waves in the plate matches the sound speed in the water, then the sound pressure caused by a cracking process in the ice will be most effectively coupled into the water. This relationship defines a characteristic frequency ω_c, which is a function of radiation angle. Consequently, an angular filtering phenomenon appears: the ice cover selects a characteristic frequency ω_c corresponding to the frequency of maximum sound transmission.

Thus the frequency content of a signal detected on a hydrophone depends upon the radiation angle at which the sound is projected into the water. If two signals arrive at the hydrophone from two different radiation angles α_1 and α_2, the ratio between the two dominant frequencies f_1 and f_2 is

$$R_T = \frac{f_2}{f_1} = (\frac{\sin \alpha_1}{\sin \alpha_2})^2. \tag{3.29}$$

Together with the presence of broadband radiation at angle θ_b, this theoretical result allows a simple comparison to be made with my observations.

I emphasize that the assumption of homogeneous ice properties used to derive equation (3.28) is a great simplification which must be considered when comparing observed results with independently determined parameters. For example Cox and Weeks [8] have recently shown that the Young's modulus E is linearly related to brine volume for dynamic measurements (also see chapter 1). The implications of this dependence will be discussed later.

3.7 Theoretical Considerations on Sound Radiation from an Elastic Plate due to Surface Forcing

In this section, I will apply Lyamshev's theory to the problem of acoustical radiation from an homogeneous ice sheet subject to point horizontal or vertical forces at its surface. Solutions to the two Green's functions will be obtained giving the underwater sound fields beneath the ice sheet. A more detailed derivation of the solutions is provided in Appendix B.

3.7.1 Plate Under Horizontal Forcing and Sound Radiation due to Thermal Cracking at the Ice Surface

Lyamshev [43] derived an expression for sound radiation from the surface of an elastic plate based on the principle of reciprocity for a point force $f(\vec{r})$ applied normally to its upper surface. Lyamshev's approach can be applied to the present problem of thermal cracking provided certain assumptions are valid. The necessary assumptions are:

1. Thermally induced horizontal stresses are concentrated at the ice surface or at a surface layer much thinner than the ice plate;

2. The resulting cracks are very shallow with respect to ice thickness.

The first assumption ensures the validity of an integral representation of the sound field due to a point force introduced by Lyamshev (see equation (9) of Ref. [43]); the second ensures that even though cracks are forming on the ice surface the approximation of the ice as an elastic plate still holds. This seems to be the case for many thermal cracking events, which occur on the skin of an ice cover in response to the maximum value of thermal stress; in contrast to the deeper cracks
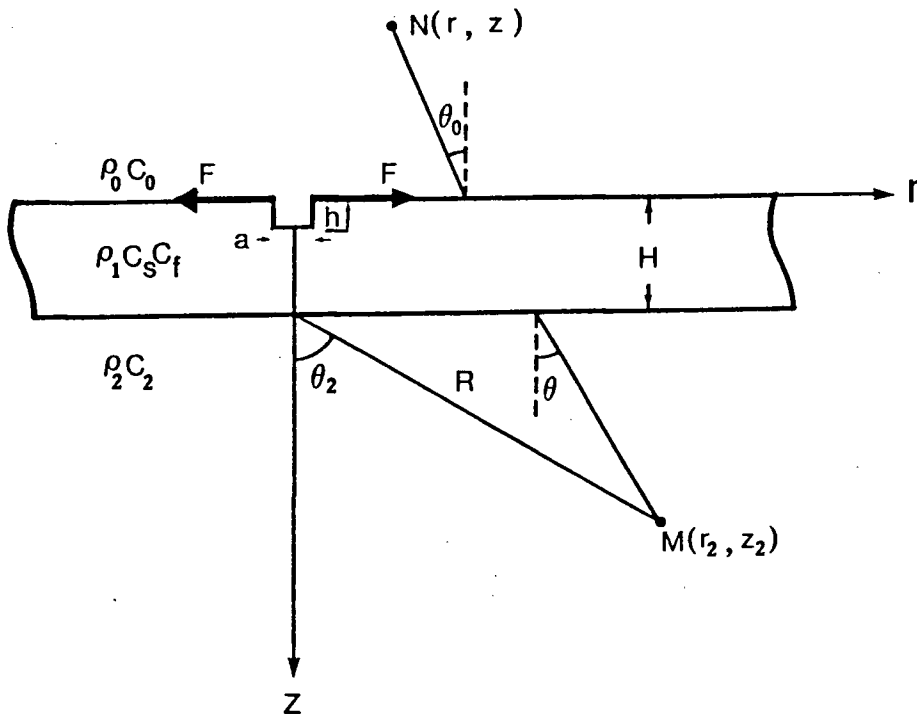
Figure 3.22: Coordinate system used for the model of sound radiation from an ice cover due to a pair of point forces F^r applied at the inner surface of a cylindrical cavity with radius a and height h.

due to some unclear internal stress discussed in chapter 2 (also in Farmer and Xie [2]), the vertical scales of these cracks are small compared to the ice thickness and wavelengths of associated acoustical emission.

I now derive a theoretical model for the sound radiated by a thermal crack and apply it to a simplified conditions illustrated in Figure 3.22 where a cylindrical (r, z, ϕ) co-ordinate system is used. My goal here is to find the sound field beneath the ice at $M(r_2, z_2)$ caused by a pair of harmonic and horizontal point forces $f(\vec{r})$ applied to the ice surface as shown in Figure 3.22. According to the principle of reciprocity, I can place an imaginary point source at M, and find the resulting scattering field on the upper surface of the ice. Once the scattering field P_s is found, the sound field at M can be expressed in terms of P_s and $f(\vec{r})$ in an integral form.

The radiation field of this point source of strength Q in the half space $z > H$ is

$$P_q = -\frac{i\omega\rho_2 Q}{4\pi R}e^{ik_2 R}. \tag{3.30}$$

This spherical wave can be expressed as a sum of plane waves incident from all directions. The scattering sound field P_s at $N(r,z)$ in the upper space $z < 0$ is found by multiplying each plane wave by the corresponding transmission coefficient B_{21} given by equation (3.24). Thus,

$$P_s(r,z,r_2,z_2) = \frac{\omega\rho_2 k_2 Q}{8\pi}\int_\Gamma H_0^{(1)}(k_2|r_2 - r|\sin\theta)B_{21}(\theta)e^{i(k_2 z_2\cos\theta - k_0 z\cos\theta_0)}\sin\theta d\theta. \tag{3.31}$$

Here, $H_0^{(1)}$ is the zero order Hankel function of the first kind, and Γ denotes the path of integration, which is given in Figure 28.1 of Ref. [42].

The radiation field at M induced by the vibration of an ice plate under a forcing system $f(\vec{r})$ is, according to Lyamshev [43] (also see Appendix B),

$$P_r(r_2,z_2) = \frac{1}{i\omega\rho_0 Q}\int\int_S \frac{\partial P_s(r,z,r_2,z_2)}{-\partial r}|_{r=a}f(\phi,z)ad\phi dz. \tag{3.32}$$

The integration is performed over the entire inner surface of a cylindrical cavity with a radius of a and height h at the upper surface of the ice.

I emphasize here that I am treating the crack at the moment of formation when the radius a is small enough that significant stress relief, and hence sound generation, has not yet taken place. The use of a cylindrical source can of course be extended to a line opening for different practical applications; in fact the solution given by (3.32) will represent the Green's function which can be used to construct solutions for cracks with parallel faces of arbitrary shapes. Similarly, the horizontal stress can be a function of depth below the surface, as modelled by Milne [15]. There is therefore little loss in generality in choosing this prototype shape of ice crack.

My model for the forcing term is a pair of point forces with density per unit area of $f(r,\phi)$. These external forces are acting on the inner side of the cavity along the radial direction (on the x,y plane). In reality, the stress will be released once

a crack is formed. Lyamshev's integral representation of a sound field requires that the driving force must be applied normally on the surfaces of an elastic body if the body is immersed in media that cannot support shear deformations. Although the model shown in Figure 3.22 is an approximation to the thermal cracking process, it can be generalized to deal with any surface failure processes in an ice cover by closing the cavity after a solution to the model is obtained.

The forces are expressed as

$$f^r(z, \phi)\vec{e_r} = \frac{F^r}{a}[\delta(\phi)\delta(z) + \delta(\phi - \pi)\delta(z)]\vec{e_r}, \qquad (3.33)$$

where $\vec{e_r}$ is a unit vector along the radial direction and F^r is the magnitude of the two point forces. It can be shown that the field due to the first term of $f^r(r, \phi)$ is identical to that due to the second term (see pp. 363 of Ref. [41]). Thus, I need only derive the field due to the first term in equation (3.33).

Substituting (3.31) and the first term of (3.33) into (3.32) yields

$$P_r(r_2, z_2) = \frac{-F^r \rho_2 k_2}{4i\rho_0} \int_\Gamma H_1^{(1)}(k_2(r_2 - a)\sin\theta)B_{21}(\theta)e^{ik_2 z_2 \cos\theta}k_2 \sin^2\theta d\theta, \quad (3.34)$$

where $H_1^{(1)}$ is the first order Hankel function of the first kind. By means of the method of steepest decent (see Appendix B), (3.34) is evaluated as

$$P_r(r_2, z_2) = P_r(R, \theta_2) \approx \frac{iF^r \rho_2 k_2 \sin\theta_2 B_{21}(\theta_2)}{\rho_0 R}e^{ik_2 R}. \qquad (3.35)$$

3.7.2 Plate Under Vertical Forcing and Sound Radiation due to Loading Failure of the Ice

For the contrasting example of acoustical radiation from a vertical point impact (representative of a hammer blow), the driving force can be modelled as a point force applied normally to the upper surface of the ice plate (i. e. $z = 0$ plane) as shown in Figure 3.23.

The radiation field at M (denoted by $P_r^n(r_2, z_2)$) due to the vibration of an ice cover under a vertical forcing system $f^n(\vec{r})$ is (see Appendix B and Lyamshev [43])
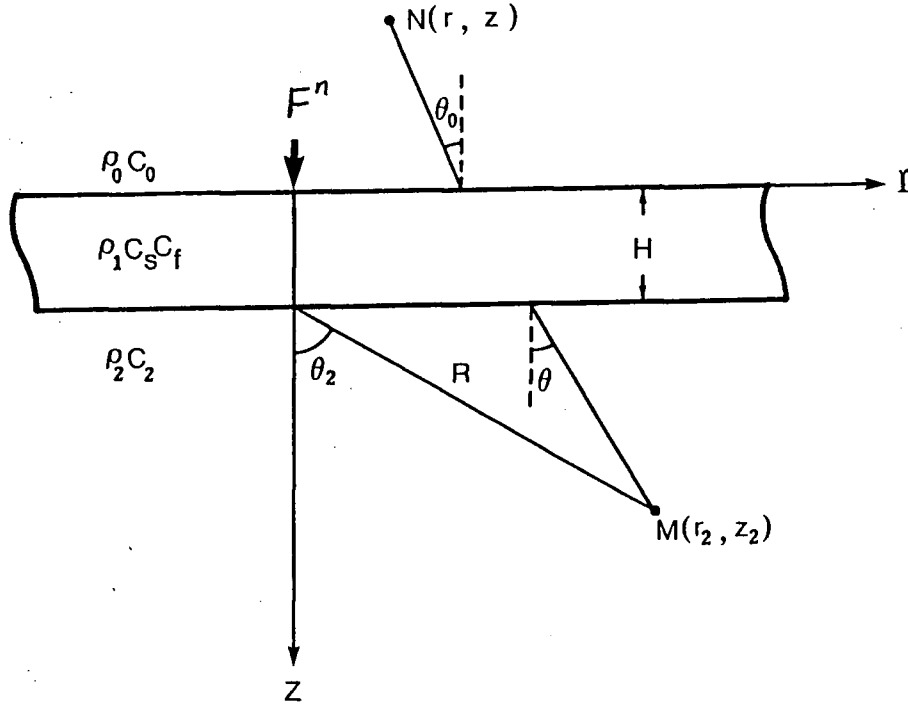
Figure 3.23: Coordinate system used for the model of sound radiation from an ice cover due to a normal impact of a point force F^n applied at its upper surface.

$$P_r^n(r_2, z_2) = \frac{-1}{i\omega\rho_0 Q} \int \int_S \frac{\partial P_s(r, z, r_2, z_2)}{\partial z}\Big|_{z=0} f(r, \phi) r\, dr\, d\phi. \tag{3.36}$$

The integration is performed over the entire upper surface of the ice. Using a point force model, I can express the forcing term in (3.36) as

$$f^n(r, \phi)\vec{e_z} = F^n \delta(\phi)\frac{\delta(r)}{r}\vec{e_z}, \tag{3.37}$$

with $\vec{e_z}$ being the unit vector along z axis, and f^n and F^n the areal density of the normal force and its magnitude respectively. Substituting (3.31) and (3.37) into (3.36) yields

$$P_r^n(r_2, z_2) = \frac{\rho_2 k_2 k_0 F}{\rho_0 8\pi} \int_\Gamma H_0^{(1)}(k_2 r_2 \sin\theta) B_{21}(\theta) e^{ik_2 z_2 \cos\theta} \cos\theta_0 \sin\theta\, d\theta. \tag{3.38}$$

By means of the method of steepest decent (see Appendix B), (3.38) is evaluated as

$$P_r^n(r_2, z_2) = P_r^n(R, \theta_2) \approx -i\frac{Z_0^{(2)}}{Z_0^{(0)}}\frac{k_2 F \cos\theta_2 B_{21}(\theta_2)}{4\pi R} e^{ik_2 R}, \tag{3.39}$$

where $Z_0^{(2)}$ and $Z_0^{(0)}$ are defined in the same way as that in (3.22) and (3.23).

Although this solution is valid for the vertical impact case, it can be applied to the study of ice cracking due to any loading failure.

3.7.3 Asymptotic Forms of the Two Green's Functions for the Sound Radiation from a Thin Plate at Angles $\neq \theta_b$

Most ice cracking sounds observed in the Arctic show dominant frequencies that are around a few hundred Hertz. This makes the ice cover acoustically thin, which is especially true for first year ice. Therefore, the discussion of the asymptotic behaviour of the two Green's functions, given by equations (3.35) and (3.39), provides a valuable insight into the physics behind the observations.

The broadband radiation angle θ_b, defined by equation (3.26), represents the special case for which the symmetric impedance vanishes ($Z_s = 0$). It is easily shown that at this angle the acoustical radiations predicted by both (3.35) and (3.39) reach maxima and no filtering effect of the ice cover is imposed on the radiated sound. A higher radiation level will occur at this angle. This phenomenon was first predicted by Gutin [44]. Greening *et al* [45] have reported this anomalously high radiation level in their ice cracking sound observations in polar pack ice regions in high Arctic. I will further discuss this phenomenon in the next section when comparing my theoretical results with observations.

For signals radiated at angles not too close to θ_b, I may simplify the two Green's functions by using the thin plate approximation which leads to two expressions for a thin plate acoustic impedance due to symmetric and antisymmetric modes respectively (see equations (3.11) and (3.12)). From now on, unless specified, only thin plate acoustic impedance will be used with Z_s and Z_a denoting the right hand sides of equations (3.11) and (3.12) respectively.

It can be readily shown from (3.11) and (3.12) that for a thin ice cover, its

symmetric impedance is much greater than its antisymmetric impedance, i. e. $|Z_s| \gg |Z_a|$. For normal incidence, this leads to $2\pi H/\lambda_s \ll 2$; i. e. the symmetric mode wavelength λ_s is much greater than the ice thickness. Alternatively, for this condition to be valid, it is required that the product of ice thickness and the frequency of radiated sound is less than $1000Hz \cdot m$, or $fH < 1000Hz \cdot m$, which is satisfied by most of the observed signals of ice cracking sound.

With this approximation, (3.24) simplifies to

$$B_{21} = \frac{2Z_0^{(0)}}{Z_a + Z_0^{(2)}}. \tag{3.40}$$

Substituting (3.24) into (3.35) and (3.40) into (3.39) respectively, I finally obtain:

$$P_r(R, \theta_2) \approx [\frac{ik_2 F^r e^{ik_2 R}}{R}][\frac{4\rho_2 C_2 \sin \theta_2}{Z_a(\omega)\sqrt{1 - 4\sin^2 \theta_2} + 2\rho_2 C_2}]. \tag{3.41}$$

and

$$P_r^n(R, \theta_2) = -[\frac{ik_2 F^n e^{ik_2 R}}{4\pi R}][\frac{2\rho_2 C_2 \cos \theta_2}{Z_a(\omega) \cos \theta_2 + \rho_2 C_2}], \tag{3.42}$$

corresponding to solutions for the horizontal stress case and the vertical point impact case respectively. The detailed derivations of the two results are given in Appendix B.

These solutions reveal several features of the sound radiated from an ice plate subject to two quite different forcing functions. These are:

- For both the vertical and horizontal forcing cases, acoustical radiation into the water is in the form of spherical waves.

- For both examples the frequency dependent directivity, given by the denominator in the second term, has a maximum at $Z_a(\omega, \theta) = 0$, leading to a resonant frequency at this angle exactly as given by (3.28). The angular frequency dispersion relationship holds regardless of the specific details of the applied force.

- For low frequency sources satisfying $f \cdot H \leq 100Hz \cdot m$ or $|Z_a| \ll \rho_2 C_2$, the vertical impact solution (3.42) corresponds to a dipole radiation pattern, as

expected for an ice plate subject to a normal force. For low frequency signals or for thin ice satisfying this criterion, the angular dependence of radiation frequency will be diminished. Thus some observations, especially those restricted to low frequency detection, may not reveal the angular frequency dispersion feature discussed above.

- For a thermal stress crack in which the forcing is horizontal, the second term in solution (3.41) vanishes for $\theta_2 = 0$. Thus no sound will be radiated vertically downwards beneath the crack. This result is physically reasonable because the horizontal forces produce no local vertical components of shear deformation. Therefore, the induced motion can only lead to a signal that will radiate into the water through horizontal radiation of longitudinal waves excited by the horizontal forcing. For low frequency sources satisfying $f \cdot H \leq 100 Hz \cdot m$ or $|Z_a| \ll \rho_2 C_2$, the radiation pattern varies as $\sin \theta_2$.

Equations (3.41) and (3.42) imply an important characteristic of radiation patterns of cracking sound: the dipole pattern can only be formed by the response of the ice to a loading failure; thermal cracking leads to a sound radiation focusing in horizontal directions. Thus, the downward radiation from a thermal crack is probably due to the tilted orientations of the ice surface on which the crack occurs.

3.8 Comparison between Theory and Observations

According to the theoretical models derived in the previous section, the observed frequency dependent radiation pattern that occurs in some events is caused by the dispersive properties of the antisymmetric vibrational mode excited by the crack. Comparisons can be made with the theory for any cracking events that do not significantly alter the local bulk properties of the ice. This condition will hold, for example, for hammer blows and superficial cracks.

A difficulty does arise however, in that most of the thermal cracks occur in multi-year ice, some of which is very rough. Other portions, especially the old ice floes, are relatively smooth. There are fewer cracks emanating from the first year ice and many of these occur quite far from the hydrophone array. Since the models described by equations (3.41) and (3.42) apply to an ice cover with flat surface, I can hardly expect good agreement with cracking events in the highly irregular ice rubble. I might expect better agreement from the smoother and flatter multi-year ice floes. The best agreement can be expected from first year ice events. However, the relatively greater distance of these sources results in only modest differences in radiation angle between the direct and reflected paths, thus limiting the angular frequency dispersion effect that can be detected. For a few nearby first year ice cracks, the non-dipole radiation pattern given by (3.41) results in a weak sea floor reflection signals that can hardly be extracted from the background noise (see Figure 3.11(k)). Aside from the artificial sources, most of the examples I have chosen are therefore from multi-year ice. The selection of natural events was determined primarily by the clarity of the dispersion effect.

The results of the comparisons are given in Table 3.2, where the frequency peaks are evaluated by taking means over the bandwidths of the corresponding spectra. The theoretically determined ratio of frequencies, R_T, are calculated from (3.29), and may be compared with the observed frequency ratio for direct to reflected paths

f_d/f_r.

For first year ice, the hammer blow sources and the four natural sources agree quite closely with the theoretical prediction. For both artificial and some natural events on multi-year ice, there is poor agreement, consistent with expectations, given the irregular nature of the ice. Interestingly however, a few of the natural sources on the multi-year ice (events 11, 13, 30, 107) agree moderately well with the model, suggesting an origin on locally flat pieces of ice.

Referring to Figure 3.15, it is apparent that in the example of the hammer blow near hydrophone B, the sound reflected from the sea floor is broadband, in contrast to other examples. This result might be explained if the radiation angle $\theta(= 27.7^\circ)$ is close to θ_b. As mentioned before, at the angle θ_b, the ice cover behaves as a broadband system and consequently transmits the full bandwidth of the source signal. As a result, the sound level at this radiation angle will deviate from, and probably be higher than, the radiation pattern given by the second term of equation (3.42). This phenomenon was first predicted by Gutin [44].

Now consider the direct path signals radiating from the hammer blow near hydrophone B and received at $5, 30$ and $70m$ (see Figure 3.15). Three dominant frequencies have been found by spectral analysis based on the maximum entropy method (see Table 3.3). It is seen that the peak frequency rises with increasing hydrophone depth from $5m$ to $30m$, corresponding to a decrease in radiation angle θ from 87° to 73°. However, no significant frequency shift occurs as the depth increases from $30m$ to $70m$. An explanation for the discrepancy at small angles is proposed later. Table 3.3 shows a comparison between observation and theory.

Knowing the thickness of the new ice and the dominant frequencies of the acoustic signals, one can use (3.28) to evaluate the elastic modulus of the ice. With $\rho_1 = 910 kg \cdot m^{-3}$, $H = 1.75m$, and $C_2 = 1438 m \cdot s^{-1}$, from Table 3.3 I derive the average value $E_1 = 1.5 \times 10^9 Pa$.

Taking the accepted value of Poisson's ratio for sea ice Stein [23], $\sigma = 0.33$, I obtain Young's modulus for the ice: $E = (1 - \sigma^2)E_1 = 1.34 \times 10^9 Pa$.

An alternative way to evaluate E_1 is to make use of the broadband radiation angle relationship given by equation (3.26). The broadband signal detected for a hammer blow near B (Figure 3.15) suggests that the source radiation angle detected at A_5 through the reflected path is close to θ_b. For $\rho_1 = 910 kg \cdot m^{-3}$, $\theta_b = 27.7°$ and $C_2 = 1436 m \cdot s^{-1}$, (3.26) gives $E_1 \simeq 8.7 \times 10^9 Pa$. Insertion into (3.28) then yields an ice thickness of $1.43m$. Thus a combination of (3.26) and (3.28) can be used to obtain both E_1 and H. The ice thickness is underestimated by the theory due to the inaccurate measure of θ_b which is shown below to be 33.1°. In general, detection of the broadband radiation angle will require a vertical array with more hydrophones. On the other hand, if there are P wave components in the arriving signals, then C_s can be measured through the delay relationship between the P wave and the acoustic wave. Young's modulus of the ice cover E_1 can then be calculated from the relationship $E_1 = \rho_1 C_s^2$.

First year ice	$f_d(Hz)$	$f_r(Hz)$	$\theta_d(deg)$	$\theta_r(deg)$	R_T	f_r/f_d
Artificial source[1] near B	550	3000	87.1	27.7	5.6	5.8
Artificial source[1] near D	400	1016	88.3	42.8	2.2	2.5
Natural event 35	650	650	~ 90	~ 90	1	1
Natural event 56	173	432	78.7	38.3	2.5	2.5
Natural event 69	100	302	76.1	32.2	3.3	3.0
Natural event 104	622	668	87.9	76.1	1.06	1.07
Multi-year ice						
Artificial source[1]	164	356	84.7	61.3	1.3	2.2
Artificial source[2]	150	360	84.7	61.3	1.3	2.4
Natural event 11	276	440	84.4	59.5	1.6	1.3
Natural event 13	134	217	85.0	65.2	1.2	1.6
Natural event 30	145	256	84.2	58.5	1.4	1.8
Natural event 43	265	801	86.1	69.3	1.2	3.0
Natural event 90	271	383	85.0	62.8	1.3	1.4
Natural event 107	173	300	82.4	50.0	1.67	1.73
Natural event 124	168	489	85.1	63.5	1.2	2.4
Natural event 129	208	454	85.0	62.9	1.3	2.2

Table 3.2: Ratios between frequencies of direct path f_d, and reflected path f_r. [1]Hammer blow; [2]Small explosive source placed on upper surface of ice.

Hydrophone	Freq. Hz	$\theta(deg)$	R_T	f/f_5
A_5	$550(= f_5)$	$87.0(= \theta_5)$	1	1
A_{30}	640	73.2	1.1	1.16
A_{70}	640	55.0	1.5	1.16

Table 3.3: Ratios between frequencies of 3 direct path acoustic waves received by 3 vertical hydrophones from a hammer blow near B.
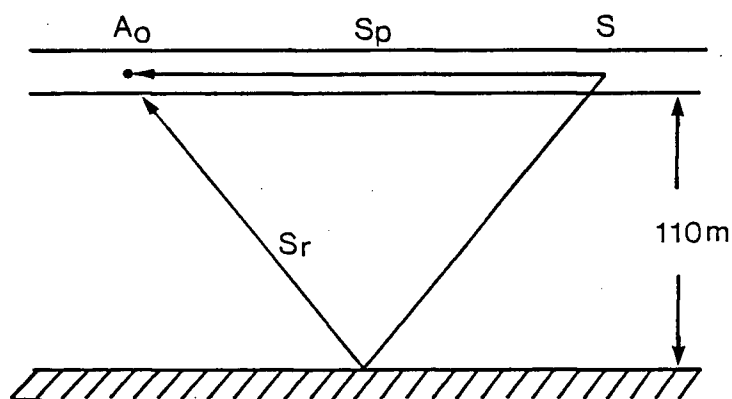
Figure 3.24: Paths illustrating the arrival of P and R waves at A_0 hydrophone for a hammer blow near B, where S_p and S_r denote P and R ray paths respectively.

3.9 Evaluation of Elastic Parameters of First Year Ice from a Sound due to a Hammer Blow

The hammer blow on the first-year ice excited four types of waves (Figures 3.15 and 3.14). Since the CTD casts (see Figure 3.5) provide a precise sound speed profile in the water column, I can evaluate elastic parameters for the first year ice based on delay relationships among F, P and acoustic waves.

3.9.1 P Wave Speed C_p

I use signals received at A_0 to calculate C_p (see Figure 3.14). Since the group speed of F is very close to the sound wave speed in the water, it is seen that A and F waves overlap to some extent. Therefore, the reflected acoustic wave R along a path S_r is chosen as a time reference for the travel time estimates along the P wave path S_p. Figure 3.24 illustrates the two paths. The difference in travel time between the two waves is:

$$\Delta t = \frac{S_r}{C_w} - \frac{S_p}{C_p},\tag{3.43}$$

where $C_w = 1438 m \cdot s^{-1}$ is the mean sound speed in the water column. With $\Delta t = 130 ms$, $S_p = 100 m$ and $S_r = 241.66 m$, equation (3.43) yields

$$C_p = 2628 m \cdot s^{-1}.$$

Thus the radiation angle θ_2 of the P wave from ice to water is:

$$\theta_2 = \sin^{-1}(1436/2628) = 33.1^0,$$

where $1436 m \cdot s^{-1}$ is the sound speed near the ice – water interface (see Figure 3.5). This result may be compared with the broadband radiation discussed in the previous section, for which the geometry limited me to a radiation angle of $27.7°$.

To confirm the above evaluation, I can use C_p and geometrical relationships between the source and vertically spaced hydrophones to calculate the travel time difference between the P wave and direct acoustic paths from source to A_5, A_{30} and A_{70} respectively. The calculation leads to time delays between the P and A waves for the three hydrophones, with which I can make a comparison between the calculated and measured delays. Table 3.4 gives the results, where the travel time along the P wave path is calculated by means of ray tracing routines, with a linear sound speed profile indicated by the dashed line in Figure 3.5 used as input. It is seen that the

Hydrophone	dt(ms) calculated	dt(ms) measured
A_5	28.8	30.0
A_{30}	17.2	17.6
A_{70}	6.2	8.0

Table 3.4: Comparison of travel time difference for P and A waves from the hammer blow to 3 vertically spaced hydrophones.

estimated C_p does give a correct delay relationship for the array system. Therefore, I accept $2628 m \cdot s^{-1}$ for C_p in first year ice.

3.9.2 Shear Wave Speed β

As mentioned above, the flexural wave is anomalously dispersive. Judging from the signals detected at A_5 (Figure 3.14), it is estimated that the frequency of maximum group velocity for F is about $60 Hz$, and the time delay between the P and F waves is approximately $32 ms$ at A_0 channel. Therefore, the maximum group speed for F is:

$$U_{max} = 1428 m \cdot s^{-1}.$$

According to Ewing and Press (Figure 6-7, [33] where Poisson's ratio has been assumed to be 0.345 for sea ice), the shear wave speed β is

$$\beta = \frac{U_{max}}{0.8} = 1785 m \cdot s^{-1},$$

and the corresponding phase speed is

$$C_{max} = 0.55\beta = 982 m \cdot s^{-1}.$$

My calculations of U_{max} and C_{max} for the flexural wave are consistent with the observations (Figure 3.14). The fact that U_{max} is close to the sound speed in the water implies that F and A waves arrive almost simultaneously at the hydrophone A_5; the fact that C_{max} is less than the sound speed in the water implies an evanescent property of the F wave.

3.9.3   Compressional Wave Speed α

Knowing β, I can calculate the compressional wave speed of the first year ice. From equation (1-12) in reference [33], it follows that

$$\alpha = \beta[\frac{2(1 - \sigma)}{1 - 2\sigma}]^{1/2}. \tag{3.44}$$

With $\beta = 1785 m \cdot s^{-1}$ and $\sigma = 0.345$, it yields from (3.44) that

$$\alpha = 3669.4 m \cdot s^{-1} \ .$$

3.9.4   Lamé's Constants λ_e, μ_e and Young's Modulus E

The compressional, shear wave speed and Young's modulus can be expressed in terms of the Lamé's constants, λ_e and μ_e (see Chapter 1 of Ewing and Press [33]). That is,

$$\alpha = \sqrt{\frac{\lambda_e + 2\mu_e}{\rho_i}} \ ,$$

$$\beta = \sqrt{\frac{\mu_e}{\rho_i}} \quad ,$$

and

$$E = \frac{\mu_e(3\lambda_e + 2\mu_e)}{\lambda_e + \mu_e} \quad ,$$

where $\rho_i = 910 kg \cdot m^{-3}$ is the first year ice density. With estimated values for α and β, I obtain

$$\mu_e = 2.9 \times 10^9 \quad Pa,$$

$$\lambda_e = 6.45 \times 10^9 \quad Pa,$$

and

$$E = 7.8 \times 10^9 \quad Pa.$$

This value is higher than $1.34 \times 10^9 Pa$, a value estimated by using direct path radiated sound from the same hammer blow source. The discrepancy is probably caused by the profile properties of the inhomogenous ice plate, which is the topic of discussion in the following section.

3.10 Interpretation of Young's Modulus Evaluations

Cox and Weeks [8] have recently described profiles of Young's modulus in sea ice determined by *in situ* measurements. For their samples, much higher values ($7 \sim 9 \times 10^9 Pa$) occur near the surface than in the porous region at the base of the ice ($E \approx 2 \times 10^9 Pa$). My thin plate vibration model is based on uniform ice properties, but the evaluation of Young's modulus through radiated sound of the same source from different paths depends on different aspects of ice behaviour, and is therefore more or less sensitive to different portions of the real profile.

For the thin plate vibration response of the ice, angular frequency dispersion leads to $E = 1.34 \times 10^9 Pa$. The vibration characteristics depend on bulk properties of the ice in the vicinity of the source. In particular the asymmetric response, on which the angular frequency dispersion depends, is associated with the local bending of the plate, and thus presumably depends on some integral property of the Young's modulus profile. Thus a calculation of E by this method might be expected to yield an intermediate value.

Use of the delay relationships between the F and P waves results in a slightly different sensitivity to the profile. The flexural wave speed also depends on the complete vertical profile although in this case I exploit the waveguide properties of the ice so that the properties are in some sense an average along the horizontal propagation path, instead of being locally determined as in the plate vibration measurements. The situation is different for the P wave. In this case, the higher propagation speed near the upper surface of the ice, where E is greatest, will dominate the time delay measurement of P wave speed. Although a full analysis of this problem lies beyond the scope of this paper, the somewhat greater value of $E = 7.8 \times 10^9 Pa$ found by the F and P wave relationships are consistent with this explanation. No independent measurement of the Young's modulus profile was made, but these results are qualitatively consistent with those of Cox and Weeks [8].

Finally, the broadband transmission angle measurement depends on the symmetric (i. e. P mode) response, and is again most sensitive to the higher values of E at the top of the profile. My measurement is only approximate, because of the limited number of hydrophones in the vertical array, but the relatively higher value of $E = 7.8 \times 10^9 Pa$ is again consistent with this explanation.

3.11   Ridging Event

Before closing this chapter, I will briefly describe an acoustical event related to ridging. Figure 3.25 shows a $360ms$ long sound pressure record of a ridging event. This event occurred $216m$ away from the array centre during a period when background noise level was very low. It is possible to observe *the ice mode radiation* i. e. the P wave, provided the source is within a few hundred metres. The ice failure occurred at the weaker ridge near the boundary between first-year ice and multi-year ice area (see Figure 3.3). The P wave is clearly seen on A_{70} channel in Figure 3.25, but not on the A_0 or A_5 channels. One can see a much weaker precursor on channel A_{30}, which is the same P wave as that appearing on A_{70}. The dominant P wave frequency is around $70Hz$, and its initial phase is negative. Thus a rarefying process is responsible for the acoustical emission. Pritchard [20] has interpreted ridging failure in terms of bending of an ice plate and sliding between ice plates. However, failures due to ice bending usually cause P wave radiation with a positive initial phase as is also the case for the hammer blow signal in Figure 3.14. The ridging deformation revealed by this event indicates that the failure process is associated with a crushing process that seals air or vacuous gaps between ice floes. The acoustical signal is similar to that emitted from a collapsing air bubble in a fluid as illustrated by Longuet-Higgins [46].

No conclusive remarks on sound due to ice ridging can be made based on this individual event. The background noise level is too high in my data to identify P waves for most of the cracking events. As a result, I am unable to group as many ridging events with identifiable P waves as it is required to conduct a statistical analysis on ridging related ice failure. Nevertheless, based on the air photo (Figure 3.3) and the location of this event on the photo, for the first time a naturally occurring acoustical event is correlated with a ridge building process with high confidence. Therefore, I can say that

- Ridging can cause collapse between adjacent ice floes at spots where a ridge
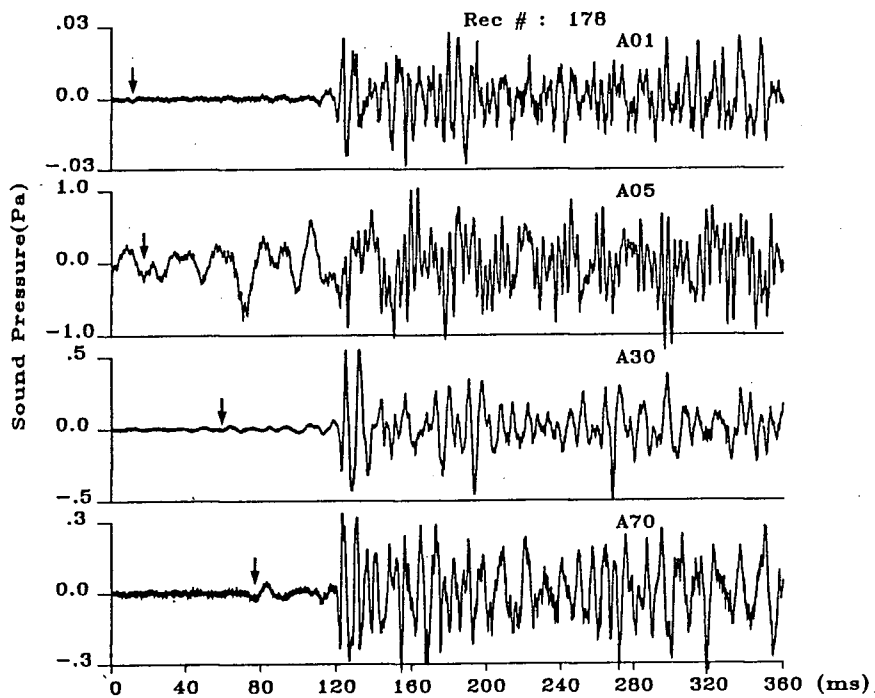
Figure 3.25: Sound pressure time series recorded by the 4 vertically spaced hydrophones for a ridging event. Arrows indicate the arrival of a weak P wave.

is being built;

- The frequency of the P wave is only half that generated by the hammer blow, which is ~ 140 Hz (see Figure 3.14). This difference means that the ridging event has not triggered any normal P wave modes in the ice cover. Thus, the observed frequency is probably related to the failure process at the ridge.

3.12 Concluding Remarks on Chapter 3

Ice cracking generates a sharp, broadband source which can be located using a 3-dimensional array of hydrophones. Deployed near the boundary between first year and multi-year ice, my instrument detected a predominance of sources on the multi-year ice, with relatively few on the first year ice during a cooling period. Even on the multi-year ice , however, the cracks were far from being evenly distributed. Cooling leads to thermal tension concentrated along the ice surface and decaying exponentially with depth (Milne [15]). This effect will be most pronounced in rubble ice areas which have uneven snow cover including exposed ice faces. Thermally induced cracking in multi-year ice was the dominant source of sound during my measurement period, with local events occurring at the rate of $1 \sim 2$ per second.

Thermal tension creates a force system on the ice surface. A small surface crack typical of that produced by this effect does not significantly alter the overall mechanical properties of the ice sheet. The acoustical response is therefore appropriately analyzed in terms of plate vibration theory. This theory provides a theoretical framework which apparently has not previously been applied to a floating ice sheet. In particular, this theory predicts an angular dependence of the radiated frequency which is consistent with many of my observations. It should be emphasised that the analysis is appropriate only for shallow cracks. Large cracks, such as those discussed previously in chapter 2 are more appropriately analyzed in terms of a finite volume displacement.

Cracks radiating from far field ($> 1km$) first-year ice show acoustical features that differ somewhat from multi-year ice cracks. Examples are shown in Figure 3.11(a, i, j, k); Figure 3.26 for example shows the corresponding spectrogram for Figure 3.11(a).

The source is a short pulse centered on $622Hz$. The reflected path at this range partly overlaps the direct path signal; the dominant frequency shift is from $622Hz$ to $668Hz$ in the reflected portion. This frequency shift is consistent with a local
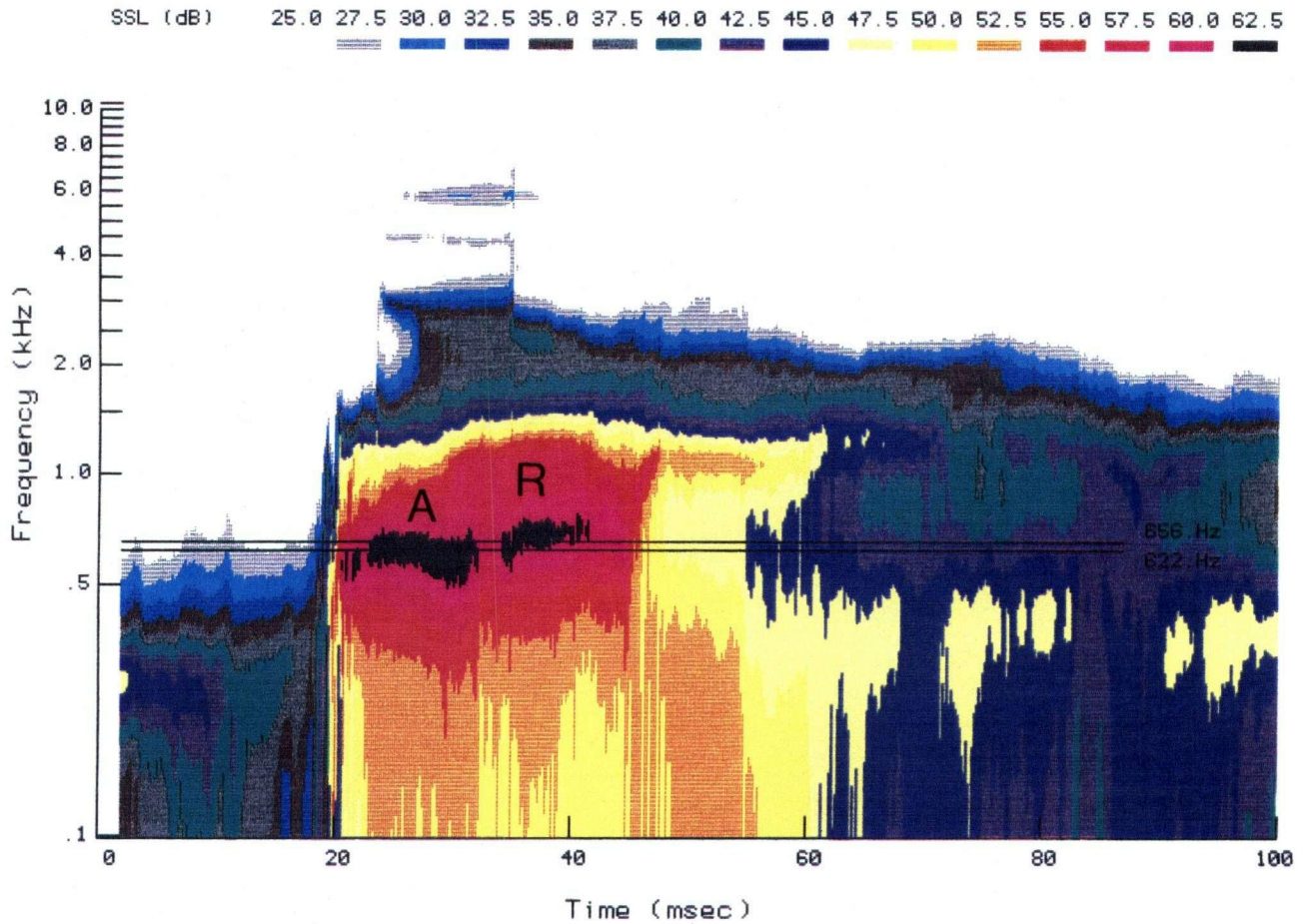
Figure 3.26: Spectral intensity as a function of time for far field event 104 detected at hydrophone A_{30}. The predicted frequencies are indicated by two lines for direct path acoustic wave A ($622Hz$) and sea floor reflected wave R ($656Hz$).

ice thickness at the source of $1.4m$, similar to, but less than that in the vicinity of my hydrophone array. The spectrum in Figure 3.26 also illustrates a high frequency component of about $6kHz$, similar to the example described previously in chapter 2. At this point I do not know for sure the reason why far field cracking sounds emanating from the first year ice are significantly shorter than those from multi-year ice; I anticipate that a different forcing mechanism may be responsible, but it is apparent both in this and other examples that the angular frequency dispersion characteristic of radiation from thin plate vibration is present.

Cracks radiating from near field ($< 1km$) first-year ice have acoustical features that also differ somewhat from multi-year ice cracks. Examples are shown in Figure 3.11(n, o). The most interesting feature is that none of those near field events show distinct sea floor reflection signals, which implies a non-dipole radiation pattern. The fact that near field first year ice events lack strong sea floor reflections while far field first year ice events show very strong reflections indicates that the radiation pattern predicted by my theoretical model (3.41) for thermal cracking sound is in good qualitative agreement with the observations. According to equation (3.41), the closer a source is to a receiver, the smaller the radiation angle (θ) for the reflected path. Hence, less sound will propagate to the receiver along the reflected path for the nearby events than for the far field events.

It has been shown from the observations that many of the acoustical events occurred in multi-year ice show distinct sea floor reflections with frequency shifts with respect to the direct path signals. If the plate vibration model is valid for multi-year ice and the forcing for multi-year ice cracks is due to thermal tension applied in parallel to the ice surface, then according to equation (3.41) the strong sea floor reflection occurs only when the ice surface is tilted vertically. Intuitively, I feel that the plate model is a poor representation for rubble ice in multi-year ice field and a more realistic model has to be developed to predict the acoustical behaviour of rubble ice subject to thermal tension stress. However, the conclusion based on the plate model is probably true. Specifically, cracks caused by thermal tension stress

tend to radiate acoustical energy primarily parallel to the ice surface.

In all of the data I have analyzed both in this experiment and in Amundsen Gulf (see chapter 2), it is certain that the primary origin of ambient sound beneath a floating ice sheet is the direct path and sea floor reflected signals. Sound scattered or leaking due to ice mode radiation in the ice waveguide provides at most a minor contribution. Although high frequency components ($\sim$ 5 to $6kHz$)are caused by the fine structure in the cracking process, there is an important class of ice cracking events in which the dominant frequency of the base band signal is due to the unique angular filtering characteristics of the ice.

Detailed analysis of radiation from a hammer blow on the ice allows evaluation of the elastic properties. The evaluation is of course limited by the ice plate model, which as yet does not include the possibility of a variable profile of Young's modulus through the ice. Extension of the theory to allow for this possibility remains an avenue for further research.

Finally it should be noted that in one important respect the present theory fails to account for the observations. The data show that angular frequency dispersion proceeds only as far as a certain frequency. For example in the hammer blow response (Table 3.3), the dominant frequency rises with increasing hydrophone depth (i. e. decreasing radiation angle), but only up to a frequency of about $640Hz$. This effect, which is believed due to the limitations of a purely elastic description of ice properties, suggests the possibility of further research into ice physics using higher frequency signals.

Chapter 4

An Investigation of the Sound of Ice Rubbing Triggered by the Break-Up of Sea-Ice

4.1 Motivation

So far I have studied ice response to thermal stress and internal stress transmitted through the ice cover. In all the cases discussed no observable motion occurred in the whole ice field. Therefore, the ambient sound data collected during these periods of time contain very little information related directly to ice-ice interactions. The dynamic response of the Arctic ice field to wind and ocean currents is another important aspect of sea ice studies, especially in marginal ice zones (MIZ). Makris [47] made use of low frequency ambient sound measured under drifting ice floes in the Fram Strait to correlate the sound with local forcing, and found that surface gravity wave forcing and ice concentration are the two primary correlates of the noise in the MIZ. Makris [47] claimed that environmental forces, e. g. , wind stress, internal ice stress and moment, thermal tension force, are uncorrelated with MIZ noise. However, high quality ambient sound data are needed to gain a better understanding

on how ice floes interact with each other and generate MIZ noise. In the 1987 ambient sound experiment (chapter 2), the ice cover of the instrumentation broke away from land during an ocean storm and drifted $90km$ from the deployed site. The subsequent noise was recorded for 16 hours. This data set provides an opportunity for the study of ice-ice interactions and response of the ice cover to currents and wind. One of the signals I am to analyze in this chapter is a pure tone sound caused by rubbing between ice floes. The following analysis is preliminary and I hope that a more thorough study of this kind of signal will eventually lead to a better understanding of ice-ice interaction.

4.2 A Review of the Problem

The pure tone sound beneath Arctic sea ice has been observed and treated as an interference noise that affects underwater communications in the arctic ocean (Dwyer [48], [49]). Although this kind of sound is known to be caused by ice-ice, ice-structure interactions (Määttänen [50], [51]), very little theoretical work and virtually no experimental work has been done to understand its generation mechanism.

Ice-ice interaction is of great interest to Arctic oceanographers and engineers. The momentum transferred to sea-ice from wind and current determines the behaviour of the ice cover; the ice will either crack (see chapters 2 and 3) and even break up into a few pieces, or exert a great amount of pressure on engineering structures. The floe collision process has been studied by Shen *et al* [52]. Buckingham and Chen [21] established a numerical model to investigate sound caused by crushing between ice cubes, which leads to an impulse like signal. The break-up of sea ice consists of two major stages:

1. dismantling of the ice cover;

2. ice-ice interaction which includes ice crushing, ice rubbing, etc.

During the 1987 experiment, one of the ice rubbing events occurred only 150 metres away from the centre of the hydrophone array. The complete acoustic signal emitted from this event was recorded. The analysis of the signal leads to a scenario for sea ice break-up which serves as a starting point for further studies on the process of ice breaking in the Arctic.

In this chapter, I will examine this event and the ice breaking scenario revealed from the event. A theoretical description based on a steady solution to a boundary value problem will be given to demonstrate how the observed pure tone sound can be triggered in an ice floe by rubbing.

4.3   The Experiment and Observations

The ambient sound experiment was conducted in the spring of 1987 in Amudsen Gulf in the Beaufort Sea. A detailed description of the experiment is given in chapter 2. A 4-hydrophone array system was deployed in the water beneath a first-year ice cover of one metre thickness, see Figure 2.2. The ice was landfast at the beginning of the experiment. However, two days later it started breaking away from the land during a storm. By the time the array was recovered, it was found to have drifted about 90 *km* from the original site (see Figure 2.1). Figure 4.1 shows the acoustical transient process of the ice from landfast to free drifting states. It is seen that at about 17:00:00 March 20, the root mean square of the ambient sound level jumps to 0.15 *Pascals*. At this time, the wind had been blowing from the south for about 12 hours. Listening to the corresponding acoustical signal, I believe that this is the moment when the ice starts to break-up.

One of the events occurred near the hydrophone array is analyzed in detail. Figure 4.2 shows the spectrum of this event as a function of time.
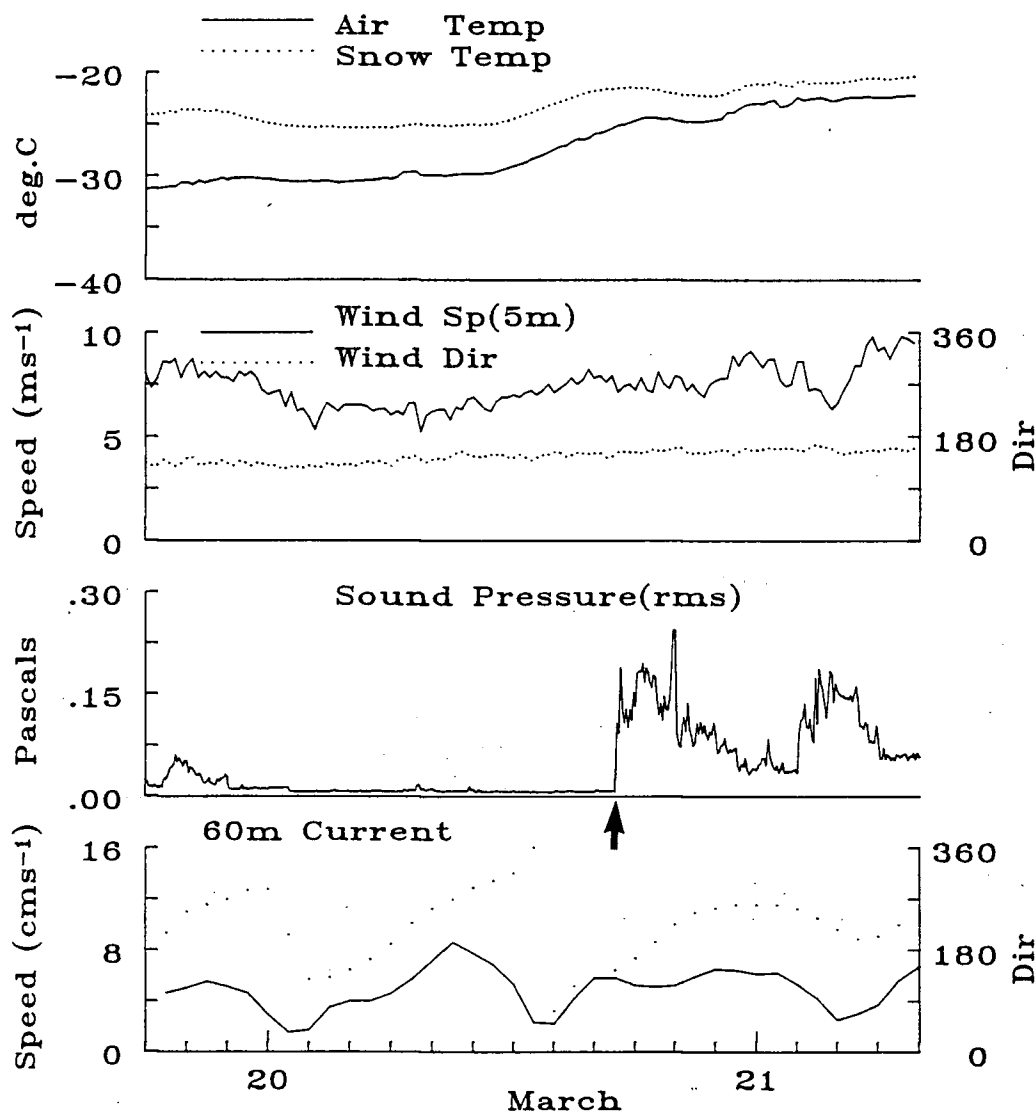
Figure 4.1: Statistic overall view of environmental and acoustic data collected during section 2 of the 1987 ambient sound experiment in Beaufort Sea. The arrow identifies the sudden increase in underwater sound level at the time of break-up.
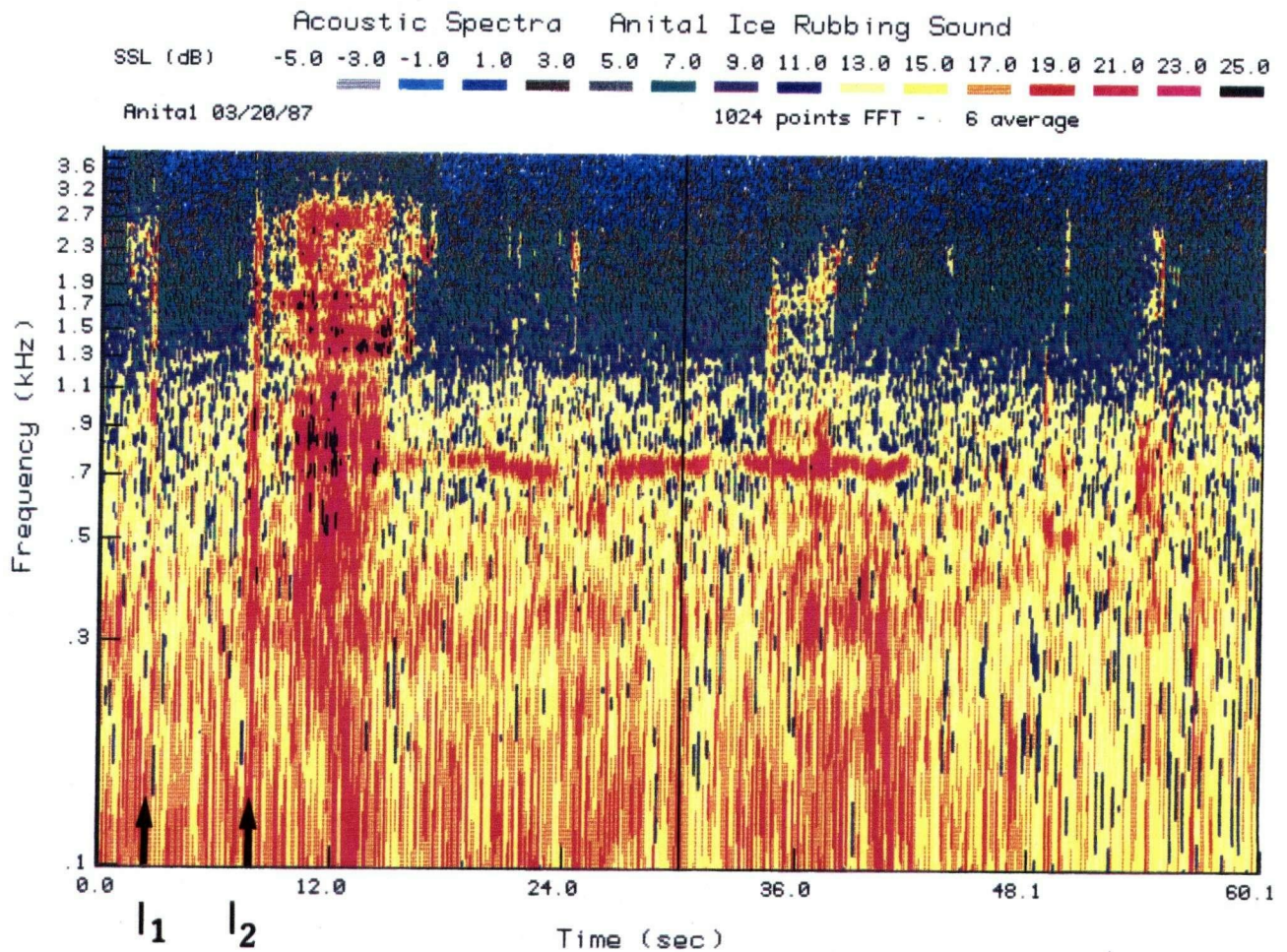
Figure 4.2: Spectral intensity as a function of time for an ice breaking event detected at A_{30}. Colours represent intensities of acoustical signals.
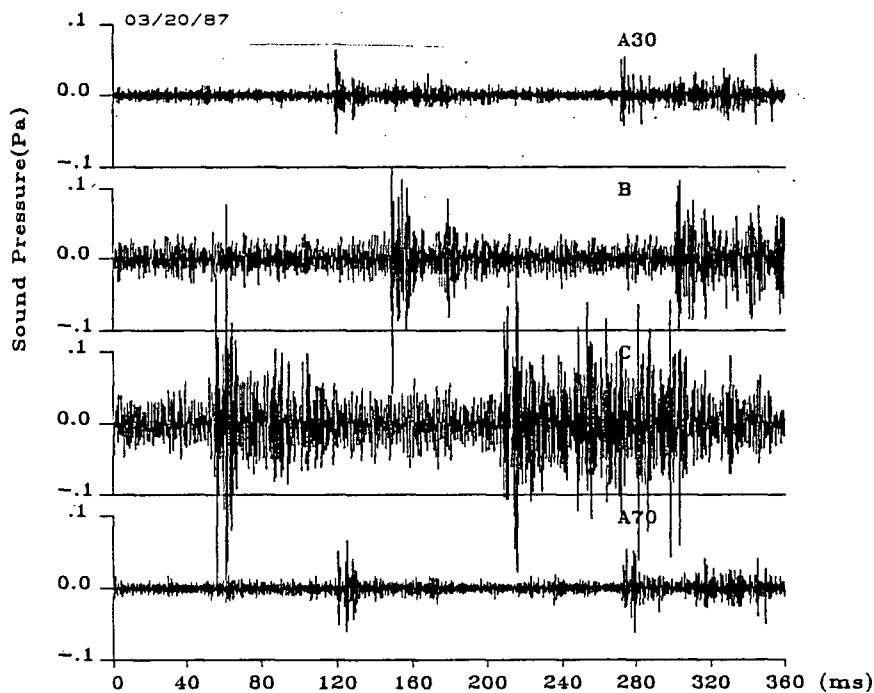
Figure 4.3: Sound pressure time series recorded by the 4 horizontally spaced hydrophones for sound pulse I_1, which occurred at $150m$ range.
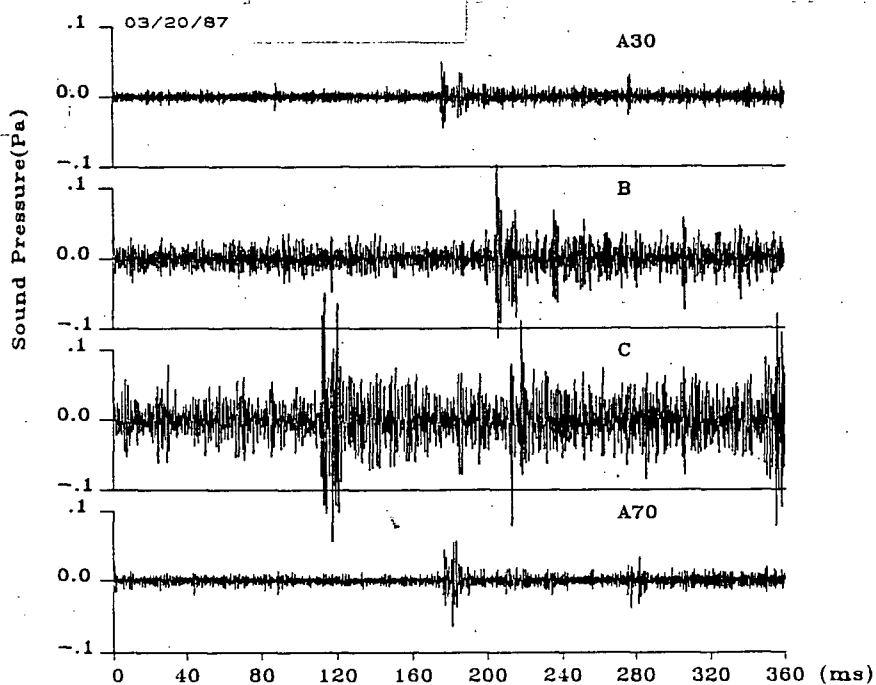
Figure 4.4: Sound pressure time series recorded by the 4 horizontally spaced hydrophones for sound pulse I_2, which occurred at $150m$ range.

This event starts with two impulse type pulses (labelled as I_1 and I_2 in Figure 4.2) which are 6 seconds apart. Their time series are shown in Figures 4.3 and 4.4. Correlation analysis shows that the two pulses originate from the same location which is about 150 metres away from the centre of the hydrophone array. Right after I_2, the ice emits many broadband sound pulses into the water. This noisy process lasts about 8 seconds. At this stage the ice floe probably gains freedom to move with respect to its adjacent floe. Meanwhile, the wind and current keep applying stress on the whole ice field, which makes the adjacent ice floes rub against each other. Consequently, a fascinating intermittent pure tone sound radiates from the ice cover. The sound lasts about 25 seconds with three segments. The last segment of pure tone signal overlaps another breaking event. The frequency of the tone is centered at 778 Hz with a minor fluctuation (see Figure 4.2). The following hypothesis is proposed for this ice breaking event:

Phase 1 Under the stress of strong wind or currents, ice starts breaking at locations where the ice is weaker or the stress is greater. This initial process of breaking emits individual sound pulses such as I_1 and I_2 shown in Figures 4.3 and 4.4. Once a crack occurs, it is most likely that further failure related cracks will occur around that spot. This hypothesis is consistent with the classical rupture criteria given by equation (1.12) in chapter 2 which states that as a crack lengthens, the stress required for further extension of the crack decreases.

Phase 2 The ice keeps breaking as a continuation of *phase 1*. *Phase 1* and *phase 2* form a positive feedback system, i. e. once ice starts breaking, more failure events will be triggered if wind and current keep applying stress to the ice. Consequently, more impulsive sound is radiated into the water. Therefore, the underwater sound field beneath the ice is a superposition of many sound pulses. The process will persist until large scale faults are formed separating the once integral ice into several individual floes. At this moment, the ambient sound level sharply decreases, see Figure 4.2.

Phase 3 The wind and current keep supplying momentum to the ice floes. Since the ice floes at this stage are still very close to each other, there is little opportunity to achieve rapid motion normal to neighbouring floes. Therefore, crushing events are rare. However, the adjacent ice floes are relatively free to move *along* the new fault. Consequently, the ice floes start rubbing with each other and shear failure will develop at the edges of each ice floe. It is reasonable to assume that shear failure is the final phase of a complete break-up process. The shear failure due to ice rubbing excites a pure tone signal as shown in Figure 4.2, which can be described in terms of a boundary value problem.

4.4 Theoretical Considerations

The process of ice rubbing has been studied as a potential danger to Arctic engineering structures by Määttänen [50], [51]. The mechanism of rubbing is one of the classical topics treated in non-linear vibration theory (see Mclachlan [53] and Hagedorn [54]) where the rubbing related vibration is termed a self-excited oscillation. A simple example is the pure tone produced on a violin string subjected to the rubbing of a bow. In this case, the forcing term arises from friction between the vibrating string and a unidirectional moving bow. In this example, the length and tension of the violin string determine the frequency, which is independent of the action of the bow.

A quite different situation occurs if there is no strongly resonant characteristic to the oscillating member. For example, the squeal of an automobile brake depends on the rotation speed pressure applied and possibly the surface properties. In the first case, the oscillation of the violin string may be analyzed as a linear problem. On the other hand, in the second case a full analysis requires inclusion of the nonlinear boundary condition.

In the case of rubbing ice, it appears that the generated tone is essentially constant which will be shown latter to be the fundamental frequency of SH modes in the ice. This lends support to the concept that a resonant characteristic of the ice is dominating the mechanical response. It appears that a likely source of this resonance lies in the narrow band response of the ice to SH waves.

The forcing, whether applied to a resonant or non-resonant system, originates from the frictional force (zero frequency) which is a unique function of relative velocity between the two rubbing bodies. Mclachlan [53] and Hagedorn [54] have used a mass-spring system to examine the energy supply and dissipation process for the case where a moving belt of constant speed is rubbing with the mass. A superposition of many such mass-spring systems simulates the real slip-stick movements of the Earth's crust over a fault zone (Levi [55]). In short, it is the negative damping

effect of the dry friction that keeps feeding energy into the mass-spring system. This is a nonlinear problem; the nonlinearity stems from the abrupt transition between static and dynamic friction. When the energy extracted from the other moving body is equal to that dissipated through positive damping, the vibration reaches its final amplitude. The frequency of vibration is determined by the resonant frequency of the system and frictional force or the relative velocity between the rubbing bodies. In Arctic engineering problems, a structure must be designed in such a way that the rubbing between the structure and surrounding ice floes will not excite resonant oscillations (Määttänen [50], [51]).

It is believed that rubbing will induce shear deformation at the edges of an ice floe. This kind of deformation will most likely trigger shear waves having a horizontal polarization, i. e. SH waves. In the following, a wave equation will be defined in an ice floe with the rubbing effect coupled to the floe through its boundary with the adjacent ice. This boundary value problem is then solved for the linear interaction case, giving a series of normal modes. A numerical approach will have to be adopted to solve the same problem for the nonlinear interaction case, which is beyond the scope of this thesis.

4.4.1 Rubbing Induced SH Waves in a Finite Ice Plate

The model used in the following derivation is shown in Figure 4.5 where the ice floe A has a finite length L in the x direction; ice floe B keeps rubbing A with a velocity V_b along the y axis. Consequently, shear deformation occurs along the y axis, which causes SH mode vibrations in the ice plate. The wave equation for SH waves in A is

$$\frac{\partial^2 U}{\partial t^2} - C_S^2 \nabla^2 U = 0, \tag{4.1}$$

where

U ice particle displacement along y direction;

$C_S = \sqrt{\mu/\rho}$: shear wave speed in the ice;
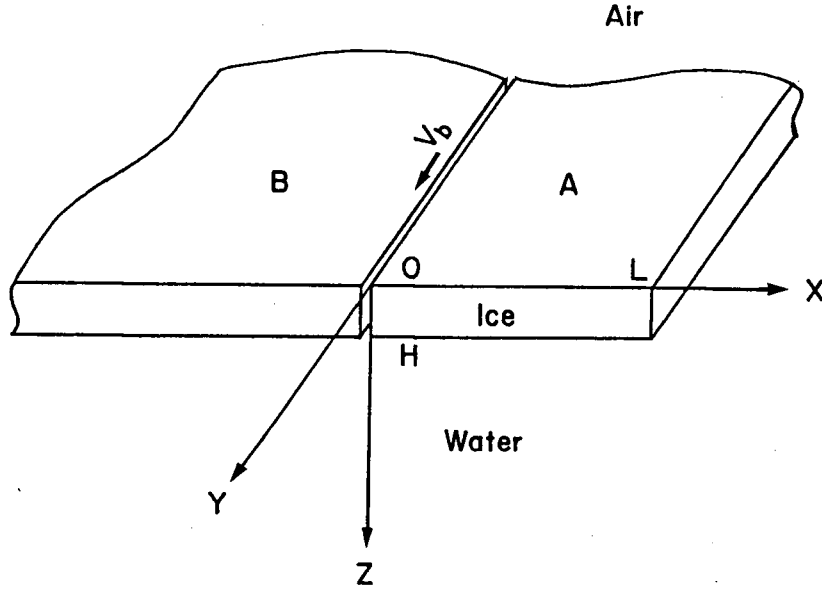
Figure 4.5: An (x, y, z) coordinate system used for the derivation of the ice rubbing sound model in a finite ice plate.

μ: shear modulus of the ice;

ρ: ice density.

The shear stress must vanish at three boundaries (see page 31 of Ref. [42]):

$$\mu \frac{\partial U}{\partial z}\big|_{z=0,H} = 0, \tag{4.2}$$

$$\mu \frac{\partial U}{\partial z}\big|_{x=L} = 0. \tag{4.3}$$

Equation (4.3) means that the end of the ice plate A at $x = L$ is free of stress.

Ice floe A is subjected to ice floe B's rubbing at $x = 0$. The corresponding boundary condition can be expressed as

$$\mu \frac{\partial U}{\partial z}\big|_{x=0} = F(z, \omega, V_b - \frac{\partial U}{\partial t}\big|_{x=0})e^{-i\omega t}, \tag{4.4}$$

where F is the stress due to rubbing by ice floe B. In general, F is a function of relative velocity between the two ice floes. A typical curve of F versus $V_b - \frac{\partial U}{\partial t}$ is

given in Figure 51 of Mclachlan [53]. F decreases as $|V_b - \frac{\partial U}{\partial t}|$ increases. However, the SH wave in the ice floe has a velocity amplitude much less than $|V_b|$; therefore, in this case F is approximately independent of the SH wave velocity at the edge of ice floe A. Thus, the boundary condition at $x = 0$ becomes

$$\mu \frac{\partial U}{\partial z}|_{x=0} = F(z,\omega)e^{-i\omega t}, \tag{4.5}$$

where $F(z,\omega)$ is modelled as

$$F(z,\omega) = \begin{cases} F_0(\omega) & 0 < z < H \\ 0 & \text{elsewhere.} \end{cases} \tag{4.6}$$

The steady solution to this problem is the response of ice floe A to a harmonic rubbing stress at its edge. The response to an impulse-shape stress can be obtained by integrating U over all frequencies.

Choosing the time dependence as $e^{-i\omega t}$, I obtain from equation (4.1) and boundary conditions (4.2), (4.3) and (4.5) that

$$U(x,z,t,\omega) = \frac{4HF_0(\omega)}{\mu} \sum_{n=0}^{\infty} \frac{\sin k_n(x - L)}{(2n + 1)^2 \sin k_n L} \cos \frac{(2n + 1)\pi}{H} z e^{-i\omega t}, \tag{4.7}$$

where $k_n = \sqrt{(\omega/C_S)^2 - [(2n + 1)\pi/H]^2}$ with $n = 0, 1, 2, \ldots$ being the nth mode wavenumber along the x axis.

4.4.2 The Relationship Between the Pure Tone and Shear Wave Speed C_S

It is seen from equation (4.7) that a resonant phenomenon occurs when $\sin k_n L = 0$ which leads to

$$k_n = \sqrt{(\omega/C_S)^2 - ((2n + 1)\pi/H)^2} = \frac{n_x \pi}{L}, \quad n_x = 1, 2, 3, \ldots. \tag{4.8}$$

Thus, (4.8) yields a series of eigen frequencies, f_{n,n_x}, for ice floe A (a two dimensional rectangular waveguide):

$$f_{n,n_x} = \frac{C_S}{2} \sqrt{(\frac{2n + 1}{H})^2 + (\frac{n_x}{L})^2}. \tag{4.9}$$

I am interested in ice floes with a large horizontal scale such that $L \gg H$. Under this assumption, the eigen-frequencies can be simplified as

$$f_n = \frac{(2n+1)C_S}{2H}, \quad n = 0, 1, 2, \ldots \quad (4.10)$$

Equation (4.10) represents the odd mode frequencies of SH waves in a one dimensional waveguide. The even modes cannot be excited by a unidirectional stress as described by (4.6).

The observed frequency ($778Hz$) of the pure tone signal (shown in Figure 4.2) indicates that rubbing or dry friction between ice floes has excited a wave similar to the fundamental mode (set $n = 0$ in Eq. (4.10)). If the above theory has indeed described the rubbing process precisely, one can expect that equation (4.10) can be used to infer the shear wave speed C_S of an ice floe provided its thickness is known. With $f_n = 778Hz$, $n = 0$ and $H = 1m$, (4.10) yields

$$C_S = 1556m \cdot s^{-1}.$$

4.5 Concluding Remarks on Chapter 4

I have derived a theoretical model to investigate the generation mechanism of the observed pure tone ice rubbing sound. Based on the observation (Figure 4.2), I believe that the dry friction between adjacent ice floes excites an SH wave in the ice. This SH wave radiates as a pure tone in the water with a frequency equal or close to the fundamental frequency predicted by the theory.

To avoid the cumbersome nonlinear boundary value problem indicated by equation (4.4), I have ignored the nonlinear effect by linearizing the boundary condition at the edge of ice floe A (see Eq. (4.5)). As a result, the pure tone frequency due to rubbing has been overestimated since the nonlinear damping coefficient, whether it is positive or negative, will result in a frequency lower than the normal mode frequency given by equation (4.10). Therefore, the inferred shear wave speed ($1556 m \cdot s^{-1}$) from (4.10) provides a lower bound for the *in situ* ice, which seems resonable when compared with $1590 m \cdot s^{-1}$, a value inversely solved through the SAFARI model for new ice by Miller [56].

On the other hand, in a marginal ice zone, the primary stress on the ice floe is due to ocean currents and air flow. Therefore, a perfect waveguide does not exist for SH waves — the stress is always transferred into the ice floe through its boundaries, and the force making the two adjacent ice floes rub against each other is supplied from ocean currents beneath the ice and air flow above. In this case, the frictional force along the ice edge will result in a damping coefficient which is definitely positive, and the problem will no longer be nonlinear.

The observations reported here are insufficient to gain a complete picture of the generation mechanism of ice rubbing sound in the arctic ocean. Further experimental study is needed to search for answers to the following questions:

1. Does the pure tone sound result from a nonlinear rubbing process?

2. If a nonlinear effect is indeed involved in generating the sound, then how dominant is this effect in the sound generation?

Chapter 5

Conclusions of the Thesis

5.1 Summary of the Study

The observations made in the two ambient sound experiments provide me with a unique opportunity to examine the seismic and acoustical behaviour of Arctic sea ice in various environmental conditions. The analysis of the data motivates the development of 3 theoretical models respectively for ice fracturing due to internal stress (sources not clear), superficial ice cracking due to thermal stress and ice rubbing due to relative motion between ice floes. The surveys of *in situ* ice by photography and SAR imaging and the acoustical localization of individual cracks (though not very precise), make it possible for the first time to correlate the spatial distribution of cracks with ice conditions. The main research orientation of this thesis focuses on the study of failure mechanisms of the Arctic ice cover through the sound radiated from individual cracks and leads to the potential use of ambient sound to monitor remotely the mechanical properties of sea ice. Both the artificial sound made in the second experiment and some naturally occurring sound, vividly illustrate the filtering effect of an ice cover on a broadband source, and the importance of the water channel in ambient ice sound propagation compared to the contribution of the ice waveguide.

The main results from this study are summarized in the following:

142

- The fracturing of sea ice radiates sound into the ocean. The signals usually consist of a dominant component of low frequency and possibly a small component of a high frequency. The base band signals correspond to the bulk vibrations of the ice cover. Therefore, the corresponding frequency is a function of mechanical bulk properties of the ice. For most observed events, this frequency is below $700 \sim 1000 Hz$, depending on the ice thickness, the Young's modulus, etc. As far as the high frequency signals are concerned, it is believed that they result directly from the actual slip-stick seismic movements over the fault planes at the crack.

- Rubble ice with tilted snow free surfaces is most sensitive to thermal cooling effects. It responds to thermal stress by surface cracking when the temperature drops to around $-20C$. In contrast, ice covered with a snow layer of a few centimetres does not respond to cooling.

- Thermal cracking tends to radiate sound in directions parallel to ice surfaces. If the ice surface is flat, maximum radiation is in the horizontal direction.

- Ice failures due to loading or any failure processes that can be represented by a monopole in the ice cover will result in a dipole radiation pattern.

- For superficial cracking, it is found that the frequency of the cracking sound depends on the radiation angle. There is more high frequency sound radiated downwards than horizontally.

- Ice rubbing seems to be an efficient mechanism for generating SH waves in the ice. Based on the observed rubbing event, it is felt that the nonlinearity effect is not profound.

In concluding this thesis, I would like to point out that the acoustical radiation from an ice cracking event in sea ice is the consequence of geophysical response of ice to various stresses. This response consists of ice fracturing of different scales

and vibrations of the ice plate in different modes. The analysis of individual events shows quite often that certain aspects of the ice response are dominant. In order to use the sound of cracking to infer the behaviour and properties of sea ice, realistic theoretical models must be developed to provide a firm basis for interpretation of observations.

5.2   Suggestions for Future Research

Naturally occurring sound results from failure processes in the ice, and one gains a lot by analyzing this kind of sound. However, it is not an easy task to predict exactly when and where cracks would occur. It is even harder to reconstruct precisely the source mechanisms based on the observed sound. While the monitoring of under-ice ambient sound is an indispensable experimental approach in future ice studies, more effort should be made to use artificial sources to probe the dynamics of the acoustical behaviour of sea ice. Although only one mode of failure can be simulated by artificial sources at a time (say loading failure), the corresponding sound should reveal the ice response to that particular mode of failure. This approach will enable us to represent the geophysical response of sea ice to various environmental stresses in terms of response functions to various modes of failure.

Another aspect of the field study of sea ice is to monitor simultaneously the under-ice ambient sound field and strain field of the corresponding ice floe(s) so that the radiated sound can be related to stress release within the ice. The comparison of these two energy budgets will provide us with some information on how efficient the stress releasing process in the ice is in generating under-ice sound (including both water mode and ice mode acoustical radiation). If the acoustically radiated energy is significant compared with the total released stress, then it would provide a motivation for studying the efficiency of water mode acoustical radiation in stress release from sea ice. To fulfill this purpose, a joint experiment is needed in which both acousticians and experts on ice mechanical properties participate. It seems that such an opportunity may occur, when a project to be funded by the Office of Naval Research to study the mechanical properties of the Arctic sea ice gets underway in a couple of years.

The following are a few suggestions for future experiments.

- Using artificial sources to check the angular frequency response of the ice at as many radiation angles as possible. This work can be done both in the

laboratory and in the field.

- If the frequency shift does occur, then the highest frequency that can be radiated, should be established. This cutoff frequency should tell us something about the viscous properties of the ice.

- A laboratory study should be initiated to study acoustical radiation patterns from an ice cover for normal impact forcing and horizontal tensile forcing. The comparison of the two patterns will further confirm that the preferential radiation directions of excited sound are closely related to the forcing directions.

- A laboratory study should also be conducted to study the generation mechanisms of the sound of rubbing ice. It will be interesting to determine, for an ideal ice plate subject to rubbing under different magnitudes of normal pressure, what is the range of radiated frequencies and how far these frequencies deviate from the first mode SH wave frequency. Answers to these two questions will lead to a better understanding of how important the nonlinear effect is on the sound generated by rubbing ice.

Appendix A

An Underwater Sound Field due to a Point Harmonic Source in an Ice Cover

In the following, I will show how a solution to the problem given by equations (2.1) to (2.4) is obtained.

Using Hankel transform, I can express $\Phi_{1,2}(R, Z)$ in terms of their spatial spectra $\widetilde{\Phi}_{1,2}(Z, \eta)$:

$$\Phi_{1,2}(R, Z) = \int_0^\infty \widetilde{\Phi}_{1,2}(Z, \eta) J_0(\eta R) \eta \, d\eta, \qquad (A.1)$$

where $\eta = k_1 \cos \alpha_1 = k_2 \cos \alpha_2$ is horizontal wavenumber; $J_0(\eta R)$ is the zero order Bessel function. The subscripts 1 and 2 again refer to ice and water respectively. It is easy to show that

$$4\pi \delta(R, Z - h) = 2 \int_0^\infty \delta(Z - h) J_0(\eta R) \eta \, d\eta. \qquad (A.2)$$

Upon substituting (A.1) and (A.2) into equations (2.1) to (2.4), the original wave problem is represented by two ordinary differential equations in terms of $\widetilde{\Phi}_{1,2}(Z, \eta)$:

$$\frac{d^2 \widetilde{\Phi}_1}{dZ^2} + \beta_1^2 \widetilde{\Phi}_1 = -2\delta(Z - h), \qquad Z < H; \qquad (A.3)$$

147

and

$$\frac{d^2\widetilde{\Phi}_2}{dZ^2} + \beta_2^2\widetilde{\Phi}_2 = 0, \qquad\qquad Z > H; \qquad\qquad (A.4)$$

where $\beta_1 = \sqrt{k_1^2 - \eta^2}$, $\beta_2 = \sqrt{k_2^2 - \eta^2}$ are the vertical wavenumbers in ice and water respectively.

The point source is represented by the delta function and this representation causes the source position $(0, h)$ to be a singular point for the sound field. In other words, the wave equation is invalid at the source. To overcome this difficulty, I integrate equation (A.3) with respect to Z around the source region, i. e. from h^- (just below the source) to h^+ (just above the source). Thus:

$$\frac{d\widetilde{\Phi}_1}{dZ}\Big|_{h^+} - \frac{d\widetilde{\Phi}_1}{dZ}\Big|_{h^-} = -2, \qquad\qquad (A.5)$$

and the sound pressure field is continuous at $Z = h^+, h^-$ for a monopole source. Therefore

$$\widetilde{\Phi}_1\Big|_{h^+} = \widetilde{\Phi}_1\Big|_{h^-}. \qquad\qquad (A.6)$$

Equations (A.5) and (A.6) are the famous Pekeris source conditions which state that at the source, sound pressure remains continuous but the pressure gradient is discontinuous. These conditions allow the subdivision of the ice cover into two layers: one is above the source ($Z > h$); the other below the source ($Z < h$). Therefore, the source effect is transferred to a boundary condition.

The other two boundary conditions at the ice surface and ice-water interface are given in terms of $\widetilde{\Phi}_{1,2}(Z, \eta)$ as

$$\widetilde{\Phi}_1 = 0, \qquad\qquad at \;\; Z = 0, \qquad\qquad (A.7)$$

and

$$\left.\begin{array}{rcl} \rho_1\widetilde{\Phi}_1 & = & \rho_2\widetilde{\Phi}_2 \\[2ex] \frac{d\widetilde{\Phi}_1}{dZ} & = & \frac{d\widetilde{\Phi}_2}{dZ} \end{array}\right\} \qquad at \;\; Z = H. \qquad\qquad (A.8)$$

Thus, equations (A.3) to (A.8) form a boundary value problem equivalent to the original wave problem.

Neglecting attenuation effects of the media on sound, the solutions to equations (A.3) and (A.4) are

$$\tilde{\Phi}_1(Z,\eta) = \begin{cases} Ae^{-i\beta_1(Z-h)} + A_1 e^{i\beta_1(Z-h)} & Z \le h \\ Be^{i\beta_1(Z-h)} + Ce^{-i\beta_1(Z-h)} & h \le Z \le H, \end{cases} \qquad (A.9)$$

and

$$\tilde{\Phi}_2(Z,\eta) = De^{i\beta_2(Z-H)} \qquad\qquad Z \ge H. \qquad (A.10)$$

Subtitution of the first expression in equation (A.9) into (A.7) leads to

$$A_1 = -Ae^{2i\beta_1 h}.$$

Thus, the sound field in the ice cover and water given by (A.9) and (A.10), can be expressed in terms of 4 coefficients, i. e. A, B, C and D. Substituting (A.9) into (A.5), (A.6) and (A.8), I obtain 4 algebraic equations with respect to the 4 coefficients

$$\begin{bmatrix} 1 - e^{2i\beta_1 h} & -1 & -1 & 0 \\ 2e^{2i\beta_1 h} & 2 & 0 & 0 \\ 0 & e^{i\beta_1(H-h)} & e^{-i\beta_1(H-h)} & -\rho_2/\rho_1 \\ 0 & e^{i\beta_1(H-h)} & -e^{-i\beta_1(H-h)} & -\beta_2/\beta_1 \end{bmatrix} \cdot \begin{bmatrix} A \\ B \\ C \\ D \end{bmatrix} = \begin{bmatrix} 0 \\ -2/i\beta_1 \\ 0 \\ 0 \end{bmatrix} \qquad (A.11)$$

Solving for coefficient D from (A.11) yields

$$D = \frac{2\sin\beta_1 h}{m\beta_1 \cos\beta_1 H - i\beta_2 \sin\beta_1 H},$$

which is identical to $S(\eta)$ in equation (2.7). Thus, equation (A.10) becomes

$$\tilde{\Phi}_2(Z,\eta) = \frac{2\sin\beta_1 h}{m\beta_1 \cos\beta_1 H - i\beta_2 \sin\beta_1 H} e^{i\beta_2(Z-H)} \qquad Z \ge H. \qquad (A.12)$$

Substituting (A.12) into (A.1), I obtain the underwater sound field due to a monopole source in the ice cover, i. e.

$$\Phi_2 = \int_0^\infty S(\eta)e^{i\beta_2(Z-H)} J_0(\eta R)\eta d\eta. \qquad (A.13)$$

Equation (A.13) is identical to equation (2.6).

In the following, I will use the stationary phase method to evaluate the integral given by equation(A.13). A similiar problem was solved by Brekhovskikh and Lysanov [57] who used the stationary phase method to evaluate a reflected sound field due to a point source (see pp. 76 to 79 of Ref. [57]). Now let me follow Brekhovskikh's approach to estimate the underice sound field caused by the radiation of sound from a monopole.

The zero order Bessel function $J_0(\eta R)$ can be expressed by a sum of zero order Hankel functions of 1st and 2nd kinds ($H_0^{(1)}(\eta R)$ and $H_0^{(2)}(\eta R)$):

$$J_0(\eta R) = \frac{1}{2}(H_0^{(1)}(\eta R) + H_0^{(2)}(\eta R)).$$

Using this relationship and an identity that

$$H_0^{(2)}(\eta R e^{-i\pi}) = -H_0^{(1)}(\eta R),$$

I can rewrite equation (A.13) as follows:

$$\Phi_2 = \int_{-\infty}^{\infty} S(\eta)e^{i\beta_2(Z-H)}H_0^{(1)}(\eta R)\eta d\eta. \tag{A.14}$$

For far-field cases, $\eta R \gg 1$, and

$$H_0^{(1)}(\eta R) \approx H_0^{(1)}(\eta R) \approx \sqrt{\frac{2}{\pi\eta R}}e^{i(\eta R - \pi/4)}(1 + \frac{1}{8i\eta R} + \cdots).$$

Substitution of this asymptotic expression into (A.14) leads to

$$\Phi_2 = \frac{e^{-i\pi/4}}{\sqrt{2\pi R}}\int_{-\infty}^{\infty} S(\eta)\sqrt{\eta}e^{-i\beta_1(H-h)}e^{i\phi(\eta)}d\eta, \tag{A.15}$$

where

$$\phi(\eta) = \eta R + \beta_1(H - h) + \beta_2(Z - H),$$

which is the phase built up by the propagation of sound (along the direct path) from the source (at $R = 0$, $Z = h$) to the observation point (R, Z) in the water. Since $R \gg \lambda$ (wavelength), $\phi(\eta)$ is a rapidly varying function of η. Therefore, the principal value of the integral given by equation (A.15) can be estimated by means of the stationary phase method. Note: here I am only considering the contribution of the monpole

source to the underwater sound through the direct path sound propagation, i. e. principal radiation. Sound reflected at the ice-air interface will of course contribute to the underwater sound field, but the high attenuation coefficient of sound in the ice makes these higher modes contribute relatively less to the underwater sound than the principal radiation. A full solution of the problem can be obtained by summing the contribution from all the possible modes as illustrated by Ewing *et al* (pp. 131 to 142 of Ref. [33]).

In terms of η, $\phi(\eta)$ can be expressed as

$$\phi(\eta) = \eta R + \sqrt{k_1^2 - \eta^2}(H - h) + \sqrt{k_2^2 - \eta^2}(Z - H). \qquad (A.16)$$

The stationary phase η_0 is the root of the following equation:

$$\frac{\partial \phi}{\partial \eta}\Big|_{\eta_0} = R + \frac{-\eta}{\sqrt{k_1^2 - \eta^2}}(H - h)\Big|_{\eta_0} + \frac{-\eta}{\sqrt{k_2^2 - \eta^2}}(Z - H)\Big|_{\eta_0}. \qquad (A.17)$$

From the geometry given in Figure 2.12, it follows that

$$R = \frac{H - h}{\tan \alpha_1} + \frac{Z - H}{\tan \alpha_2}.$$

Substitution of this relationship into equation (A.17) leads to

$$\eta_0 = k_1 \cos \alpha_1 = k_2 \cos \alpha_2. \qquad (A.18)$$

Therefore, the sound path giving the stationary phase is the one obeying Snell's law. Expanding $\phi(\eta)$ around $\eta = \eta_0$, one has

$$\phi(\eta) \approx \phi(\eta_0) + \frac{1}{2}\phi''(\eta_0)(\eta - \eta_0)^2. \qquad (A.19)$$

Substituting (A.19) into (A.15) yields

$$\Phi_2 \approx \sqrt{\frac{k_2 \cos \alpha_2}{2\pi R}} e^{-i\beta_1(H-h)} S(\eta_0) e^{i(\phi(\eta_0) - \pi/4)} \int_{-\infty}^{\infty} e^{i\frac{1}{2}\phi''(\eta_0)(\eta - \eta_0)^2} d\eta. \qquad (A.20)$$

Bearing in mind that $H < \lambda \ll R$, we obtain

$$\phi(\eta_0) \approx k_2 \cos \alpha_2 R + k_2 \sin \alpha_2(Z - H) \approx k_2 r, \qquad (A.21)$$

where r is the slant distance between the source and receiver (see Figure 2.12). The second derivative of $\phi(\eta)$ at η_0 is

$$\phi''(\eta_0) \approx -\frac{r}{k_2 \sin^2 \alpha_2}.$$ (A.22)

Using the value of the integral

$$\int_{-\infty}^{\infty} e^{-s^2}\, ds = \sqrt{\pi},$$

and substituting equations (A.21) and (A.22) into (A.20) one obtains

$$\Phi_2(r, t) \approx \frac{k_2 |\sin \alpha_2| S(\eta_0)}{r} e^{ik_2 r - i\omega t},$$ (A.23)

which is identical to equation (2.8) and is a compact form of the principal integral value for equation (A.13).

Appendix B

Acoustical Response of an Ice Cover to Loading Failure and Tensile Failure

In the following, I will provide detailed derivations of the 2 theoretical models used in chapter 3.

B.1 Ice Cover Subject to a Point Normal Force

In this section, I will show the acoustical response of an ice plate driven by a point normal force at its upper surface as illustrated in Figure 3.23. My goal is to derive the corresponding sound field beneath the ice plate.

First, let me briefly describe the main results based on the Steepest Descent Method which will be used in the subsequent derivation. According to Brekhovskikh (see pp. 234 to 237 of Ref. [42]), the path integral

$$I = \int_\Gamma e^{\eta f(\zeta)} F(\zeta) d\zeta \qquad (B.1)$$

can be evaluated by means of the steepest descent method provided the integrand function possesses some properties. In the above integral, $f(\zeta)$ and $F(\zeta)$ are analyt-

ical functions of the complex variable ζ; η is a parameter; Γ is the path of integration in the ζ plane. $f(\zeta)$ can be separated into its real and imaginary parts and rewritten as

$$f(\zeta) = f_1(\zeta) + if_2(\zeta).$$

If $e^{i\eta f_2(\zeta)}$ oscillates rapidly with ζ and $e^{\eta f_1(\zeta)}F(\zeta)$ in the integrand fall off rapidly with distance from a certain point, say ζ_0, then the integration in (B.1) is given by

$$I = e^{\eta f(\zeta_0)}\sqrt{\frac{\pi}{\eta}}[\Phi(0) + (\frac{1}{4\eta})\Phi''(0) + \cdots], \qquad (B.2)$$

where ζ_0 is the saddle point (the so called certain point) and is found from the equation

$$\frac{df}{d\zeta} = 0. \qquad (B.3)$$

At this point, f_1 takes its maximum and $e^{\eta f(\zeta)}$ falls off rapidly as ζ departs from ζ_0 for large η. $\Phi(\nu)$ is defined by

$$\Phi(\nu) = F(\zeta)\frac{d\zeta}{d\nu}, \qquad (B.4)$$

with ν being a real variable $(-\infty < \nu < \infty)$ which specifies the most convenient path for the evaluation of the integration. Therefore, the original integration path Γ can be changed into the so-called *saddle path* for the integrand function without affecting the final result. The saddle path is given by

$$f(\zeta) = f(\zeta_0) - \nu^2, \qquad (B.5)$$

which passes the saddle point $(\nu = 0)$. Along this path, $f_2(\zeta) = f_2(\zeta_0)$.

Now I consider the acoustical radiation from an ice plate which is subject to a time-harmonic normal point force f^n (see Figure 3.23). Lyamshev's reciprocity theory [43] states that if the scattering field P_s of a point source, placed at some point of the space surrounding a plate, is known , then the sound radiation P_r of the plate subject to a normal force f^n is uniquely determined at the same point. Mathematically,

$$P_r(r_2, z_2) = \frac{1}{i\omega\rho_0 Q}\int\int_S \frac{\partial P_s(r, z, r_2, z_2)}{\partial n}|_s f^n(r, z, \phi)ds, \qquad (B.6)$$

where n is the outward normal of the elementary area ds; f^n is a force applied normally to ds. The scattering field P_s due to a point source placed at (r_2, z_2) is given by equation (3.31).

In the plate vibration problem (indicated by Figure 3.23), the surface S is in the xy plane where $z = 0$ and the normal n is in the direction of the $-z$ axis. Thus, application of equation (B.6) to this problem leads to

$$P_r(r_2, z_2) = \frac{-1}{i\omega \rho_0 Q} \int \int_S \frac{\partial P_s(r, z, r_2, z_2)}{\partial z}|_{z=0} f^n(r, \phi) r dr d\phi, \qquad (B.7)$$

where the forcing term is given by equation (3.37). Substituting (3.37) into the above equation, one can easily obtain

$$P_r(r_2, z_2) = \frac{\rho_2 k_2 k_0 F^n}{8\pi\rho_0} \int_\Gamma H_0^{(1)}(k_2 r_2 \sin\theta) B_{21}(\theta) e^{ik_2 z_2 \cos\theta} \cos\theta_0 \sin\theta d\theta, \qquad (B.8)$$

where $H_0^{(1)}$ is the zero order Hankel function of the first kind, and Γ represents the saddle path obtained from equation (B.5). For large distance r and radiation angle θ not equal to 0, the Hankel function can be expressed in terms of its asymptotic form:

$$H_0^{(1)}(k_2 r_2 \sin\theta) \approx \sqrt{\frac{2}{\pi k_2 r_2 \sin\theta}} e^{i(k_2 r_2 \sin\theta - \pi/4)}(1 + \frac{1}{8ik_2 r_2 \sin\theta} + \cdots). \qquad (B.9)$$

From the geometry given in Figure 3.23, it is found that $z_2 - H = R\cos\theta_2$, $r_2 = R\sin\theta_2$ and $R \gg (H, a)$. These relationships lead to

$$z_2 \cos\theta + r_2 \sin\theta \approx R\cos\theta_2 \cos\theta + R\sin\theta_2 \sin\theta = R\cos(\theta - \theta_2). \qquad (B.10)$$

Substitution of (B.9) and (B.10) into equation (B.8) yields

$$P_r(r_2, z_2) \approx \frac{\rho_2 k_2 k_0 F^n \cos\theta_0 e^{-i\pi/4}}{8\pi\rho_0} \sqrt{\frac{2}{\pi k_2 r_2}} \int_\Gamma e^{ik_2 R\cos(\theta-\theta_2)} B_{21}(\theta)\sqrt{\sin\theta} d\theta. \quad (B.11)$$

Comparison of (B.11) with (B.1) leads to $\zeta = \theta$, $\eta = k_2 R$ and

$$F(\theta) = \frac{\rho_2 k_2 k_0 F^n \cos\theta_0 e^{-i\pi/4}}{8\pi\rho_0} \sqrt{\frac{2}{\pi k_2 r_2}} B_{21}(\theta)\sqrt{\sin\theta}, \qquad (B.12)$$

$$f(\theta) = i\cos(\theta - \theta_2). \qquad (B.13)$$

It follows from (B.13) that the saddle point $\zeta_0 = \theta_2$, and

$$\Phi(\nu) = F(\theta)\frac{2i}{\sqrt{\nu^2 - 2i}}. \tag{B.14}$$

Hence

$$\Phi(0) = \sqrt{2}e^{-i\frac{\pi}{4}}F(\theta_2). \tag{B.15}$$

Substituting the above relationships into equation (B.2), one obtains

$$P_r(r_2, z_2) = \frac{-i\rho_2 k_0 F^n \cos\theta_0 B_{21}(\theta_2)}{4\pi\rho_0 R}e^{ik_2 R}. \tag{B.16}$$

With $Z_0^{(0)} = \rho_0 C_0/\cos\theta_0$ and $Z_0^{(2)} = \rho_2 C_2/\cos\theta_2$, the above equation can be rewritten as

$$P_r^n(r_2, z_2) = P_r^n(R, \theta_2) = -i\frac{Z_0^{(2)}}{Z_0^{(0)}}\frac{k_2 F \cos\theta_2 B_{21}(\theta_2)}{4\pi R}e^{ik_2 R},$$

which is equation (3.39).

B.2 Ice Cover Subject to a Pair of Horizontal Point Forces

In this section, I will apply the above approach to a more complicated case i. e. the acoustical response of an ice plate driven by a pair of point forces tearing a small cylindrical cavity in the upper surface of an ice plate as illustrated in Figure 3.22. The motivation for searching for an analytical solution to this problem, seemingly very artificial, is to establish a Green's function for thermal cracking sound radiation, which may be useful for the study of sound radiation from a real thermal crack at the ice surface. Here, I emphasize that due to the difficulty in obtaining an analytical solution to a 3-D problem I am going to restrict my solution in a 2-D plane. In other words, I ignore the distortion effect of the cavity on the spherical wave P_q (given by (3.30) emitted from the imaginary point source at observation point $M(r_2, z_2)$, and keep the scattering field P_s in the same form as that shown by equation (3.31). While the vertical radiation pattern of the field can be obtained relatively easily from the final result, the azimuthal radiation pattern cannot be derived from this model due to the lack of azimuthal dependence of P_s in (3.31).

Turning to the original problem, I assume that a pair of point forces are applied normally to the inner surface of a shallow cylindrical cavity (see Figure 3.22). The forcing term in equation (B.6) is given by $f^r(\phi, z)$ in equation (3.33) and the normal to the inner surface is opposite to the radial direction, i. e. $-\vec{e_r}$. Taking all these into account, one has from (B.6) that

$$P_r(r_2, z_2) = \frac{1}{i\omega\rho_0 Q} \int \int_S \frac{\partial P_s(r, z, r_2, z_2)}{-\partial r}\Big|_{r=a} f^r(\phi, z) a d\phi dz,$$

which is given by equation (3.32). With (3.31) and (3.33) inserted into the above equation, and

$$\frac{dH_0^{(1)}(y)}{dy} = -H_1^{(1)}(y),$$

leads to equation (3.34). That is,

$$P_r(r_2, z_2) = \frac{-F^r \rho_2 k_2}{4i\rho_0} \int_\Gamma H_1^{(1)}(k_2(r_2 - a)\sin\theta)B_{21}(\theta)e^{ik_2 z_2 \cos\theta}k_2 \sin^2\theta d\theta.$$

For large distance r and radiation angle θ not equal to 0, the first order Hankel function of the first kind $H_1^{(1)}(k_2 r_2)$ can be expressed in its asymptotic form

$$H_1^{(1)}(k_2(r_2 - a)\sin\theta) \approx \sqrt{\frac{2}{\pi k_2(r_2 - a)\sin\theta}}e^{i(k_2(r_2-a)\sin\theta-\frac{3\pi}{4})}$$
$$(1 - \frac{3}{8ik_2(r_2 - a)\sin\theta} + \cdots), \qquad (B.17)$$

and equation(3.34) becomes

$$P_r(r_2, z_2) \approx \frac{-F^r \rho_2 k_2}{4i\rho_0} \int_\Gamma \sqrt{\frac{2}{\pi k_2(r_2 - a)\sin\theta}}e^{(ik_2(r_2-a)\sin\theta+ik_2 z_2 \cos\theta)-i\frac{3\pi}{4}}$$
$$B_{21}(\theta)k_2 \sin^2\theta d\theta. \qquad (B.18)$$

With the geometrical relationships indicated by Figure 3.22, the above equation can be rewritten as

$$P_r(r_2, z_2) \approx \frac{-F^r \rho_2 k_2}{4i\rho_0} \int_\Gamma \sqrt{\frac{2}{\pi k_2(r_2 - a)}}e^{ik_2 R \cos(\theta-\theta_2)-i\frac{3\pi}{4}}B_{21}(\theta)k_2 \sin^{3/2}\theta d\theta. \quad (B.19)$$

Comparison of the above with equation (B.1) leads to results similar to that for the vertical forcing case discussed in the previous section, except that $F(\theta)$ in (B.2) is given by

$$F(\theta) = \frac{-F^r \rho_2 k_2}{4i\rho_0}\sqrt{\frac{2}{\pi k_2(r_2 - a)}}k_2 \sin^{3/2}\theta B_{21}(\theta)e^{-i\frac{3\pi}{4}}. \qquad (B.20)$$

The saddle point ζ_0 in (B.2) remains the same as that obtained in the previous section, i. e. $\zeta_0 = \theta_2$. Substituting (B.20) into (B.2), one obtains equation (3.35). That is

$$P_r(r_2, z_2) = P_r(R, \theta_2) \approx \frac{iF^r \rho_2 k_2 \sin\theta_2 B_{21}(\theta_2)}{\rho_0 R}e^{ik_2 R}.$$

As mentioned in chapter 3, a real crack due to thermal tension is formed on the ice surface down to certain depth in the ice. Acoustically, the source produced by thermal cracking is physically located at the upper surface of the ice but in the ice interior. In order to use the theoretical model to simulate acoustical radiation from

such a source, it is necessary not only to close the cavity shown in Figure 3.22 (i. e. $a \to 0$), but also to let $\rho_0, C_0, \theta_0 \to \rho_1, C_1, \theta_1$ as well. This leads equation (3.35) to

$$P_r(R, \theta_2) \approx \frac{iF^r \rho_2 k_2 \sin \theta_2 B_{21}(\theta_2)}{\rho_1 R} e^{ik_2 R}. \qquad (B.21)$$

The corresponding transmission coefficient B_{21} is obtained through equation (3.24) with $Z_0^{(0)}$ replaced by $Z_0^{(1)}$. Thus,

$$B_{21}(\theta_2) = \frac{2Z_0^{(1)}(Z_s - Z_a)}{Z_s Z_a + 4Z_0^{(2)} Z_0^{(1)} + (Z_0^{(2)} + Z_0^{(1)})(Z_s + Z_a)}, \qquad (B.22)$$

where $Z_0^{(1)} = \rho_1 C_1 / \cos \theta_1$ and C_1 is the longitudinal wave speed in the ice plate; $\cos \theta_1$ is related to $\cos \theta_2$ by Snell's law:

$$\frac{\sin \theta_1}{C_1} = \frac{\sin \theta_2}{C_2}.$$

Taking $C_1 \approx 2C_2$ which is true for many applications, Snell's law yields:

$$\sin \theta_2 = \frac{1}{2} \sin \theta_1. \qquad (B.23)$$

Using the thin plate approximation, $|Z_s| \gg |Z_a|$, and considering the case in which $|Z_s| \gg |Z_0^{(2)}|$, I can simplify $B_{21}(\theta_2)$ to

$$B_{21}(\theta_2) = \frac{2Z_0^{(1)}}{Z_a + Z_0^{(2)} + Z_0^{(1)}}. \qquad (B.24)$$

Substituting the above into equation (B.21), one obtains

$$P_r(R, \theta_2) \approx \frac{iF^r k_2 \sin \theta_2}{R} \frac{2\rho_2 C_1}{Z_a \cos \theta_1 + \rho_1 C_1 + \rho_2 C_2(\cos \theta_1 / \cos \theta_2)} e^{ik_2 R}. \qquad (B.25)$$

By equation (B.23), it follows that

$$\rho_2 C_2 \frac{\cos \theta_1}{\cos \theta_2} = \rho_2 C_2 \frac{\cos \theta_1}{\sqrt{1 - \frac{1}{4}\sin^2 \theta_1}} < \rho_1 C_1.$$

Therefore, equation (B.25) can be further simplified, and with $\rho_1 \sim \rho_2$, it follows

$$P_r(R, \theta_2) \approx [\frac{ik_2 F^r e^{ik_2 R}}{R}][\frac{4\rho_2 C_2 \sin \theta_2}{Z_a(\omega)\sqrt{1 - 4\sin^2 \theta_2} + 2\rho_2 C_2}],$$

which is equation (3.41), a final form of the Green's function for horizontal forcing.

Bibliography

[1] N. Untersteiner, *The Geophysics of Sea Ice: Overview*, N. Untersteiner , ed. , NATO ASI Series, Plenum Press, New York, pp.1-8, 1986.

[2] D. M. Farmer and Yunbo Xie, *The Sound Generated by Propagating Cracks in Sea Ice*, J. Acoust. Soc. Am. , Vol 85 No. 4, pp.1489-1500, 1989.

[3] Yunbo Xie and D. M. Farmer, *Acoustic Radiation Beneath The Arctic Ice Cover*, in *Natural Physical Sources Of Underwater Sound* edited by B. R. Kerman, (In Press, Kluwer Academic Publishers, 1991).

[4] Yunbo Xie and D. M. Farmer *Acoustical Radiation from Thermally Stressed Sea Ice*, J. Acoust. Soc. Am. , Vol 89 No. 5, pp. 2215 - 2231, 1991.

[5] M. Mellor, *Mechanical Behaviour of Sea Ice*, N. Untersteiner , ed. , NATO ASI Series, Plenum Press, New York, pp.165-281, 1986.

[6] E. R. Pounder, *Physics of Ice*, London, Pergamon Press, 1965.

[7] T. Karlsson, *A Viscoelastic-plastic Material Model for Drifting Sea Ice*, in *Proceedings of International Conference on Sea Ice*, Edited by T. Karlsson, in Reykjavík, Iceland, May, 1971.

[8] G. F. N. Cox and W. F. Weeks, *Profile Properties of Undeformed First-Year Sea Ice*, CRREL Report 88-13, 1988.

[9] A. A. Griffith, *The Phenomona of Rupture and Flow in Solids*, Philosophical Transactions, Royal Society of London, A221, pp. 163-198, 1920.

[10] E. Orowan, *In Fatigue and Fracture of Metals*, edited by W. M. Murray, Wiley, New York, pp. 139-157, 1950.

[11] J. E. Dykins, *Tensile and Flexure Properties of Saline Ice*, edited by N. Riehl, B. Bullemer and H. Engelhardt, in *Proc. of Int. Symp. on Physics of Ice*, Plenum, New York, pp. 251-270,1969.

[12] A. Assur, in *Arctic Sea Ice*, Publication Number 598 of the National Academy of Sciences–National Research Council, Washington, pp. 106, 1958.

[13] N. N. Zubov, *Arctic Ice*,vol. 2, translated from Russian by the U. S. Navy Oceanographic Office and American Meteorological Society, 1943.

[14] J. K. Lewis, *Stress Relief in Sea Ice as Related to the Generation of High Frequency Noise in the Arctic Ocean*, A report to ONR, Feb. 1989.

[15] A. R. Milne, *Thermal Tension Cracking in Sea Ice; A Source of Underice Noise*, J. Geophys. Res. , 77(12), pp.281-327, 1972.

[16] F. N. Cox, *Thermal Expansion of Saline Ice*, J. Glaciol. , Vol. 29, No.103, pp. 425-432, 1983.

[17] D. M. Farmer and S. R. Waddell, *High Frequency Ambient Sound in the Arctic*, in *Proc. Natural Mechanisms of Surface Generated Noise in the Ocean*, NATO A. R. W. , Lerici, Italy, June 1987.

[18] S. R. Waddell and D. M. Farmer, *Ice Break-Up: Observations of the Acoustic Signature*, J. Geophys. Res. , 93(C3), pp.2333-2342, 1988.

[19] N. C. Makris and I. Dyer, *Environmental Correlates of Pack Ice Noise*, J. Acoust. Soc. Am. vol 79, pp.1434-1440, 1985.

[20] R. S. Pritchard, *Arctic Ocean Background Noise Caused by Ridging of Sea Ice*, J. Acoust. Soc. Am. vol 75, pp.419-427,1984.

[21] M. J. Buckingham and C. Chen *Acoustic Ambient Noise in the Arctic Ocean below the Marginal Ice Zone*, in *Sea Surface Sound* edited by B. R. Kerman (Kluwer Academic Publishers, 1988), pp. 583-598.

[22] F. Press and W. M. Ewing, *Propagation of Elastic Waves in a Floating Ice Sheet*, Trans. Am. Geo. Union 32(5), pp.673-678, 1951.

[23] P. J. Stein, *Acoustic Monopole in a Floating Ice Plate*, Ph. D. Thesis, Mass. Inst. of Tech. , 1986.

[24] P. J. Stein, *Interpretation of a Few Ice Event Transients*, J. Acoust. Soc. Am., vol 83, pp.617-622, 1988.

[25] I. Dyer, *The Song of Sea Ice and Other Arctic Ocean Melodies*, in Arctic Policy and Technology, edited by I. Dyer and C. Chryssostomidis, Hemisphere, New York, pp.11-37, 1984.

[26] A. R. Milne, *Wind Noise Under Winter Ice Fields*, J. Geophys. Res. , 79(12), pp.803-809, 1974.

[27] K. V. Mackenzie, *Reflection of Sound from Coastal Bottoms*, J. Acoust. Soc. Am. , vol 32, pp.221-231, 1960.

[28] K. Kasahara, *Earthquake Mechanics*, (Cambridge U. P., Cambridge U. K., 1981).

[29] I. Dyer, *Arctic Ambient Noise: Ice Source Mechanics*, *Physics Today*, (Published by Am. Inst. Phys. , Jan. 1988), pp. s5-s6.

[30] J. S. Kim, *Radiation from Directional Seismic Sources in the Laterally Stratified Media with Application to Arctic Ice Cracking Noise*, Ph. D. Thesis, Mass. Inst. of Tech. , 1989.

[31] J. P. Burg, *Maximum Entropy Spectral Analysis,* paper presented at the 37th Annual International Meeting, Soc. of Explor. Geophys.,Oklahoma City, Okla., Oct. 31, 1967.

[32] W. H. Press, B. P. Flannery, S. A. Teukolsky and W. T. Vetterling, *Numerical Recipes,* Cambridge University Press, 1986.

[33] W. M. Ewing, W. S. Jardetzky and F. Press, *Elastic Waves in Layered Media,* McGraw-Hill, New York, 1957.

[34] H. Schmidt and F. B. Jensen, A Full Wave Solution for Propagation in Multilayered Viscoelastic Media with Application to Gaussian Beam Reflection at Fluid-Solid Interfaces, J. Acoust. Soc. Am. , vol 77, pp.813-825, 1985.

[35] N. A. Haskell, *Total Energy and Energy Spectral Density of Elastic Wave Radiation from Propagating Faults,* Bull. Seis. Soc. Am. , 54, pp.1811-1841, 1964.

[36] J. C. Savage, *Relation of Corner Frequency to Fault Dimensions,* J. Geophys. Res. ,77(20), pp.3788-3795, 1972.

[37] L. Mansinha, *The Velocity of Shear Fracture,* Bull. Seis. Soc. Am. , 54, pp.369-376, 1964.

[38] G. S. Peck, *Arctic Oceanographic data Report 1978: Eastern Viscount Melville Sound, Vol. 2,* An internal technical report by Ocean and Aquatic Sciences Central Region, Fisheries and Oceans, Canada. (Unpublished Manuscript), May, 1980.

[39] M. G. G. Foreman, *Manual for Tidal Currents Analysis and Prediction,* Pacific Marine Science Report 78-6, The Institute of Ocean Sciences, Patricia Bay, Sidney, B. C. 1978.

[40] D. J. Tritton. *Physical Fluid Dynamics,* Van Nostrand Reinhold (UK) 1985.

[41] P. M. Morse and K. U. Ingard, *Theoretical Acoustics*, Princeton University Press, Princeton, NJ, 1986.

[42] L. M. Brekhovskikh, *Waves in Layered Media*, 2nd ed. translated by R. T. Beyer, Academic Press, New York, 1980.

[43] L. M. Lyamshev, *Theory of Sound Radiation by Thin Elastic Shells and Plates*, Soviet Physics – Acoustics (translated from Russian) Vol. 5, No. 4, pp. 431-438(1959).

[44] L. Ya. Gutin, *Sound Radiation from an Infinite Plate Excited by a Normal Point Force*, Soviet Physics – Acoustics(translated from Russian) Vol. 10, No. 4, pp. 369-371(1964).

[45] M. V. Greening, P. Zakarauskas and R. I. Verrall, *Vertical Directivity Measurements of Ice Cracking*, in *Natural Physical Sources Of Underwater Sound*, Edited by B. R. Kerman, (In Press, Kluwer Academic Publishers, 1991).

[46] M. Longuet-Higgins, *The production of Sound by Rain-drops: An Analytical Model for the Fluid Flow*, Presented in The Robert W. Stewart Symposium, Victoria, B.C. May 25-26, 1990.

[47] N. C. Makris, *Environmental Correlates of Arctic Ice Edge Noise*, Ph. D. Thesis, Mass. Inst. of Tech. , 1990.

[48] R. F. Dwyer, *Essential Limitations to Signal Detection and Estimation: An Application to the Arctic Under Ice Environmental Noise Problem* in *Proceedings of International Conference on Acoustics, Speech and Signal Processing*. San Diego, CA(USA) 19-21 March, 1984.

[49] R. F. Dwyer, *A Technique for Improving Detection and Estimation of Signals Contaminated by Under Ice Noise*, J. Acoust. Soc. Am. Vol. 74, pp. 124-130 (1983).

[50] M. Määttänen, *Stability of Self-Excited Ice-Induced Structural Vibrations*, in *Proceedings of the 4th International Conference On Port and Ocean Engineering under Arctic Conditions*, St John's, Newfoundland, Canada, 1977.

[51] M. Määttänen, *The Effect of Structural Properties on Ice-induced Self-Excited Vibrations*, *LAHR Ice Symposium*, Hamburg, 1984.

[52] H. H. Shen, W. D. Hibler III and M. Lepparanta, *The Role of Floe Collision in Sea Ice Rheology*, J. Geophys. Res. Vol. 92, pp. 7085-7096 (1987).

[53] N. W. Mclachlan, *Ordinary Non-linear Differential Equations in Engineering and Physical Sciences*, Oxford University Press, Oxford, 1956.

[54] P. Hagedorn, *Non-linear Oscillations*, Clarendon Press, Oxford, 1981.

[55] B. G. Levi, *Are Fractures Fractal or Quakes Chaotic?*, Published in *Physics Today* by The American Institute of Physics, Vol 43, No. 11, pp. 17 - 19, Nov. 1990.

[56] B. E. Miller, *Observation and Inversion of Seismo-Acoustic Waves in A Complex Arctic Ice Environment*, M. Sc. thesis, MIT, Cambridge, MA (1990).

[57] L. M. Brekhovskikh and Yu. Lysanov, *Fundamentals of Ocean Acoustics*, Springer-Verlag, 1982.